



A new Monte Carlo model of the detailed electron and ion distribution in the WGTS of KATRIN

Master's Thesis of

Christian Reiling

at the Department of Physics
Institute of Experimental Particle Physics (ETP)

Reviewer: Prof. Guido Drexlin
Second reviewer: Prof. Günter Quast
Advisor: Dr. Felix Spanier
Second advisor: Jonas Kellerer

26. November 2018 – 09. December 2019

Karlsruher Institut für Technologie
Fakultät für Physik
Wolfgang-Gaede-Str. 1
76128 Karlsruhe

I declare that I have developed and written the enclosed thesis completely by myself, and have not used sources or means without declaration in the text.

Karlsruhe, 09.12.2019

.....

(Christian Reiling)

Abstract

The **KATRIN - KA**rlsruhe **TRIT**ium Neutrino collaboration aims to measure the effective mass of the electron antineutrino with an unprecedented sensitivity of 0.2 eV. To limit the systematic uncertainty caused by plasma effects in the source of the KATRIN experiment a profound understanding of the plasma is needed. This is obtained from experimental studies and by plasma simulations.

For the plasma simulations a twofold simulation strategy is chosen. The **KARL - KA**trin **WGTS** elect**R**on and ion spectrum Monte **CarLo** code simulates particle distributions in fixed electric field settings across the source. Subsequently a Particle-in-Cell simulation computes arising electric fields from these particle distributions. By iterative combination of both simulation an equilibrium state will be reached, which reflects the plasma in the source of the KATRIN experiment.

In the scope of this master thesis the KARL code was developed. The KARL code uses semi-classical Monte Carlo techniques to kinetically simulate electrons and tritium ions within a pre-implemented molecular tritium distribution. The KARL code focuses on particle interactions. Therefore the latest theoretical and experimental models for elastic scattering, ionization, rotational excitation, vibrational excitation, electric excitation, recombination and cluster formation are implemented. Interactions among two particle species, that are kinetically simulated within KARL, are covered self consistently using runtime calculation of densities.

The KARL shows good performance and is highly parallelized. It successfully yields quantitative particle distributions and fluxes with high energy and spatial resolution. Analytical test cases are satisfying and first simulations show positive results and are in good agreement with previous simulations. In addition, the KARL code can simulate voltage-dependent electric currents at the Rear Wall of the KATRIN, which are an important tool for the experimental validation of the entire plasma simulation.

Zusammenfassung

Die **KATRIN** - **KARlsruhe TRITium** Neutrino Kollaboration möchte die effektive Masse des Elektron-Antineutrinos mit einer noch nie zuvor erreichten Genauigkeit von 0.2 eV bestimmen. In der Quelle des KATRIN-Experiments können Plasmaeffekte zu systematischen Unsicherheiten führen. Um diese einzugrenzen, muss ein umfassendes Verständnis des Plasma erlangt werden. Hierfür werden in der KATRIN-Kollaboration experimentelle Studien und Plasmasimulationen durchgeführt.

Für die Plasmasimulationen wurde ein zweigeteilter Ansatz gewählt. Der **KARL** - **Katrin** **WGTS electRon** und Ionenspektrum Monte Carlo Code berechnet Teilchenverteilung in konstanten vorimplementierten elektrischen Feldkonfiguration. Aus diesen Teilchenverteilungen werden anschließend mittels einer Particle-in-Cell Simulation die resultierenden elektrischen Felder bestimmt. Durch iterative Kombination beider Simulationen wird ein Gleichgewichtszustand erzielt, der das Plasma des KATRIN-Experiments widerspiegelt.

Im Zuge dieser Masterarbeit wurde der KARL-Code entwickelt. KARL benutzt semiklassische Monte Carlo Methoden, um Elektronen und Ionen kinetisch in einer vorgegebenen molekularen Tritiumverteilung zu simulieren. Der Fokus liegt dabei auf Teilcheninteraktionen. Hierfür wurden aktuelle theoretische und experimentelle Modelle für elastische Streuung, Ionisation, Anregung von Molekülen, Rekombination und Clusterbildung implementiert. Teilcheninteraktionen zwischen zwei Teilchenspezies, die beide kinetisch in der Simulation enthalten sind, werden mittels zur Laufzeit berechneten Dichten selbstkonsistent berücksichtigt.

Die Entwicklung des KARL-Codes wurde erfolgreich abgeschlossen. Der KARL-Code weist eine gute Performance auf und ist gut parallelisiert. Er liefert erfolgreich quantitative Teilchendichten und Teilchenflüsse mit hoher Orts- und Energieauflösung. Erste analytische Testfälle, sowie ein Vergleich zu bisherigen Simulationen, verliefen zufriedenstellend. Außerdem kann der KARL Code spannungsabhängige elektrische Ströme an der Rear Wall des KATRIN Experimentes simulieren, die eine experimentelle Validierung der Plasmasimulationen ermöglicht.

Contents

Abstract	i
Zusammenfassung	iii
1. Introduction	1
2. Neutrino physics	3
2.1. Neutrino physics in the past century	4
2.2. Neutrino oscillations	5
2.3. Neutrinos mass measurements	7
3. The KATRIN experiment	11
3.1. Overview and principle of work	11
3.2. Source and Transport Section (STS)	12
3.3. Spectrometer and Detector Section	14
3.4. Plasma effects in the WGTS	17
4. Monte Carlo and computation techniques	19
4.1. Random number generation	19
4.2. Sampling of Random variables	20
4.3. Particle Interactions	23
4.4. Change of particle track by interactions	25
4.5. Boris Push	26
4.6. Drift Approximation	27
4.7. Parallel computing strategies and the MPI standard	28
5. The KARL Code	29
5.1. Code intention	30
5.2. Technical details	31
5.3. Simulation strategy	31
5.4. Simulation of the Current Simulation Particle (CSP)	33
5.5. Runtime Density Field (RDF)	36
5.6. Macroscopic cross section (MCS) calculation	37
5.7. Logging Barrier Method	40
5.8. Parallelization strategy	41
5.9. Simulation parameters	41
6. Modeling of the WGTS and of particle interactions	45
6.1. Implementation of the WGTS	45

6.2. Interactions of electrons with tritium molecules	47
6.3. Recombination of electrons with tritium ions	50
6.4. Interactions of tritium ions	51
6.5. Modeling of tritium ions	52
7. Analytical tests of the simulation	53
7.1. Test of the injection methods	53
7.2. Test of elastic scattering	55
7.3. Test of ionization	56
7.4. Test of excitation	56
8. Simulations with KARL	59
8.1. First results using KARL	59
8.2. Simulations with recombination	65
8.3. Comparing KARL with previous simulations	66
8.4. Validation via voltage-dependent Rear Wall currents	69
9. Summary and outlook	71
Bibliography	73
A. Appendix	79

List of Figures

2.1.	Structure of the standard model of particle physics (SM) [GGS99] including the Higgs boson [Hig64]. Quarks in blue. Leptons in green. The Gauge bosons in red and the Higgs boson in orange.	3
2.2.	Feynman diagram of the β -decay. The neutron n decays under weak interaction resulting in a proton p , an electron e and an anti-electro neutrino $\bar{\nu}_e$	8
2.3.	Energy spectrum of β -decay with zoom on endpoint E_0 showing the shift in spectrum by neutrino mass (see Equation 2.19). The blue line represents the spectrum for $m(\bar{\nu}_e) = 1$ eV. The red line represents the spectrum for $m(\bar{\nu}_e) = 0$ eV. E_0 is the total freed energy in the β -decay.	8
2.4.	Feynman diagram of the neutrino less beta decay. The ν_e are viewed as Majorana particles and only participate as virtual particles.	9
2.5.	Energy spectrum of double beta decay. The red line represents the $2\nu\beta\beta$ -decay spectrum calculated from Equation 2.19. The blue line indicates the expected spectrum of a $0\nu\beta\beta$ -decay. The scale of this spectrum is arbitrary. E_0 is the total freed energy in the double β -decay.	9
3.1.	Overview of the beamline. RS: Rear Section, WGTS: Windowless Gaseous Tritium Source, DPS: Differential Pumping Section, CPS: Cryogenic Pumping Section, PS: Pre-Spectrometer, MS: Main Spectrometer, DET: Detector, STS: Source and Transport Section, SDS: Spectrometer and Detector Section.	11
3.2.	CAD drawing of the Windowless Gaseous Tritium Source. Gas density shown in green. Arrows represent gas flow direction. (Figure from [Ha17])	12
3.3.	CAD drawing of (a) the Differential Pumping Section: Turbo Molecular Pumps (TMPs) in yellow, magnets in blue. (b) Cryogenic Pumping Section: argon frost layer in blue, magnets in red. (Figure modified from [Fri+19])	13
3.4.	Scheme of the MAC-E filter. B denotes the magnetic field. Magnetic field lines represented by black lines in the spectrometer. Sample trajectory of an electron in blue color. The corresponding electron momentum displayed on the bottom of the figure. E denotes electron energy fractions . (Figure modified from [Bec+14])	14
3.5.	Pixel structure of the Detector (DET). Pixels aligned in twelve rings with twelve pixels each. Bullseye in the center has four pixels.	16
4.1.	Sketch of the numerical inversion technique. The black solid line represents the Probability Density Function (PDF) and the grey bars represent the bins of equal sizes.	21

4.2.	Sketch of rejection method. The black solid line represents the PDF. Values are sampled within $a < x < b$ and $0 < y < p_{max}$ represented by dotted surface. Values sampled in grey area are accepted and values in white area are rejected.	22
4.3.	Cumulative Distribution Function (CDF) of a discrete histogram with borders x_i	23
5.1.	Scheme of the twofold plasma simulation strategy. The KARL code calculates electron and ion distributions in a given electric field configuration and passes these distributions to the Particle-in-Cell (PIC) code. The PIC code calculates an electric field configuration from electron and ion distributions and passes these electric fields to the KARL code.	30
5.2.	Flowchart of the simulation algorithm. Algorithm starts with injection of one β -electron. Consecutively the β -electron and all arising particles are being simulated. New β -decays are performed until the number of target decays is reached. PQ: Particle Queue.	32
5.3.	Flowchart of the physical simulation algorithm for a CSP. Particles simulation alternates between propagation by the mean free path (MFP) and performing interactions until a termination condition is met.	33
5.4.	Sketch of shift from simulation coordinate system to laboratory frame. \vec{v}_1 is the velocity of bombarding particle in the simulation system. $\vec{v}_2(\vartheta, \varphi)$ is the velocity of the target particle in the simulation system. In the simulation integration over all possible ϑ and φ is performed. The integration is independent of φ . ϑ is displayed in blue. The resulting velocity of the bombarding particle is displayed in red and labeled as \vec{v}_{lab}	37
5.5.	Sketch of a particle with longitudinal speed v_z passing a Logging Barrier. The particle is displayed in blue. The Logging Barrier is displayed as thick red line. Dashed box with surface A and thickness dl represent volume the particle passes with constant speed v_z . Velocity components of the particle parallel to the Logging Barrier are not displayed in this sketch.	40
5.6.	Flowchart of the parallelization strategy of the KARL code. n_{left} is the number β -decays left until reaching the number of target decays. n_{step} is the number β -decays that are simulated on each core before synchronizing the RDF and n_{cores} is the number of cores used for the simulation.	41
6.1.	Sketch of the geometrical implementation of the Windowless Gaseous Tritium Source (WGTS) for the KARL simulation. The simulation area is marked in gray. The WGTS has a length of 13 m and a radius of 45 mm. The Rear Wall (RW) is positioned at $z = -3$, the Turbo Molecular Pumps (TMPs) are set at $z = 0$ and $z = 10$, the tritium inlet at $z = 5$. The scaling of z -axis and r -axis is chosen arbitrary here.	46
6.2.	Longitudinal course of the molecular tritium density profile over the length of the WGTS. The densities are calculated in respect to the maximum density n_0 at $z = 5$. The reduction factors are obtained from [Kuc+18].	46

-
- 6.3. Overview of implemented e^- - T_2 interactions. Displayed ionization and excitation TCS are summed over all sub channels. Energies defined in laboratory frame, where kinetic electrons interact with fixed tritium molecules. 47
- 6.4. Visualization of the composition of the Total Cross Section (TCS) of e^- - T_2 elastic scattering. The TCS is composed of three models. The dotted, yellow line represents the TCS for energies $E > 100$ eV. These TCSs are calculated using ELSEPA [SJP05]. The dashed, blue line represents the TCS for energies 0.02 eV $< E < 100$ eV. These TCS are adapted from experimental data from [Yoo+08] was used. The solid, red line represents the TCS for energies $E < 0.02$ eV. These are obtained by interpolation of the experimental data. 48
- 6.5. TCSs for electron-ion recombination of different tritium ions. TCS for e^- - T_2^+ and e^- - T_3^+ recombination from [JRS03]. TCS for e^- - T_5^+ recombination from [Pet+15]. Energies defined in laboratory frame, where kinetic electrons interact with fixed T_2 molecules. 50
- 7.1. Test of Maxwell Boltzmann Injection (INJECTION = 2) at three different energies: 1 meV (left), 1 eV (center), 1 keV (right), which are related to the temperature of the Maxwell Boltzmann distribution by $E = k_B T$. The red histograms show the observed electron energy spectrum at the RW. The solid, black lines shows the expected spectra. 54
- 7.2. Test of β -injection. The red histogram shows the observed energy spectrum at the RW. The solid, black line shows the expected β -spectrum (Equation 2.19). 54
- 7.3. Test of elastic scattering. Electrons are injected with constant energy of 5 meV (left) and 0.1 meV (right). The blue, dashed line represents the injection energy. After sufficient number of elastic scattering the electrons are expected to enter the 1 meV ($\hat{=}$ 11.6 K) Maxwell Boltzmann distribution of the underlying molecular tritium distribution. This expected spectrum is represented by the black, solid lines. These are normalized to the number of observed electrons. The red histograms represent the observed electron spectrum in the center of the WGTS. 55
- 7.4. Test of ionization. Electrons have been injected with constant energy of 30 eV. The expected energy spectrum is a superposition of secondary electron spectrum and altered primary spectrum. This expected spectrum is represented by the black, solid lines. The observed electron spectrum at the RW is displayed by the histograms in red. 56
- 7.5. Test of excitation. Electrons have been injected with constant energy of 1 eV. The expected energy spectrum consist of scattered electrons with energies of 0.484 eV and unscattered electron at 1 eV. The observed electron spectrum at the RW is displayed by the red histograms. 57

8.1.	Differential electron density spectrum averaged over the length of the WGTS. The solid, red line represent the results from SIM1. The dotted, yellow line follows Equation 8.1 and was fitted to the results from SIM1. The dashed, blue line follows Equation 8.2 and was also fitted to the results from SIM1.	60
8.2.	Comparison of the differential electron density spectrum obtained from Logging Barrier Method (LBM) with the spectrum of RDF at the end of the simulation. The solid, red line represents the results from the LBM. The dashed, blue line represents the final states of the RDF at the end of the simulation. Both spectra are average over the length of the WGTS. The corresponding standard deviation is indicated by the shaded area.	61
8.3.	Differential electron densities from SIM1. The differential density is indicated by the color. Small densities are indicated by blue coloring. Towards higher densities the hue shifts to yellow. The x -axis represent longitudinal position in the WGTS. y -axis represents the electron energy on a logarithmic scale.	62
8.4.	Analysis of the high energetic β -electrons from SIM1. The solid, red line shows the number of e^- with energies $E > 10^2$ eV observed in the simulation. The dashed, blue line shows the expectation for unobstructed β -electrons of $N_\beta = 10^4$. Cutting the β -spectrum at 10^2 eV equals 99.1 % of the β -spectrum. The divergence of the simulation data to the expectation for unobstructed β -electrons is $O(1000) \hat{=} O(0.1)$	63
8.5.	Comparison of densities of electron from different energy regimes from SIM1. The solid, red line represents the thermal electrons with energies $E < 10^{-2}$ eV. The dashed, blue line represents the non-thermal secondary electrons with energies 10^{-2} eV $< E < 10^2$ eV. The dotted, yellow line represents the β -electrons with energies $E > 10^2$ eV. The dash-dotted, green line represents the density of molecular tritium.	63
8.6.	Particle densities from SIM1. The solid, red line represents the electron density. The dashed, blue line represents the density of molecular tritium. The dotted, yellow line represents the density of tritium ions.	64
8.7.	Particle fluxes from SIM1. The solid, red line represents the particle flux of electrons. The dashed, blue line represents the ion flux. Positive fluxes indicates particles moving towards the spectrometers.	64
8.8.	Comparison of SIM1, SIM2 and SIM3 from KARL in the thermal region. The upper half of the plot shows the differential densities. The displayed densities are averaged over the whole length of the WGTS. The bottom half of the plot shows the ratio of the densities from SIM2 and SIM3 in respect to SIM1. SIM1: Conservative estimator without recombination, displayed as solid, red line. SIM2: Implementation of asymmetric recombination, displayed as dashed, blue line. SIM3: Implementation of recombination by solely accounting electron energy in the MCS calculation, displayed as dotted, yellow line.	65

8.9.	Comparison of differential electron densities from SIM1 with results of COMP1 [Nas+05]. The results from KARL are averaged over the WGTS and displayed as solid, red line. The shaded area represents standard deviation of the longitudinal averaging. The dashed blue line shows results from COMP1. The spectrum of COMP1 was normalized using the β -spectrum at energies $E > 10^2$ eV.	67
8.10.	Comparison of SIM2 and SIM3 with results from COMP1 [Nas+05] in the thermal region. The upper half of the plot shows the differential densities. The displayed densities from SIM2 and SIM3 are averaged over the whole length of the WGTS. The shaded area represent the stand deviation from this averaging. The bottom half of the plot shows the ratio of the densities from SIM2 and SIM3 in respect to COMP1. SIM2: Implementation of asymmetric recombination, displayed as dashed, blue line. SIM3: Implementation of recombination by solely accounting electron energy in the MCS calculation, displayed as dotted, yellow line. COMP1: Results from [Nas+05], displayed as dash-dotted, green line.	68
8.11.	Comparison of the longitudinal electron density distribution from, (a) SIM2: results from KARL, (b) COMP2: results from the plasma simulation of [Kuc16].	68
8.12.	Comparison of simulated voltage-dependent Rear Wall currents with experimental observations. The solid, red line represents the total Rear Wall current from simulation. The total consists of electron contribution (represented by dashed, blue line) and ion contribution (represented by dotted, yellow line). The observed currents from the experiment are represented by the dash-dotted green line. The measurement was made before KNM2 on the 20.09.2019 with a column density of 84 % at a temperature of 30 K.	69
A.1.	The FERMIAC, invented by E. Fermi. The FERMIAC is an analog computer using Monte Carlo method to study slow neutrino transport. It is one of the first applications of Monte Carlo methods for modern physics. (Picture from [Com17])	79
A.2.	Linear fit of e^- -T ₂ elastic scattering TCS data below 1 eV from [Yoo+08] . Resulting fit is used for sub 0.02 eV regime. Energies in laboratory frame, where of kinetic electrons interact with fixed T ₂ molecules.	81
A.3.	TCS for electron impact ionization of T ₂ . Cross sections from [JRS03]. Non-dissociative ionization channel with threshold energy of 15.42 eV displayed as solid red line. Dissociative ionization channel with threshold energy of 18.15 eV displayed as dashed blue line. Dissociative ionization channel with threshold energy of 30.6 eV displayed as dotted yellow line. Energies in laboratory frame, where of kinetic electrons interact with fixed T ₂ molecules.	81
A.4.	TCSs of e^- electronic excitations of T ₂ to dipole allowed singlet states. Models from [JRS03]. Energies in laboratory frame, where of kinetic electrons interact with fixed T ₂ molecules.	82

A.5.	TCSs of e^- electronic excitations of T_2 to symmetry forbidden singlet states. Models from [JRS03]. Energies in laboratory frame, where of kinetic electrons interact with fixed T_2 molecules.	82
A.6.	TCSs of e^- electronic excitations of T_2 to tripled states. Models from [JRS03]. Energies in laboratory frame, where of kinetic electrons interact with fixed T_2 molecules.	83
A.7.	Differential electron densities from SIM1 at different longitudinal positions z throughout the WGTS. Each line represents a different z position. . . .	85
A.8.	Comparison of differential electron densities of SIM1, SIM2, SIM3. Results averaged over the length of the WGTS. The shaded area represent the standard deviation. SIM1: Conservative estimator without recombination, displayed as solid, red line. SIM2: Implementation of asymmetric recombination, displayed as dashed, blue line. SIM3: Implementation of recombination by solely accounting electron energy in the MCS calculation, displayed as dotted, yellow line.	85

List of Tables

5.1. Overview of all possible termination channels.	36
5.2. Overview of simulation parameters with recommendation for KATRIN parameters in measurement mode.	43

List of acronyms

SM standard model of particle physics

SNO Sudbury Neutrino Observatory

MFP mean free path

CMB Cosmic Microwave Background

CνB Cosmic Neutrino Background

STS Source and Transport Section

SDS Spectrometer and Detector Section

RS Rear Section

WGTS Windowless Gaseous Tritium Source

RW Rear Wall

DPS Differential Pumping Section

CPS Cryogenic Pumping Section

PS Pre-Spectrometer

MS Main Spectrometer

DET Detector

TMP Turbo Molecular Pump

LARA Laser Raman spectroscopy

PDF Probability Density Function

CDF Cumulative Distribution Function

MPI Message Passing Interface

RNG Random Number Generator

PRNG Pseudo Random Number Generator

CS Cross Section

TCS Total Cross Section

DCS Differential Cross Section

MCS Macroscopic Cross Section

CSP Current Simulation Particle

RDF Runtime Density Field

LBM Logging Barrier Method

PIC Particle-in-Cell

PQ Particle Queue

IC interaction channel

1. Introduction

Neutrinos are neutral standard model fermions that only interact under weak force and gravitation. The mass of the neutrino is by orders of magnitude smaller than the mass of any other known standard model particle and has been recently¹ limited to 1.1 eV [Ake+19]. Due to their small mass and the short range of the weak force, interactions between neutrinos and matter are very scarce. Thus observing and measuring neutrinos is and has always been among the most difficult tasks in physics. Over the course of time many challenges have been met to form our today's understanding of neutrinos. A brief summary of the history of neutrinos and the knowledge accumulated until today is outlined in chapter 2.

A very important theoretical contribution was made by Enrico Fermi. In 1934 he published the first ever theory on neutrinos [Fer34]. Enrico Fermi was also the inventor of the FERMIAC, an analog computer using the Monte Carlo method for the study of neutron transport (Figure A.1). The FERMIAC was a predecessor to modern computers and the first application of the Monte Carlo method in modern physics. [Coc16]

Almost 90 years later Monte Carlo techniques and numerical simulations are still indispensable for modern physics, likewise for the KATRIN experiment in the examination of systematic uncertainties. The **KATRIN - KARlsruhe TRItium Neutrino** collaboration aims to measure the effective mass of the electron antineutrino with an unprecedented sensitivity of 0.2 eV. Currently the KATRIN collaboration provides, as previously stated, the best² upper limit for the neutrino mass of 1.1 eV. An overview of the KATRIN experiment is featured in chapter 3.

In particular, studies of plasma effects in the WGTS of the KATRIN experiment rely heavily on Monte Carlo simulations. β -decays of tritium molecules generate energetic electrons with energies of up to 18.6 keV. Subsequently, these kinetic electrons create additional charged particles through ionization. In total a significantly ionized electron-tritium plasma is created. Electric potentials arising from this plasma influence the neutrino mass deduction and are therefore particularly interesting. The plasma studies at KATRIN aim to elaborate a detailed map of the electric potential across the WGTS. In the neutrino mass analysis this map is used to properly take into account plasma effects and thus reduce the systematic uncertainty.

A complete analytical or experimental access to the plasma is virtually impossible. Thus numerical plasma simulations, along with experimental observations, are deployed to study the plasma. An all-in-one full kinetic plasma simulation for KATRIN is not feasible due to the complexity of the plasma. Hence a twofold simulation strategy is pursued.

¹as of September 2019

²from direct neutrino mass measurement

A Particle-in-Cell (PIC) simulation based on the ACRONYM code [KBS12] deduces the electric fields arising from a preinitialized electron density and ion flux configuration.

This configuration is simulated by the **KARL - KA**trIn WGTS electR^on and ion spectrum Monte CarLo code, which was developed in the scope of this thesis. It uses state of the art Monte Carlo and numerical computation techniques for the simulation of kinetic particles. An overview of these techniques is presented in chapter 4.

In particular, the KARL code uses a semi classical Monte Carlo approach, which covers propagation classically and particle interactions quantum mechanically. RDFs have been introduced to self consistently treat interactions among particles, that are simulated within KARL themselves. In order to obtain the desired electron distributions and ion fluxes the LBM was developed, which allows for high energy resolution and flexibility in the post processing. A detailed description of the simulation algorithm, including all developed features, is covered in chapter 5.

The above simulation algorithm can only yield good results if the boundary conditions are modeled correctly to match the KATRIN experiment. Therefore experimental and simulational studies from the KATRIN collaboration have been deployed to implement the WGTS. Furthermore, current experimental and theoretical models for particle interactions have been selected and implemented. An overview of all models used by KARL is summarized in chapter 6.

The KARL code was successfully implemented in C++. It shows good efficiency and is highly parallelized. For the first validation of the code, analytical test cases have been designed. Therefore features of the simulations are isolated and tested within a setting of expected output, which is analytically calculable. A series of test cases was performed and is presented in chapter 7.

Finally first simulations using KARL are performed. A detailed analysis of the resulting electron distribution and particle fluxes has been performed and are in good agreement with previous simulation results from [Nas+05]. In addition, simulations with KARL yield quantitatively and spatially resolved results, which can be used for various investigations. In particular, these can be converted to voltage-dependent currents at the RW of the KATRIN experiment, which can be used to experimentally validate the entire plasma simulation. First results and potential output from the KARL code will be presented in chapter 8.

In the final chapter 9 a summary of all implemented features of KARL is given. Further potential problems arising from assumptions have been identified, corresponding envisioned solutions are proposed and a general list of potential extensions worth following is presented.

2. Neutrino physics

In the standard model of particle physics (SM) [GG99] the neutrino is a neutral, massless, spin $1/2$ lepton. Neutrinos occur in three flavors: ν_e , ν_μ , ν_τ . Together with their respective

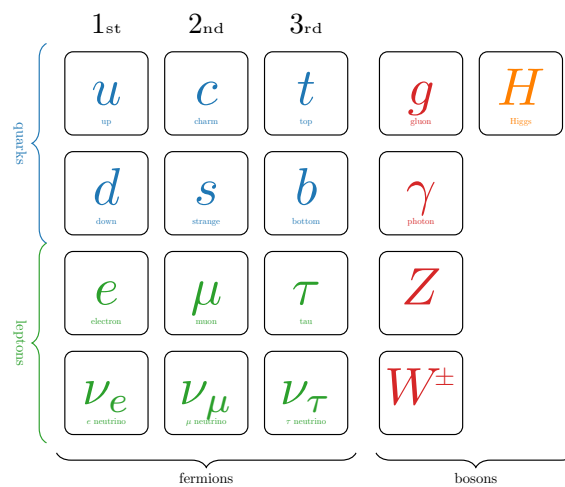


Figure 2.1.: Structure of the standard model of particle physics (SM) [GG99] including the Higgs boson [Hig64]. Quarks in blue. Leptons in green. The Gauge bosons in red and the Higgs boson in orange.

partners electron e , muon μ , tau τ they are subdivided into three leptonic generations (Figure 2.1).

In the SM neutrinos only interact under the weak interaction and the probability for interactions with neutrinos is extremely low. Particularly in the past this was a big challenge for neutrino experiments. An overview of the history of neutrino physics is summarized in section 2.1.

Modern neutrino experiments are still very challenging. In order to measure neutrino properties precisely, experimental setups have to be very accurate and sensitive. Sensitivity often scales with the size of an experiment. This leads to large and costly experimental setups.

For example, the Super-Kamiokande experiment [Fuk+98] uses a 50.000 t tank of ultra pure water 1000 m below the Earth's surface to study neutrino oscillations. In 2015, Takaaki Kajita, the head of Super-Kamiokande, along side Arthur B. McDonald of the Sudbury Neutrino Observatory (SNO), received the Nobel Prize in Physics for the discovery of neutrino oscillations.

Their observation of neutrino oscillation directly imply massive neutrinos. This is a clear contradiction to the standard model. In section 2.2 neutrino oscillations and their consequences for neutrinos masses are covered.

Neutrino oscillations cannot be used to determine the absolute neutrino mass. Hence other methods for neutrino mass measurement are needed. Recent strategies and experiments for neutrino mass measurement are summarized in section 2.3.

2.1. Neutrino physics in the past century

Postulation

The first indicator for the existence of neutrinos emerged from studies of the β -decay in the 1920s [BMH11; Cha14]. The β -decay was viewed as a quantum transition of a neutron towards a proton, while emitting an electron:



where A and Z stand for mass number and atomic number of the nuclei. The expected electron energy spectrum was a constant in energy. Contrary to the expectation the experiments showed a continuous electron energy spectrum. This observation questioned the theory.

Only in 1930 W. Pauli postulated the existence of a neutral, spin $1/2$, minimum interactive particle [Pau30], which is emitted alongside the electron in the β -decay:



In 1934 E. Fermi gave the particle the name neutrino and published his theory on the β -decay, which fulfills conservation of energy and angular momentum [Fer34].

Discovery

For another 26 years the neutrino was only a hypothetical particle whose existence could not be experimentally proven. But in 1953 C. Cowan and F. Reines finally confirmed Pauli's postulate. A nuclear reactor served as an anti electron neutrino source for their experiment. This led to higher fluxes compared to conventional radioactive probes. The detector consisted of a water target infused with cadmium chloride and a liquid scintillator. The setup was able to detect neutrinos by $\bar{\nu}$ -capture



The generated positron e^{+} annihilates immediately with an electron of the water producing two 511 keV photons. The neutron n is slowly captured by the cadmium. During this process photons with a total energy of 9 MeV are emitted. The combination of both signals have an unambiguous time signature and therefore clearly indicate an anti neutrino capture.

[Cow+56; Rei+60]

Discovery of neutrino flavours

In 1962 M. Schwartz, L. Lederman and J. Steinberger discovered the muon neutrino ν_μ at the Brookhaven National Laboratory. They examined pions π created at a nearby accelerator. During flight the pions decay into muons μ and neutrinos:

$$\pi^+ \rightarrow \mu^+ + \bar{\nu}_\mu \quad (2.4)$$

$$\pi^- \rightarrow \mu^- + \nu_\mu. \quad (2.5)$$

In order to prove the existence of the muon neutrino the particle beam was obstructed by a thick iron shielding and a detector was placed behind the shielding. The pions and muons are obstructed by the shielding, while the muon neutrinos can pass and reach the detector.

In the detector the muon neutrinos create muons by muon neutrino capture:

$$\nu_\mu + n \rightarrow p + \mu^- \quad (2.6)$$

$$\bar{\nu}_\mu + p \rightarrow n + \mu^+. \quad (2.7)$$

The detection of muons and the absence of electrons in the detector was a clear indicator for the existence of a second neutrino flavour.

[Dan+62]

The tau neutrino ν_τ was discovered in 2001 by the DONUT collaboration. They observed tau leptons τ from the D_s meson decay:

$$D_s \rightarrow \tau + \bar{\nu}_\tau. \quad (2.8)$$

Analog to the muon neutrino discovery the tau leptons were shielded from the detector. The tau neutrinos created tau leptons in the detector and thus the third neutrino flavor was discovered.

[Kod+01]

2.2. Neutrino oscillations

Discovery

The standard model of particle physics (SM) describes the structure and interplay of elementary particles very well. Nonetheless there are phenomena which can not be explained by the SM.

The solar neutrino problem was first indicated by the Homestake experiment [Kod+01]. The observed rate of solar electron neutrinos was only $1/3$ of the expected rate from theoretical pp-chain and CNO-cycle calculations. Later the Sudbury Neutrino Observatory (SNO) [Ahm+01] confirmed the lack of solar electron neutrinos and brought clear evidence for neutrino oscillations. Additionally the Super-Kamiokande experiment discovered the oscillation of atmospheric muon neutrinos towards tau neutrinos [Fuk+98].

In 2015 Takaaki Kajita (Super-Kamiokande) and Arthur B. McDonald (SNO) were awarded with the Nobel Prize in Physics for the discovery of neutrino oscillations.

Theory

The theory of neutrino mixing was first described by B. Pontecorvo, Z. Maki, M. Nakagawa and S. Sakata [Pon58; MNS62]. Their theory suggested different neutrino eigenstates for interaction and propagation. Neutrinos propagate through spacetime in their mass eigenstates $|v_1\rangle, |v_2\rangle, |v_3\rangle$ with corresponding masses m_1, m_2, m_3 . Whereas neutrinos interact under the weak interaction in their flavor eigenstates $|v_e\rangle, |v_\mu\rangle, |v_\tau\rangle$. Since flavor and mass states make up a full set of eigenstates, each flavor state is a superposition of mass states and vice versa:

$$\begin{pmatrix} |v_e\rangle \\ |v_\mu\rangle \\ |v_\tau\rangle \end{pmatrix} = \begin{pmatrix} U_{e1} & U_{e2} & U_{e3} \\ U_{\mu1} & U_{\mu2} & U_{\mu3} \\ U_{\tau1} & U_{\tau2} & U_{\tau3} \end{pmatrix} \cdot \begin{pmatrix} |v_1\rangle \\ |v_2\rangle \\ |v_3\rangle \end{pmatrix} = U \cdot \begin{pmatrix} |v_1\rangle \\ |v_2\rangle \\ |v_3\rangle \end{pmatrix}, \quad (2.9)$$

where U is the PMNS matrix.

At creation the neutrinos are in a well defined flavor eigenstate α depending on the creation process:

$$|v_\alpha(0)\rangle = \sum_{i=1}^3 U_{\alpha i} |v_i(0)\rangle. \quad (2.10)$$

During propagation neutrinos move as a superposition of eigenstates. For free propagation the mass states evolve as plane waves. After traveling by distance L and time t the states evolve to

$$|v_i(t)\rangle = |v_i(0)\rangle e^{-i(E_i t - pL)}, \quad (2.11)$$

where E_i and p are energy and momentum. Here natural units $c = \hbar = 1$ are used. For ultra relativistic neutrinos t and E are approximately:

$$t \approx L, \quad E_i = \sqrt{p^2 + m_i^2} \approx p + \frac{m_i^2}{2p}. \quad (2.12)$$

Therefore the state of a neutrino at distance L results in

$$|v_\alpha(L)\rangle = \sum_{i=1}^3 U_{\alpha i} |v_i(0)\rangle e^{-i \frac{m_i^2 L}{2p}} \quad (2.13)$$

and the probability of detecting a neutrino with flavor β at L is

$$P_{\alpha \rightarrow \beta} = |\langle v_\beta(0) | v_\alpha(L) \rangle|^2 = \left| \sum_{i=1}^3 U_{\alpha i}^* U_{\beta i} e^{-i \frac{m_i^2 L}{2p}} \right|^2, \quad (2.14)$$

where $\Delta m_{ij}^2 = m_i^2 - m_j^2$ is the squared mass difference. Hence neutrino oscillation arises from desynchronization of the mass eigenstates during propagation. This leads to nonzero Δm_{ij}^2 and therefore nonzero neutrino masses.

Measurement

Measurement of neutrino oscillation probabilities grant access to the PMNS matrix and the Δm_{ij}^2 . Suitable neutrino sources for neutrino oscillation measurements are solar neutrinos, atmospheric neutrinos and reactor neutrinos.

Combining the results from the most recent experiments [Tan+18] yields the following Δm^2 :

$$\Delta m_{21}^2 = 7.37 \times 10^{-5} \text{ eV}^2, \quad (2.15)$$

$$\Delta m_{31}^2 = 2.56 \times 10^{-3} \text{ eV}^2 \quad \text{for } m_1 < m_2 < m_3, \quad (2.16)$$

$$\Delta m_{23}^2 = 2.54 \times 10^{-3} \text{ eV}^2 \quad \text{for } m_3 < m_1 < m_2. \quad (2.17)$$

Nonetheless the absolute neutrino mass or the mass ordering can not be resolved by neutrino oscillation measurement.

[Tan+18]

2.3. Neutrinos mass measurements

Beta spectroscopy

The mass of the electron neutrino can be deduced from the kinematic of the β -decay. During the β -decay a neutron from the nucleus decays to a proton, while emitting an electron e^- and an anti electron neutrino $\bar{\nu}_e$ (Figure 2.2 and Equation 2.2). The freed energy E_0 is split between the electron and the neutrino:

$$E_0 = m({}_Z^A X) - m({}_{Z+1}^A X') = m(e^-) + E_e + m(\bar{\nu}_e) + E_\nu, \quad (2.18)$$

where m denotes the mass of the corresponding particle and E_e and E_ν the kinetic energy of the e^- and $\bar{\nu}_e$.

Following [Tan+18] the electron energy spectrum calculates to

$$\frac{dN}{dE_e} = C \cdot F(E, Z) \cdot p_e \cdot (E_e + m_e c^2) \cdot (E_0 - E_e) \sqrt{(E_0 - E_e)^2 - \sum_i |U_{ei}|^2 m_{\nu i}^2}, \quad (2.19)$$

where p_e denotes the electron momentum, $F(E, Z)$ the Fermi function, Z the number of protons in the daughter nucleus and C a constant.

As the influence of $m^2(\bar{\nu}_e) = \sum_i |U_{ei}|^2 m_{\nu i}^2$ on $\frac{dN}{dE_e}$ is dominant in the area around the endpoint E_0 (Figure 2.3) the mass of the electron neutrino $m^2(\bar{\nu}_e)$ can be deduced by precise spectroscopy of the electron energy spectrum around the endpoint.

The rate around the endpoint is rather small so a high source activity is essential. Additionally a good energy resolution is needed.

Past β -spectroscopy experiments have been performed in Mainz [Kra+05] and Troitsk [Ase+11] and provide an upper limit for the electron neutrino mass of 2 eV. The successor KATRIN (chapter 3) aims to reach a precision of 0.2 eV and is currently (September 2019) providing the best β -decay spectroscopy upper limit of 1.1 eV [Ake+19].

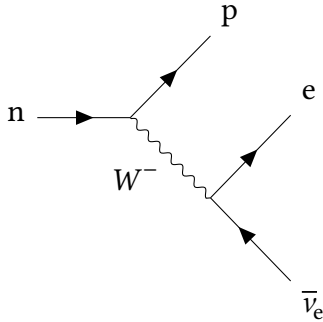


Figure 2.2.: Feynman diagram of the β -decay. The neutron n decays under weak interaction resulting in a proton p , an electron e and an anti-electron neutrino $\bar{\nu}_e$.

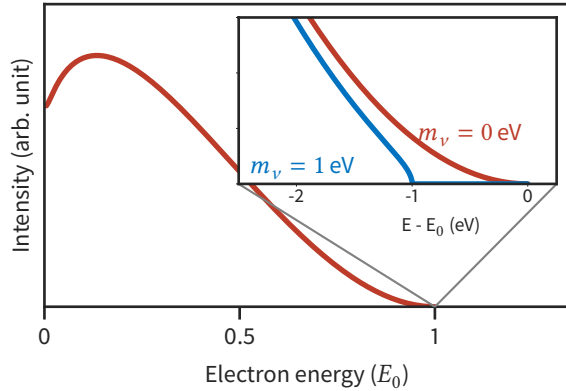


Figure 2.3.: Energy spectrum of β -decay with zoom on endpoint E_0 showing the shift in spectrum by neutrino mass (see Equation 2.19). The blue line represents the spectrum for $m(\bar{\nu}_e) = 1$ eV. The red line represents the spectrum for $m(\bar{\nu}_e) = 0$ eV. E_0 is the total freed energy in the β -decay.

Neutrinoless double beta decay

Following the single β -decay an even/even nuclei decays into an odd/odd nuclei. Therefore the β -decay can be energetically forbidden for certain even/even nuclei. In these nuclei double β -decay can occur. Two β -decays happen simultaneously and therefore turning an even/even nuclei into an even/even nuclei.

It is still a question of research whether the neutrino is a Majorana particle or a Dirac particle. If neutrinos were Majorana particles (their own antiparticle) the neutrinoless double β -decay $0\nu\beta\beta$ can occur. In the hypothetical $0\nu\beta\beta$ the two neutrinos are only generated as virtual particles. Thus directly annihilating with each other (Figure 2.4). Hence the two electron obtain the total excess energy of the decay and the sum of electron energies is a constant in energy (Figure 2.5).

Following [GP12] the neutrino mass can be deduced from the decay rate of the $0\nu\beta\beta$ -decay.

Currently there is no significant evidence for the $0\nu\beta\beta$ -decay from multiple experiments such as GERDA [GER+18], EXO-200 [Aug+12] and MAJORANA [Abg+14].

Cosmology

During the formation of cosmological structures neutrinos play a very important role. In the hot dark matter dominated universe neutrinos smear out structures smaller than the neutrino mean free path length. Hence only structures larger than the neutrino mean free path length can form.

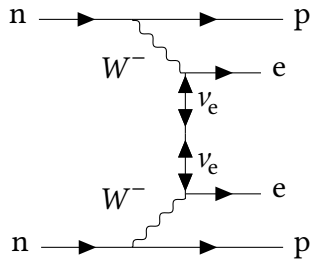


Figure 2.4.: Feynman diagram of the neutrino less beta decay. The ν_e are viewed as Majorana particles and only participate as virtual particles.

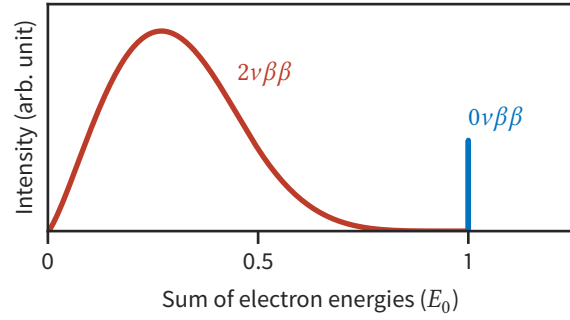


Figure 2.5.: Energy spectrum of double beta decay. The red line represents the $2\nu\beta\beta$ -decay spectrum calculated from Equation 2.19. The blue line indicates the expected spectrum of a $0\nu\beta\beta$ -decay. The scale of this spectrum is arbitrary. E_0 is the total freed energy in the double β -decay.

Common methods for experimental observation of the structure of the universe are galaxy and galaxy cluster surveys, strong and weak lensing, Lyman- α -forest and 21-cm-line measurements and Cosmic Microwave Background (CMB) examinations. Especially CMB examinations are very powerful tool, as they grant insight on the structure at a redshift of $z = 1000$.

[Tan+18]

In [Tan+18] multiple experimental data sets were combined resulting in an upper limit for the sum of neutrino masses of

$$\sum_{i=1}^3 m_i < 0.12 \text{ eV}..0.73 \text{ eV} . \quad (2.20)$$

Different limits arise from different datasets and models, which were taken into account.

3. The KATRIN experiment

The **KATRIN** - **K**Arlsruhe **T**RItium Neutrino experiment aims to measure the effective mass of the electron neutrino with an unprecedented sensitivity of 0.2 eV [KK05]. KATRIN is a next generation single β -decay experiment (section 2.3) with a target precision that is on order higher than its predecessors from Mainz [Kra+05] and Troitsk [Ase+11].

In 2016 the experimental setup of KATRIN was completed. Currently¹ the KATRIN collaboration has completed its first measurement campaign and provides the best neutrino mass limit from β -spectroscopy with 1.1 eV [Ake+19]. After a total of five years of measurement, KATRIN will have gathered enough statistics to reach the target sensitivity of 0.2 eV.

The measuring principle for reaching such a sensitivity will be introduced in section 3.1. In section 3.2 and section 3.3 the individual components of KATRIN will be presented in detail.

Besides good statistics, a comprehensive understanding of systematic effects is essential to reach the target sensitivity. In section 3.4 plasma effects influencing the β -spectroscopy are discussed. Further systematic effects are excluded from this work. The interested reader is referred to [Val07; Sei19].

3.1. Overview and principle of work

The KATRIN experiment uses single β -spectroscopy (section 2.3) of molecular tritium T_2 to determine the electron neutrino mass. T_2 is an ideal candidate because the endpoint energy of $E_0 \approx 18.6$ keV is rather low and it has a short halftime of $t_{1/2} \approx 12.3$ years, which can lead to a high source activity.

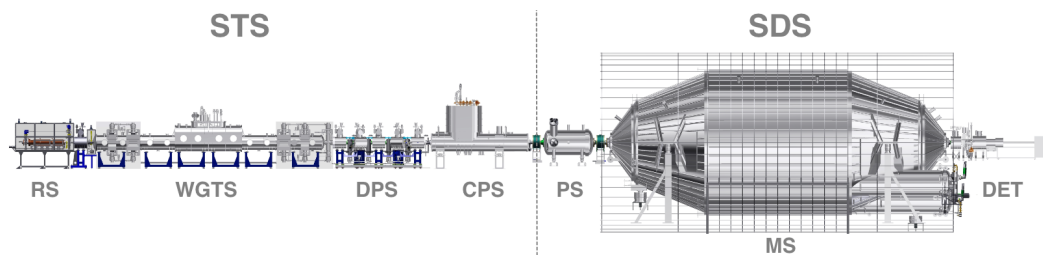


Figure 3.1.: Overview of the beamline. RS: Rear Section, WGTS: Windowless Gaseous Tritium Source, DPS: Differential Pumping Section, CPS: Cryogenic Pumping Section, PS: Pre-Spectrometer, MS: Main Spectrometer, DET: Detector, STS: Source and Transport Section, SDS: Spectrometer and Detector Section.

¹as of December 2019

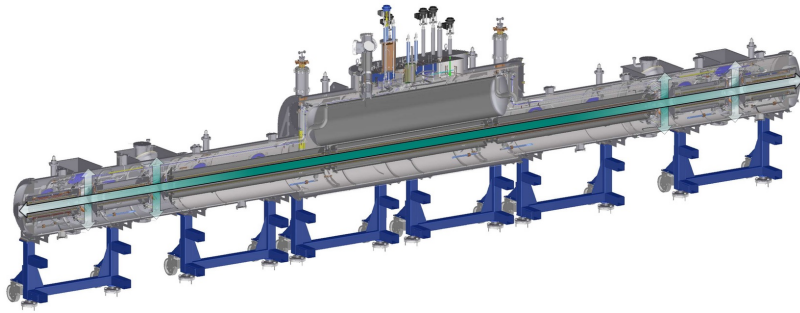


Figure 3.2.: CAD drawing of the Windowless Gaseous Tritium Source. Gas density shown in green. Arrows represent gas flow direction. (Figure from [Ha17])

The beam line of KATRIN consists of seven main components and is displayed in Figure 3.1.

In the WGTS β -electrons are created by β -decays of T_2 . The molecular tritium gas is injected in the center and removed at both ends using TMPs. Using strong magnetic fields the electrons are guided along the beam tube towards both ends.

To the rear side the WGTS is physically terminated by the Rear Section (RS). In forward direction the WGTS is connected to the Differential Pumping Section (DPS) and the Cryogenic Pumping Section (CPS). These two sections filter out all remaining neutral and ionized tritium.

Hence only electrons from the WGTS reach the Pre-Spectrometer (PS). Here the low-energy electrons are filtered out by usage of the MAC-E filter principle (section 3.3). The MAC-E filter of the PS is operated with a constant retarding potential of 10 kV. Thus all electrons with over 10 keV energy reach the Main Spectrometer (MS). The MS is a high precision MAC-E filter operated with a variable retarding potential.

Electrons surpassing the retarding potential of the MS will reach the Detector (DET). By varying the retarding potential of the MS around the endpoint of the β -decay an integral spectrum is obtained from which the electron neutrino mass can be deduced (Equation 2.19).

[KK05]

3.2. Source and Transport Section (STS)

Windowless Gaseous Tritium Source

The WGTS is designed to provide a stable and high β -electron flux with an activity of 10^{11} Bq. A scheme of the WGTS is displayed in Figure 3.2.

The 16 m long grounded tube has a diameter of 90 mm. The tritium inlets are in the center of the WGTS and provide a pressure of up to 10^{-3} mbar. 5 m from either side of the inlets four TMPs reduce the gas flow drastically and guide the gas to the loop system, where the tritium is purified and finally being fed back into the system. The interplay of inlet and pumping has to be precisely matched as the column density needs to be stable on

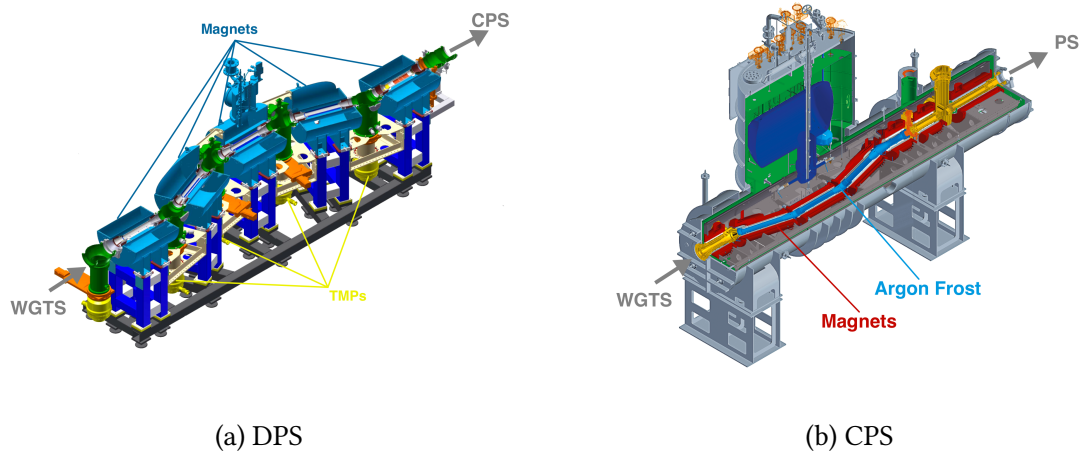


Figure 3.3.: CAD drawing of (a) the Differential Pumping Section: TMPs in yellow, magnets in blue. (b) Cryogenic Pumping Section: argon frost layer in blue, magnets in red. (Figure modified from [Fri+19])

the per mille level. The resulting T_2 column density is $5 \times 10^{21} \text{ m}^{-2}$ for standard KATRIN operation.

The WGTS is cooled down to 30 K to prevent thermal doppler blurring of the β -spectrum. The guiding magnetic fields are created by seven superconducting magnets resulting in a magnetic field of 2.5 T. [Ha17]

Rear Section

The Rear Section (RS) terminates the WGTS towards the rear side using the gold-plated crystalline RW. The RW is set on a constant potential to minimize plasma effects (section 3.4).

The RS is used for calibrations and measurements purposes. Using β -induced X-ray spectroscopy (BIXS) the source activity is monitored [Röl15]. The source density can be examined using an electron gun. This electron gun is also used for various measurements and calibrations such as energy loss measurements. [Sch16]

Differential Pumping Section

In the Differential Pumping Section (DPS) the flux of tritium molecules and ions is reduced by a factor of 10^{-5} . Tritium decaying in the spectrometer causes fatal background since the electric potential of the decaying tritium is not well defined thus leading to a distortion of the β -spectrum.

In the DPS a total of four TMPs are used to decrease the tritium flux. The DPS beam tube is bent (Figure 3.3a) to decrease the gas velocity and therefore to increase the pumping efficiency of neutral gas.

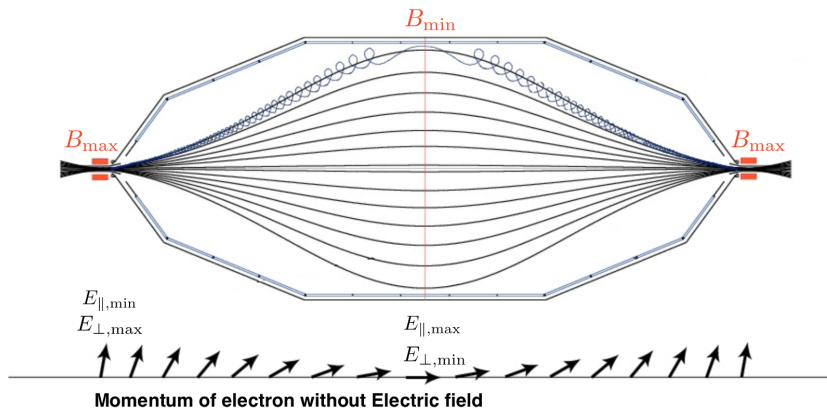


Figure 3.4.: Scheme of the MAC-E filter. B denotes the magnetic field. Magnetic field lines represented by black lines in the spectrometer. Sample trajectory of an electron in blue color. The corresponding electron momentum displayed on the bottom of the figure. E denotes electron energy fractions. (Figure modified from [Bec+14])

Charged particles are not influenced by the TMPs as they are guided by the magnetic field lines. In order to prevent tritium ions from entering the spectrometers, a ring shaped electrode is operated at positive voltage reflecting tritium ions. As they propagate back into the WGTS three dipole electrodes deflect the ions by $\vec{E} \times \vec{B}$ -drift. In the WGTS the ions are eventually reaccelerated towards the DPS by tritium flow. At some point the ions will be removed from the system by repetitive back and forth bouncing combined with $\vec{E} \times \vec{B}$ -deflection.

[Hac15; Win11]

Cryogenic Pumping Section

In the Cryogenic Pumping Section (CPS) the tritium flux is ultimately reduced by a factor of 10^{-7} thus leading to a negligible tritium pressure of 10^{-14} Pa. Therefore the CPS is cooled to 3 K and an argon frost layer is frozen onto the inner wall surface. Tritium molecules hitting the wall will be adsorbed by the argon frost. To increase the number of tritium molecules hitting the walls the CPS is tilted (Figure 3.3b). To uphold the adsorption efficiency, the argon frost is regenerated every 60 days.

[Gil+10]

3.3. Spectrometer and Detector Section

MAC-E filter principle

Both PS and MS use the Magnetic Adiabatic Collimation combined with an Electrostatic (MAC-E) filter principle. The schematic setup and principle of work is displayed in Figure 3.4. The filtering is performed in two steps. In the first steps the isotropic distributed

electron momenta are aligned parallel to the magnetic field. Afterwards the electrons are filtered using an opposing electrical potential.

Electrons guided by magnetic fields perform circular motions around the magnetic field lines. The total kinetic energy E_{tot} is composed of a parallel fraction E_{\parallel} and a transversal fraction E_{\perp} in respect to the magnetic field \vec{B}

$$E_{\text{tot}} = E_{\parallel} + E_{\perp} . \quad (3.1)$$

Adiabatic change of the magnetic field leads to conservation of magnetic momentum

$$\mu = \frac{E_{\perp}}{B} = \text{const} . \quad (3.2)$$

For a reduction from B_{max} at the entrance of the spectrometer to B_{min} in the center the perpendicular energy fraction of electron motion is reduced to

$$E_{\perp,\text{min}} = E_{\perp,\text{max}} \frac{B_{\text{min}}}{B_{\text{max}}} , \quad (3.3)$$

where $E_{\perp,\text{max}}$ corresponds to the transversal energy fraction at the entrance and $E_{\perp,\text{min}}$ in the center. For $\frac{B_{\text{min}}}{B_{\text{max}}} \ll 1$ the transversal energy is negligible and the total momentum is parallel to the magnetic field. At the point of minimal magnetic field a potential U_0 opposing the momentum is applied. Only electrons satisfying

$$E_{\text{tot}} > U_0 \cdot q \quad (3.4)$$

pass the barrier and are finally reaccelerated.

The energy resolution of the MAC-E filter is limited by Equation 3.3. The length of the spectrometer has to be sufficiently large in order to assure adiabatic change of the magnetic field. The minimum diameter is limited by conservation of magnetic flux ϕ :

$$\phi = \int d\vec{A} \cdot \vec{B} \stackrel{!}{=} \text{const} \implies d_{\text{max}} = d_{\text{min}} \sqrt{\frac{B_{\text{max}}}{B_{\text{min}}}} , \quad (3.5)$$

where d_{min} is the diameter at the entrance and d_{max} the diameter in the center.
[KK05]

Pre-Spectrometer

The Pre-Spectrometer (PS) is a small MAC-E filter with a length of 3.38 m and a diameter of 1.68 m. It is operated with a retarding potential of 10 kV. Hence the electron flux is drastically reduced and only high energetic electrons pass the PS.

Two TMPs provide a pressure of 10^{-11} mbar to keep the low pressure of the CPS. Thus reducing the scattering probability of electrons with gas. On both ends a superconducting magnet creates a magnetic field of 4.5 T.

[Frä10]

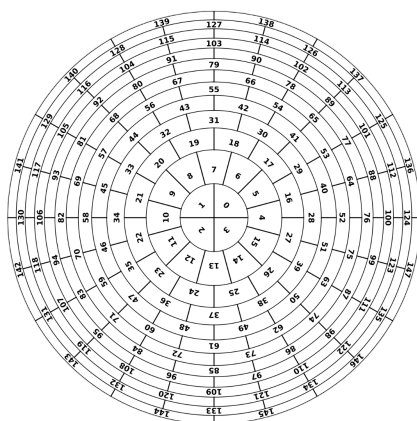


Figure 3.5.: Pixel structure of the DET. Pixels aligned in twelve rings with twelve pixels each. Bullseye in the center has four pixels.

Main Spectrometer

The Main Spectrometer (MS) is a high precision MAC-E filter operated with a variable retarding potential. In order to have a good energy resolution the MS has a diameter of 10 m and a length of 23 m. The magnetic field is created by two superconducting magnets and lead to a field of 6 T on both ends and 0.3 mT in the center. Thus leading to an energy resolution of 0.93 eV for 18.6 keV electrons (Equation 3.3).

[KK05]

The MS is surrounded by the Low Field Coil System (LFCS). A total of 14 coaxial air coils around the MS allow for adjusting the magnetic field precisely. Additionally the LFCS is surrounded by Earth Magnetic Compensation System (EMCS) allowing for compensation of the earth magnetic field.

[Glü+13]

The inner surface of the MS is covered by two layers of electrodes. These electrodes are operated 100 V and 200 V below the potential of the vessel hull. Thus preventing electrons from the spectrometer wall from entering the inner volume. Further the electrodes can be used to fine tune the electric field in the MS.

[Val10]

Detector

β -electrons surpassing the MS retarding potential hit the Detector (DET). The signal is recorded and digitalized. The DET consist of a 148 equal sized PIN diode array. The pixels are aligned in twelve rings with twelve pixels each and a bullseye of four pixels in the center (Figure 3.5). The individual pixels represent the position of origin in the WGTS. This allows for pixel wise inclusion of systematic effects in the analysis.

[Ams+15]

3.4. Plasma effects in the WGTS

In order to reach a final sensitivity of 0.2 eV all systematic effects need to be examined precisely. β -decay and impact ionization of neutral tritium molecules by β -electrons create ions and electrons in the WGTS. Their density is high enough that plasma effects have to be included in the study of systematic effects.

Plasma effects lead to gradients in the electric potential. β -electrons from decays in a higher electric potential will experience a boost in energy, whereas β -electrons from a lower electric potential will experience a retardation. Hence shifts in the electric potential will influence the energy of the β -electrons, therefore shift the integral spectrum and lastly affect the neutrino mass deduction.

An homogeneous plasma potential shifts the entire β -spectrum and can be easily compensated in the analysis. A spatially inhomogeneous plasma potential influences the shape of the β -spectrum and can only be accounted for in the analysis by good understanding of the plasma.

A quantitative examination of the plasma using a Diffusion ansatz was performed in [Kuc+18]. New investigations show that the Diffusion ansatz may not include all significant plasma effects. Thus a new kinetic simulation is being development within the KATRIN collaboration. This master thesis will provide key parameters for the new kinetic studies.

4. Monte Carlo and computation techniques

In Physics, Monte Carlo simulations are used to emulate complex physical problems on computers by dismantling them into their underlying basic processes. These basic processes follow probability distributions, which can in general be gained from experiment or theory.

In Monte Carlo simulations these probability distributions are imitated using random numbers. The creation of uniform pseudo random numbers on computers is covered in section 4.1. The sampling of arbitrary statistical distributions from these uniform random numbers is treated in section 4.2.

In physics Monte Carlo simulations are often used to determine the properties of a complex system by repetitive simulation of single particles in this system. A common approach is a semi-classical Monte Carlo simulation, where particle propagation and interactions between particles is separated.

Particle interactions are treated quantum mechanically and are therefore described by probability distributions. The statistical description of particle interactions is covered in section 4.3. Following an interaction the particle will be deflected by a certain scattering angle. The calculation of the final direction of motion after an interaction is treated in section 4.4.

Propagation of particles is treated classically in semi classical Monte Carlo simulations and is therefore definite. Free propagation without external forces is trivial and determined by conservation of momentum. The trajectory of charged particles in electric and magnetic fields is complex and usually not analytically solvable. Two algorithms for numerical trajectory calculation of charged particles in electric and magnetic field are presented in section 4.5 and section 4.6.

Analogous to real physical experiments, Monte Carlo simulations need high statistics for good results. This requires high wall times. A good way to reduce the computation time is parallel computation. In section 4.7 the Message Passing Interface (MPI) for parallel computing is introduced.

4.1. Random number generation

Random numbers are essential for the quality of a Monte Carlo simulation. Real random numbers can only be obtained from real physical experiments. Thus using these is possible but often not practicable.

Typically, Monte Carlo simulations use Pseudo Random Number Generators (PRNGs), which create numbers using special algorithms. The numbers are random in good approx-

imation. The randomness depends on the algorithm implemented and often scales with computation effort.

The first PRNG was the congruential generator proposed in 1951 [Leh51]. New elements are calculated by

$$x_{k+1} = (a \cdot x_k + b) \bmod M \quad (4.1)$$

where x_0 , a , b and M are initial integer values for the PRNG and $b < M$. Hence values for x are created on $[0, (M - 1)]$. Commonly uniform random numbers η on $[0, 1)$ are required. These can be obtained by

$$\eta = \frac{x}{M}. \quad (4.2)$$

Congruential generators are very memory and computation efficient. However, they are outdated as the maximum length of sequence is strongly limited by the maximum integer number on the system, since the sequence repeats itself, if x_0 is generated again (Equation 4.1).

The proper choice of a , b and M determines important properties of the PRNG such as randomness and length of sequence. For more information about requirements of PRNG see [Hag15]. The seed x_0 of the PRNG initializes the sequence explicitly and makes the simulation reproducible by using the same seed.

The Mersenne-Twister 19937 is a modern PRNG which is commonly used. The algorithm satisfies for randomness, has a long sequence of $2^{19937} - 1$ and the computational effort is very efficient compared to other PRNG algorithms. For details see [Hag15; Kol08]

4.2. Sampling of Random variables

In Monte Carlo simulations PRNG grant access to uniform random numbers η on $[0, 1]$ (section 4.1). Commonly physics follow arbitrary stactical distributions. Using sampling techniques a random quantity x that follows an arbitrary PDF $p(x)$ can be created from uniform random numbers η_i .

PDF describes the statistical properties of a quantity x . The relative probability of observing the quantity within $[a, b]$ is

$$w([a, b]) = \int_a^b p(x) dx, \quad (4.3)$$

where $p(x)$ is the PDF of x . The CDF of $p(x)$ is defined by

$$P(x) \equiv \int_{-\infty}^x p(x') dx' \quad (4.4)$$

and indicates the probability of obtaining a value smaller or equal to x .

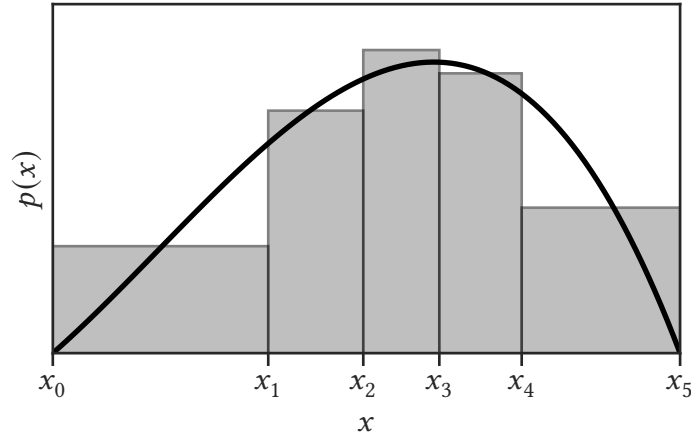


Figure 4.1.: Sketch of the numerical inversion technique. The black solid line represents the PDF and the grey bars represent the bins of equal sizes.

Inverse transform sampling theorem

Following [Kol08] the inverse transform sampling theorem states that a random quantity x that follows the PDF $p(x)$ can be sampled from a uniform random number η by

$$x = P^{-1}(\eta). \quad (4.5)$$

If the CDF $P(x)$ is analytically invertible this approach is the best choice and unmatched in terms of precision and computational effort.

Else $P^{-1}(x)$ can be obtained from numerical inversion of $P(x)$. The PDF is split into N bins of equal size $A = \frac{1}{N}$ (Figure 4.1).

As each bin is equally probable a bin i_x can be sampled by

$$i_x = \text{int}(N \cdot \eta_1) + 1. \quad (4.6)$$

From the bin i_x the value of x can be sampled. Assuming each value within a bin being equal probable the final value for x is sampled from

$$x = x_{i_x, \text{low}} + \eta_2(x_{i_x, \text{up}} - x_{i_x, \text{low}}), \quad (4.7)$$

where $x_{i_x, \text{low}}$, $x_{i_x, \text{up}}$ are lower and upper bin border of bin i_x .

The assumption of values within each bin being constant will lead to divergences from the original $p(x)$. This error can be reduced by increasing the number of bins N but will also lead to higher memory requirement and computational effort.

Rejection method

The Rejection method samples x directly from the surface of the PDF. Therefore the PDF is enclosed by a rectangular frame with borders $[a, b]$ and $[0, p_{\max}]$ (Figure 4.2).

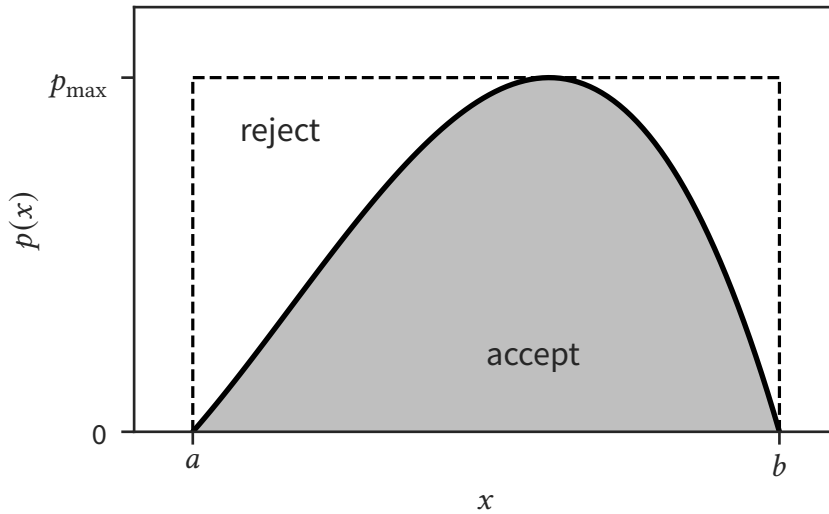


Figure 4.2.: Sketch of rejection method. The black solid line represents the PDF. Values are sampled within $a < x < b$ and $0 < y < p_{\max}$ represented by dotted surface. Values sampled in grey area are accepted and values in white area are rejected.

A random test point (x_t, y_t) in the frame is created by

$$x_t = a + \eta_1 \cdot (b - a), \quad (4.8)$$

$$y_t = \eta_2 \cdot p_{\max}. \quad (4.9)$$

The point is accepted if it is within the PDF

$$y_t \leq p(x_t). \quad (4.10)$$

Else the test point is rejected and a new test point is created. The algorithm is repeated until the condition is met and a point is accepted. Thus a random variable following $p(x)$ is created.

The rejection method models the PDF exactly, but can be very computation intensive. The efficiency e of the method is determined by the ratio of acceptance area to total sampling area:

$$e = \frac{\int_a^b p(x) dx}{p_{\max} \cdot (b - a)}. \quad (4.11)$$

[Hag15; Kol08]

Numerical evaluation

Numerical evaluation is the best method for sampling discrete PDFs (Figure 4.3). Discrete PDFs represent either categoric data or measurement results in histogram form with equidistant x -resolution.

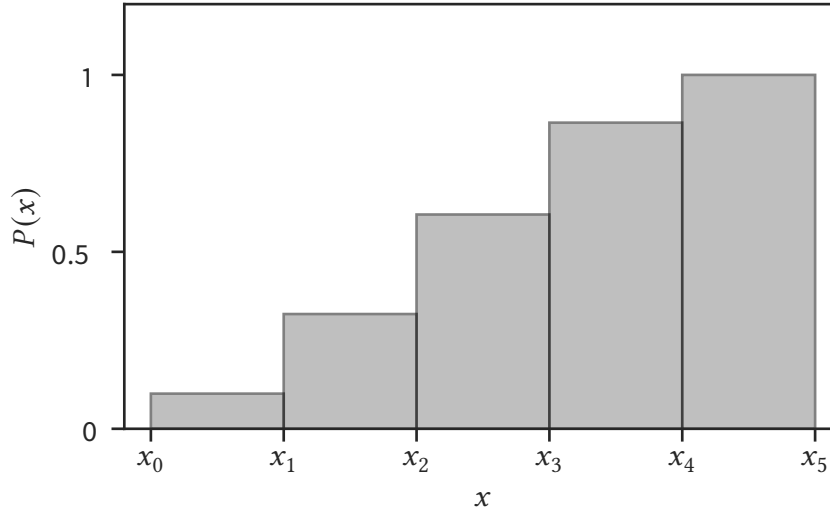


Figure 4.3.: CDF of a discrete histogram with borders x_i .

Let the i -th bin have the CDF-value P_i . A bin i_x can be sampled by searching for

$$P_{i_x-1} < \eta < P_{i_x}. \quad (4.12)$$

Thus for categorical data the corresponding outcome is sampled.

When sampling from histograms the value of x can be returned as value in the bin mid or for more precise resolution linear interpolation can be applied.

The efficiency depends on the number of bins and the search algorithm.

[Hag15; Kol08]

4.3. Particle Interactions

In particle physics interactions are described as point like events. The particles' states before and after the interaction are regarded as free waves. The interaction itself is a complicated quantum physical process determined by any acting force. With the concept of cross sections, this complicated interaction process can be simplified and expressed by the probability of observing a certain final state from a known initial state. Interaction cross sections are obtained from experiment and theory.

Two particle scattering

The Total Cross Section (TCS) is a measure for the probability of an interaction happening between two particles. It is energy dependent and generally measured and modeled in the laboratory system, where the impact particle with energy E hits a fixed target particle. For N_T number of target particles the probability for an interaction is defined by

$$w = \sigma(E) \cdot \frac{N_T}{A}, \quad (4.13)$$

where $\sigma(E)$ is the TCS and A is the surface of the target. Thus the TCS can be interpreted as the effective target surface of a single target particle.

For a constant density of target particles n_T the probability for an interaction after passing a distance x results in

$$w = \sigma(E) \cdot n_T \cdot x. \quad (4.14)$$

From Equation 4.14 the average distance between two interactions, the mean free path (MFP), calculates to

$$\lambda(E) = \frac{1}{\sigma(E) \cdot n_T}. \quad (4.15)$$

For more than one interaction channel (IC) the total MFP results in

$$\lambda_{\text{tot}}(E) = \frac{1}{\sum_i \Sigma_i(E)}, \quad (4.16)$$

where the $\Sigma_i(E) = \sigma_i(E) \cdot n_{T,i}$ are the Macroscopic Cross Sections (MCSs) of the ICs and $n_{T,i}$ the corresponding target particle densities.

Differential cross sections

Following an interaction the particles can result in various final states. These states can be expressed by measurable physical quantities such as a scattering angle or transferred energy.

The statistical distribution for observing a specific outcome x after an interaction can be expressed by the Differential Cross Section (DCS) $\frac{d\sigma}{dx}$. The probability for observing x within a specific range $[a, b]$ is calculated by

$$w = \frac{1}{\sigma} \cdot \int_a^b \frac{d\sigma}{dx} dx, \quad (4.17)$$

where σ is the TCS for the specific IC and is linked to the DCS by

$$\sigma = \int_{x_{\min}}^{x_{\max}} \frac{d\sigma}{dx} dx. \quad (4.18)$$

x_{\min} and x_{\max} are lower and upper limit for the observable x .

Reaction rates

For low energetic and rare interactions TCSs are difficult to measure. Often only reaction rates are accessible. These indicate the number of interactions per unit of time in dependence to number particles involved in the interaction.

For a two species system with densities n_I and n_T the number of interactions within a unit of volume per unit of time is defined by

$$\frac{dn_R}{dt} \equiv k_2 \cdot n_I \cdot n_T, \quad (4.19)$$

where k_2 is the reaction rate for the two particle interaction. For one particle of species I with velocity $v = \frac{dx}{dt}$ the probability for an interaction after moving by x calculates to

$$w = k_2 \cdot n_T \frac{x}{v}, \quad (4.20)$$

With Equation 4.14 this yields to

$$\sigma = \frac{k_2}{v}. \quad (4.21)$$

For ternary interactions, where one particle of species I interacts with two particles of species T the reaction rate k_3 is defined by

$$\frac{dn_R}{dt} \equiv k_3 \cdot n_I \cdot n_T \cdot n_T. \quad (4.22)$$

Thus the TCS and the MCS results in

$$\sigma = \frac{k_3}{v} n_T, \quad (4.23)$$

$$\Sigma = \frac{k_3}{v} n_T^2. \quad (4.24)$$

4.4. Change of particle track by interactions

The scattering angle indicates the deflection of the original trajectory caused by an interaction. It is commonly stated in spherical coordinates with the polar angle θ_0 and the azimuthal angle φ_0 in respect to the initial direction of motion \hat{n} .

This section presents a derivation for the formula for calculating the direction of motion after interaction \hat{n}' following [Hag15]. A full derivation is shown because the source is faulty.

Let the initial direction of the particle be

$$\hat{n} = u\hat{x} + v\hat{y} + w\hat{z}, \quad (4.25)$$

where \hat{x} , \hat{y} and \hat{z} are unit vectors of the simulation code's coordinate system. Transformation to a new coordinate system with unit vectors \hat{x}' , \hat{y}' , \hat{z}' , which satisfy for

$$\hat{z}' = \hat{n}, \quad (4.26)$$

$$\hat{y}' = \frac{\hat{n} \times \hat{z}}{|\hat{n} \times \hat{z}|} = \frac{v}{s}\hat{x} - \frac{u}{s}\hat{y}, \quad (4.27)$$

$$\hat{x}' = \hat{y}' \times \hat{z}' = \frac{-uw}{s}\hat{x} + \frac{-vw}{s}\hat{y} + s\hat{z}, \quad (4.28)$$

$$s = \sqrt{u^2 + v^2} = \sqrt{1 - w^2} \quad (4.29)$$

yields

$$\hat{n}' = \sin \theta_0 \cos \varphi_0 \hat{x}' + \sin \theta_0 \sin \varphi_0 \hat{y}' + \cos \theta_0 \hat{z}'. \quad (4.30)$$

Using the nine identities $\hat{i} \cdot \hat{j}'$ for $i, j = x, y, z$ and parameterizing \hat{n}' in the initial coordinate system as:

$$\hat{n}' = u' \hat{x} + v' \hat{y} + w' \hat{z} \quad (4.31)$$

results in:

$$\begin{aligned} u' &= \hat{n}' \cdot \hat{x} = \left(\frac{-uw}{s} \cos \varphi_0 + \frac{-v}{s} \sin \varphi_0 \right) \sin \theta_0 + u \cos \theta_0 \\ v' &= \hat{n}' \cdot \hat{y} = \left(\frac{-vw}{s} \cos \varphi_0 + \frac{u}{s} \sin \varphi_0 \right) \sin \theta_0 + v \cos \theta_0 \\ w' &= \hat{n}' \cdot \hat{z} = s \cos \varphi_0 \sin \theta_0 + w \cos \theta_0, \end{aligned} \quad (4.32)$$

which allows for easy computation of final direction of motion in the initial coordinate system.

4.5. Boris Push

The Boris Push is the standard algorithm for trajectory calculation of charged particles with relativistic gamma factor $\gamma < 100$ in arbitrary electric and magnetic fields in full kinetic plasma simulations .

A particle with charge q and mass m in an electric field \vec{E} and magnetic field \vec{B} will be affected by Coulomb and Lorentz force resulting in a total force of

$$\vec{F} = q \left(\vec{E}(\vec{x}) + \frac{\vec{v} \times \vec{B}(\vec{x})}{c} \right), \quad (4.33)$$

where (\vec{x}, \vec{v}) denote the particle's phase space coordinates and c the speed of light.

The Boris Push algorithm solves the particle's equation of motion

$$\frac{d^2 \vec{x}}{dt^2} = \frac{d\vec{v}}{dt} = \frac{\vec{F}_L}{m} \quad (4.34)$$

by approximating the time differential dt using a finite time element Δt . Hence the motion follows

$$\frac{\vec{x}_{k+1} - \vec{x}_k}{\Delta t} = \vec{v}_{k+1}, \quad (4.35)$$

$$\frac{\vec{v}_{k+1} - \vec{v}_k}{\Delta t} = \frac{q}{m} \left(\vec{E}_k + \frac{(\vec{v}_{k+1} - \vec{v}_k) \times \vec{B}_k}{2c} \right). \quad (4.36)$$

Typically \vec{x}_k and \vec{v}_k are shifted by half a time step. Hence $\vec{x}_k, \vec{E}_k, \vec{B}_k$ correspond to $t = t_k \equiv k \cdot \Delta t$ and \vec{v}_k corresponds to $t = t_k - \frac{\Delta t}{2}$. Equation 4.35 can be solved straight forward. Equation 4.36 is solved by

$$\vec{v}_{k+1} = \vec{v}^+ + \frac{q}{m} \vec{E}_k \frac{\Delta t}{2}, \quad (4.37)$$

where

$$\vec{v}^+ = \vec{v}^- + (\vec{v}^- + \vec{v}^- \times \vec{h}) \times s \quad (4.38)$$

and

$$\vec{v}^- = \vec{v}_k + \frac{q}{m} \vec{E}_k \frac{\Delta t}{2}, \quad (4.39)$$

$$\vec{h} = \frac{q}{m} \vec{B}_k \frac{\Delta t}{2}, \quad (4.40)$$

$$\vec{s} = \frac{2\vec{h}}{1 + h^2}. \quad (4.41)$$

The change of velocity is calculated by two linear boosts caused by the electric field (Equation 4.37 and Equation 4.39) and a rotation between the two boost caused by \vec{B} (Equation 4.38).

The Boris Push provides a very exact solution for arbitrary electric and magnetic fields if Δt is chosen small enough. The required Δt depends on $\vec{E}(\vec{x})$ and $\vec{B}(\vec{x})$ and determines the computational effort needed for the algorithm. Especially resolving gyro motions requires time steps of $\Delta t \approx \frac{1}{20} \frac{1}{\omega_g}$, where ω_g is the gyro frequency of the particle [Lan12]. This can limit efficiency strongly in high magnetic fields.

[Bor70; Qin+13; ZU18]

4.6. Drift Approximation

A method to overcome the high computational effort needed for the Boris Push algorithm (section 4.5) is the Drift Approximation. It can applied for propagation of charged particles in spatial and time constant magnetic fields.

In absence of electric fields the particle is solely affected by the Lorentz force. The motion can be described as superposition of a linear motion parallel to the magnetic field \vec{B} with velocity v_{\parallel} and a gyration around the magnetic field with velocity v_{\perp} . The gyro frequency calculates to

$$\omega_g = |q| \frac{|B|}{m} \quad (4.42)$$

and the motion of a particle with charge q follows

$$x(t) = x_c + \frac{v_{\perp}}{\omega_g} \cos(\omega_g t), \quad (4.43)$$

$$y(t) = y_c + \text{sign}(q) \cdot \frac{v_{\perp}}{\omega_g} \sin(\omega_g t), \quad (4.44)$$

$$z(t) = z_0 + v_{\parallel} \cdot t, \quad (4.45)$$

where the magnetic field is aligned along the z -axis. z_0 is the initial particle's z -position at $t = 0$ and (x_c, y_c) are the center of the gyro motion.

An electric field E_{\parallel} parallel to the magnetic field leads to a boost of v_{\parallel} following

$$v_{\parallel}(t) = v_{\parallel}(0) + \frac{q}{m} E_{\parallel} t. \quad (4.46)$$

A perpendicular electric field \vec{E}_\perp leads to a constant drift of the center of the gyro motion with

$$\vec{v}_E = \frac{\vec{B} \times \vec{E}_\perp}{B^2}. \quad (4.47)$$

[Nor61; Bla15]

4.7. Parallel computing strategies and the MPI standard

Parallel computing is inevitable for Monte Carlo simulations since good statistics require a high number of iterations.

For Monte Carlo simulations, where the physical environment in the simulation is constant in time, no communication between individual CPU cores is needed. Each core initializes and performs the simulation individually. In the post processing the total results is composed from the individual outputs. Note that different initial PRNG seeds for each core are mandatory. Otherwise the result from each core is identical (section 4.1).

If the physical environment in the simulation is calculated within the simulation, communication between cores is inevitable. The Message Passing Interface (MPI) allows communication across cores in a distributed memory system. All participating cores are initialized in the MPI-world and mapped to individual addresses. Communication between cores is performed using MPI-commands. The command must be met on all participating cores. Hence all participating cores will only continue calculating when all cores have called the corresponding MPI-command. Thus bad implementation of the MPI-commands can drastically reduce simulation performance, as cores might wait for others to call the MPI-command.

[Nie16]

5. The KARL Code

The **KARL** - **KA**trin **WGTS** **electR**on and ion spectrum Monte **CarLo** simulation code was developed from scratch within this thesis to simulate the electron and ion distributions of the WGTS (section 3.2).

The resulting distributions of charged particles are a key factor in the plasma studies of the KATRIN experiment (section 3.4). The current overall plasma simulation strategy for the KATRIN experiment is summarized in section 5.1.

The entire KARL code is implemented in C++ and uses several libraries for optimal efficiency. These and further technical concepts used in KARL are presented in section 5.2.

The basic concept of the simulation is the repetitive physical simulation of single particles. The general simulation strategy is covered in section 5.3 and the simulation of a single kinetic particle with focus on physics is treated in section 5.4. For better comprehensibility in the further discussion the single particle, that is being actively simulated, will be abbreviated by CSP.

The KARL code only simulates one CSP at a time. Hence interactions between particles can not be directly simulated. The implementation of RDFs allows self consistent treatment of particle interactions. These RDFs indicate the density for each particle species and are calculated within the physical simulation of each CSP of the respective species. The calculation and implementation of RDFs is presented in section 5.5.

RDFs only indicate the number of target particles. The overall interaction probability is measured by Macroscopic Cross Sections (MCSs). The calculation of the MCSs for interactions of CSPs with RDFs is covered in section 5.6.

The final electron and ion distributions are obtained using the Logging Barrier Method (LBM). Therefore virtual barriers are implemented throughout the WGTS. Particles passing these barriers are logged. The link between this logged data and the desired electron and ion distribution is presented in section 5.7.

Statistically significant results can only be gained when a large number of particles is simulated. Thus parallel computation is inevitable. The parallelization strategy of the KARL code is presented in section 5.8.

At the beginning of every simulation with KARL a number of simulation parameters allows for adjusting the simulation to one's needs. Throughout this and the subsequent chapter (chapter 5 and chapter 6) the function of each individual parameter will be explained in detail in the respective section. An overall overview of the parameters and details on setting them is given in section 5.9.

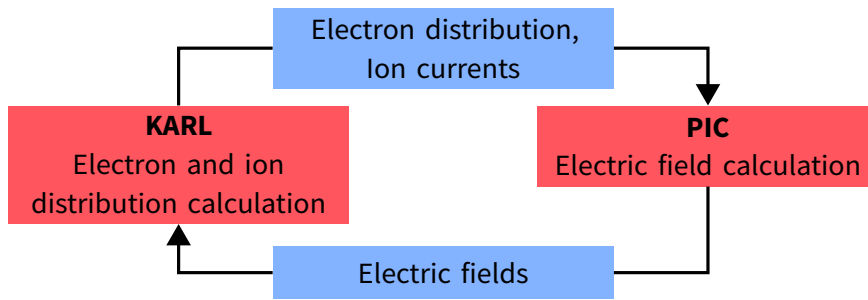


Figure 5.1.: Scheme of the twofold plasma simulation strategy. The KARL code calculates electron and ion distributions in a given electric field configuration and passes these distributions to the PIC code. The PIC code calculates an electric field configuration from electron and ion distributions and passes these electric fields to the KARL code.

5.1. Code intention

In order for the KATRIN experiment to reach the target sensitivity of 0.2 eV, all systematic effects must be well understood. In terms of plasma effects the arising spatial electric fields are of interest (section 3.4). Experimental observation and analytical modeling of plasma effects is only partly possible and not sufficient for final quantification of plasma effects.

Thus simulations are needed to gain an extensive understanding of the plasma. Due to the complexity of the system a full plasma simulation, where electric field calculations and particle interactions are combined, is not feasible. Hence a twofold simulation strategy is chosen (Figure 5.1).

A Particle-in-Cell (PIC) simulation based on the ACRONYM code [KBS12], which will be presented in the scope of a PhD thesis by J. Kellerer, calculates the electric fields arising from charged particles in the WGTS. Electrons are implemented from an initial distribution and are modeled fully kinetically. Ions can not be resolved kinetically due the much larger mass. Since ions are moving much slower than electrons, kinematics of ions on plasma time scales are negligible. Thus ions are implemented as time constant fluxes of charge. The initial electron distribution and constant ion fluxes for the PIC simulation are provided by simulations using the KARL code.

The KARL code simulates all relevant particle interactions in the WGTS to obtain the electron and ion distribution throughout the WGTS. In contrast to the PIC simulation, the KARL code cannot calculate electric and magnetic fields from the particle distributions, as each particle is simulated individually. Thus the KARL code implements constant electric and magnetic fields prior to simulation. These fields are provided from the PIC simulation.

By iterative combination of both simulations, where electric fields from the PIC simulation are implemented into the KARL simulation and in return electron and ion distributions from the KARL simulation are implemented into the PIC simulation, a equilibrium state will be reached. This equilibrium state yields a detailed map of electric fields due to plasma effects throughout the WGTS. These fields can be taken into account in the neutrino mass deduction.

5.2. Technical details

The entire KARL code is implemented in C++11. C++ provides high computation efficiency, allows for easy optimizations and has many libraries specialized on scientific tasks. Additionally, C++ allows for runtime and compile time polymorphism. This allows for very efficient implementation of various interactions and proper handling of different particle species at runtime.

Vector operations and Random Number Generator (RNG) are handled using the Blitz++ [Vel00] library. For the RNG, Blitz++ uses an adaption of the Mersenne-Twister 19937 algorithm (section 4.1).

Output is written in HDF5 format [The19] using the Table API of the corresponding library. This allows for efficient memory usage and optimized writing speed. Additionally the KARL code buffers output internally to optimize IO-speed.

The parallelization strategy of KARL (section 5.8) uses a distributed memory system. This is realized using Open MPI [Gab+04], allowing for communication between cores (section 4.7).

Throughout the entire KARL code linear and logarithmic binning of physical quantities is used. Efficient memory access is only possible if each quantity is directly mapped to an address. For a linear scale of a quantity x , that is binned into n_x bins on $[x_{\min}, x_{\max}]$ the corresponding index of the memory address can then be calculated from

$$i_x = \text{ceil}\left(\frac{x - x_{\min}}{\Delta x}\right) - 1, \quad (5.1)$$

where $\Delta x = \frac{x_{\max} - x_{\min}}{n_x}$ is the width of each bin. Logarithmic binning is obtained from logarithmizing x , x_{\min} and x_{\max} .

Internally the KARL codes uses a Cartesian coordinate system with coordinates x, y, z . The z -axis is aligned along the magnetic field lines. Positive z - direction points towards the spectrometers and negative z -direction towards the RW. For the exact definition of the Cartesian coordinate system see section 6.1. For certain application the use of cylindrical coordinates r, φ, z is handy. These are linked to the Cartesian coordinate system by

$$\begin{aligned} x &= r \cdot \cos(\varphi) \\ y &= r \cdot \sin(\varphi) \\ z &= z. \end{aligned} \quad (5.2)$$

The entire KARL code uses classical energy-velocity relation $E = \frac{m}{2}v^2$, as particles of interest are non relativistic. Thus transformation of coordinate systems is calculated using Galileo transformation.

5.3. Simulation strategy

KARL simulates the electron and ion distribution in the WGTS (section 3.2) by repetitive kinetic simulation of single particles.

As explained in section 5.1 electric and magnetic fields are implemented prior to simulation as time constant numeric fields. The density and velocity profile of molecular tritium

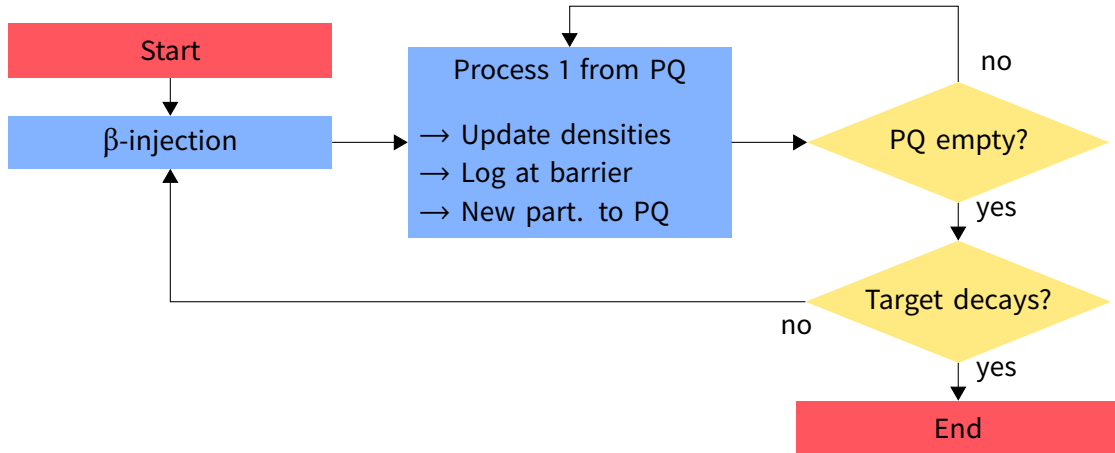


Figure 5.2.: Flowchart of the simulation algorithm. Algorithm starts with injection of one β -electron. Consecutively the β -electron and all arising particles are being simulated. New β -decays are performed until the number of target decays is reached. PQ: Particle Queue.

T_2 is implemented as time constant because kinetic simulation exceeds the computation budget and variations of T_2 -distribution caused by effects treated in the simulation are negligible. For details on the implementation of the WGTS and T_2 see section 6.1.

The starting point of the simulation is a β -decay injecting an energetic β -electron into the simulation (Figure 5.2). By processes such as ionization new particles are created within the physical simulation of the β -electron. This actual physical simulation is covered in section 5.4.

Particles created within the physical simulation are stored in the Particle Queue (PQ) and are processed subsequently. Implemented particle species that are simulated kinetically are e^- , T^+ , T_2^+ , T_3^+ , T_5^+ . Higher order of tritium ion clusters are not implemented as their properties resemble T_5^+ (section 6.5). Further particle species can be easily added in further version of KARL if found necessary.

As long as the PQ is filled, particles from the PQ are physically processed one by one. New CSPs are selected from the PQ randomly to reduce correlation effects.

Once all particles emerging from one β -electron, including particles from secondary and higher order particles, are processed, a new β -electron is injected and the algorithm is repeated.

This process is repeated until the target number of β -decays is reached. The target number of β -decays is set by the DECAYS parameter.

By repeating the process a time integration is performed. The total simulation time T_{sim} is linked to the β -decay activity A_β and the total number of β -decays N_β performed in the simulation and calculates to

$$T_{\text{sim}} = \frac{N_\beta}{A_\beta}. \quad (5.3)$$

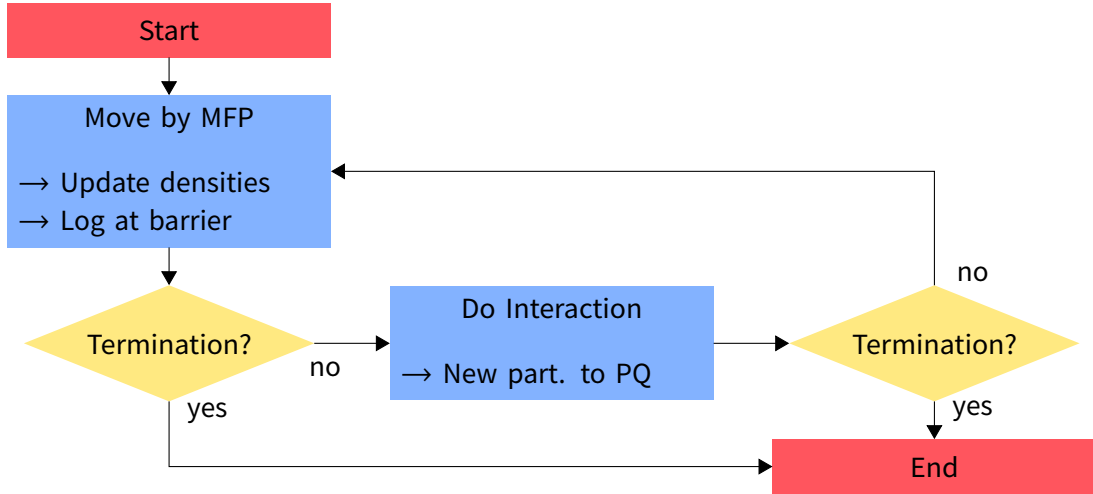


Figure 5.3.: Flowchart of the physical simulation algorithm for a CSP. Particles simulation alternates between propagation by the mean free path (MFP) and performing interactions until a termination condition is met.

5.4. Simulation of the Current Simulation Particle (CSP)

For the physical simulation of the Current Simulation Particle (CSP) a semi classical approach is chosen. An overview of the algorithm is displayed in Figure 5.3.

Particles for the physical processing emerge from either β -decay or are created within this physical simulation from another CSP by processes such as ionization.

The semi classical approach processes propagation and interactions separately. In alternation the CSP is propagated classically by its MFP and interacts afterwards with one RDF. Between and during each step the CSP's properties are checked for physical and simulational termination.

In the subsequent subsections all relevant processes are described in detail with focus on the realization of physical laws.

β -Injection

The probability for a β -decay scales linear with the T_2 -density. The implemented T_2 -density is only dependent on the longitudinal position z and is independent from the polar coordinates r , φ (section 6.1). Thus r and φ are sampled using the inverse sampling theorem for uniform distributions (Equation 4.5) resulting in

$$r = \eta_1 \cdot r_{\text{WGTS}}, \quad (5.4)$$

$$\varphi = \eta_2 \cdot 2\pi, \quad (5.5)$$

where $\eta_{1,2}$ are uniform random numbers on $[0, 1)$ and r_{WGTS} is the radius of the WGTS. The longitudinal position z is sampled from the implemented T_2 -density using rejection method (section 4.2).

The energy of the β -electron is sampled from the β -decay spectrum (Equation 2.19) also using rejection method (section 4.2). The effect of the neutrino mass on the entire

β -spectrum is negligible. The initial direction of motion is assumed to be isotropic. Thus it is sampled analogous to Equation 5.4.

The usage of rejection method at this point does not reduce efficiency, since β -injection is only performed scarcely in comparison to the number of operation for each CSP simulation times the number of secondary particles.

Ions emerging from β -decays are implemented as thermal T_2^+ (section 6.5). Thus the initial momentum is sampled from the T_2 -distribution. Kinetic ions and other decay channels are not included in the simulation (section 6.5).

Further injection methods beside β -injection are implemented in KARL for testing purposes. The injection of the tritium ions can be muted with the INJ_TI parameter, where 0 deactivates and 1 activates the injection.

By specifying the INJECTION and INJ_E parameter further energy spectra for the initial electrons are definable. The default method for sampling from the β -spectrum is INJECTION = 0. In this case the INJ_E parameter is ignored. For INJECTION = 1 all electrons are injected with constant energy. Here the INJ_E specifies the energy in eV. INJECTION = 2 injectes the electrons from a Maxwell Boltzmann distribution. The temperature T of the distribution is linked to the energy specified by the INJ_E in eV through $E = k_B T$. k_B is the Boltzmann constant.

Propagation

Propagation of CSPs is performed classically by one mean free path (MFP) λ . The MFP specifies the average length of propagation between interactions and is calculated from the total MCS (Equation 4.16). The calculation of MCS is covered in section 5.6 and depends on the implemented interaction channels. These are presented in chapter 6.

For calculating propagation the Boris Push algorithm (section 4.5) and the Drift Approximation (section 4.6) are implemented in KARL. Drift Approximation is recommended, as the computation efficiency is drastically increased and the simulation is performed in a constant magnetic field. Both solvers allow for propagation of charged particles in electric and magnetic fields. The solver can be specified using the PROPAGATION parameter. For PROPAGATION = 0 the Drift Approximation is used and for PROPAGATION = 1 Boris Push is used. If Boris Push is chosen additionally the parameter BORIS_T needs to be set. This specifies the time stepping of the Boris Push algorithm.

Particles reaching the RW or radial walls of the WGTS during propagation are passed to the terminator and terminated from physical simulation. The boundary condition in positive z direction differ for electrons and ions. Ions are removed from the simulation at this point (section 3.2), whereas electrons are reflected. The number electrons that surpass the spectrometers and reach the detector during operation of the KATRIN experiment is negligible.

During each propagation step the RDFs are updated (section 5.5) and CSPs passing a Logging Barrier are tracked (section 5.7).

Interaction

At every interaction step only one interaction is performed. Thus in the first step an IC must be sampled. The probability for each IC is

$$w_i(E) = \frac{\Sigma_i(E)}{\Sigma_{\text{tot}}(E)}, \quad (5.6)$$

where $\Sigma_i(E)$ is the MCS of corresponding IC and $\Sigma_{\text{tot}}(E)$ the total MCS. Since each $w_i(E)$ represents the probability of observing a discrete IC a resulting IC is sampled using numerical evolution (section 4.2). Calculation of MCSs is covered in section 5.6.

Once an IC is sampled the interaction is performed by sampling an interaction partner from the corresponding RDF and by sampling the physical properties of the interaction from the corresponding DCSs. From these data the final state of the CSP after interaction is calculated and set. Detailed information on the implemented models for each IC is given in chapter 6. Here an overview of mathematical and simulational methods is given.

Elastic scattering For elastic scattering the scattering angles ϑ , φ and the initial momenta of the two interaction partners specify the kinematics of the process. The initial momentum of the active particle is well known and the momentum of the secondary particle is sampled from the corresponding population. The scattering angles are sampled from the corresponding DCSs. The calculation of final kinematics is performed following [LL11] and Equation 4.32.

Ionization In case of electron impact ionization, the primary electron transfers enough energy to a bound secondary electron so that it can overcome the binding energy of its atom or molecule. Thus impact ionization is only possible if the primary electron's initial energy E_{tot} exceeds the binding energy B . Following the process a second free electron and an ion are created, which are appended to the PQ. Due to the sheer number of degrees of freedom the process can not be fully specified by DCSs. It is assumed that the ion adopts the properties of the atom/molecule. The energy of the secondary electron E_2 is sampled from the corresponding DCS. Generally conservation of energy must be satisfied:

$$E_{\text{tot}} = E_1 + E_2 + B, \quad (5.7)$$

where E_1 is the energy of the initial electron after the interaction. Direction of momenta of primary and secondary electron after interaction are sampled from the corresponding DCSs.

Excitation A very efficient IC for cooling electrons are excitations of the atoms or molecules. In these processes the CSP-electron loses a quantized amount of energy in order to excite a certain excitation level of the atom/molecules. Generally it is assumed that no further energy is being transferred. Thus the electron's final energy is specified by the initial energy and the excitation level. The final direction of motion is sampled from the corresponding DCS.

Table 5.1.: Overview of all possible termination channels.

label	description
n_rw	Termination at RW (negative z)
n_dipole	Termination at dipoles (positive z)
n_radial	Termination at WGTS walls (radial)
n_max	Termination due to maximum interaction
n_energy	Termination due to too low energy
n_reaction	Termination by interaction

Recombination Low energetic electrons and ions can recombine to form neutral atoms or molecules. This leads to the termination of physical simulation. Since electrons and ions are simulated kinetically the process must be implemented for both species symmetrically.

Cluster formation Low energetic ions can cluster up with neutral molecules and form cluster ions. Since ions and molecules are only implemented thermally (section 6.5) the resulting cluster can be initialized from the CSP.

Termination

Physical termination by wall interactions or particle interactions are handled during the processing of propagation and interaction. Additional simulational termination conditions are implemented in order to prevent continuous loops and excessive computational effort.

The TERM_E parameter allows for specifying a minimum threshold energy in eV, removing CSP with lower energies. The TERM_MAX parameter defines a maximum number of interactions before each CSP is terminated. The TERM_DI_E parameter allows to set a threshold energy in eV for termination at positive z-direction. In normal operation electrons are reflected at this point. Electrons with lower energies than this threshold are terminated.

In high quality simulations the number of non physical terminations should be negligible. To guarantee this, statistics about the termination channels is tracked. All possible loss channels and corresponding labels are summarized in Table 5.1.

5.5. Runtime Density Field (RDF)

Runtime Density Fields (RDFs) are implemented to indicate the densities of all particles. The RDFs are calculated during simulation of each CSP and therefore make the simulation self consistent. Only the T₂-RDF is implemented as a constant prior to simulation (section 6.1).

The runtime calculation of RDFs during the CSP simulation is done by accumulation of time spend within each bin of the corresponding RDF. The density of that bin then calculates to

$$n = \frac{1}{V} \cdot \frac{t_c}{t_{\text{sim}}(n_\beta)}, \quad (5.8)$$

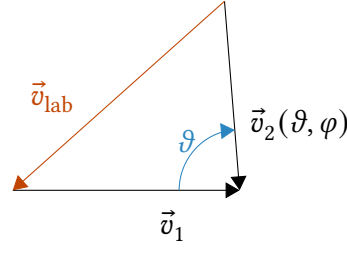


Figure 5.4.: Sketch of shift from simulation coordinate system to laboratory frame. \vec{v}_1 is the velocity of bombarding particle in the simulation system. $\vec{v}_2(\vartheta, \varphi)$ is the velocity of the target particle in the simulation system. In the simulation integration over all possible ϑ and φ is performed. The integration is independent of φ . ϑ is displayed in blue. The resulting velocity of the bombarding particle is displayed in red and labeled as \vec{v}_{lab} .

where V is the volume of the bin, t_c the cumulated time spend in the bin and t_{sim} the current simulation time. The current simulation time is calculated by the decay activity A_β and the current number of β -decays n_β using

$$t_{\text{sim}}(n_\beta) = \frac{n_\beta}{A_\beta} \quad (5.9)$$

The RDFs are spliced into multiple spatial bins using cylindric coordinates. Setting of the POP_N_Z, POP_N_R, POP_N_PHI parameters allows for specifying the number of bins in z , r and φ .

Ion RDFs are implemented without energy resolution. They adapt the velocity-distribution of T_2 . This is a superposition of a constant drift speed \vec{v}_{drift} and an isotropic Maxwell-Boltzmann distribution specified by WGTS temperature and mass of species particle (section 6.1).

The electron RDF is additionally sliced into energy bins. Here logarithmic binning is used. The number of energy bins is specified by the POP_N_E parameter, the lower end of the scale is specified by the POP_E_START parameter and the upper limit by POP_E_END.

A number of pre-run decays to reach equilibrium before taking statistics can be set using the POP_DECAYS and POP_STEP parameters. POP_DECAYS is the total number of decays to perform before the actual run. The POP_STEP parameters specifies the number of β -injections to performe on each core before synchronizing the density fields across all cores (section 5.8).

5.6. Macroscopic cross section (MCS) calculation

The Macroscopic Cross Section (MCS) $\Sigma_{\text{tot}}(E)$ is a measure for the interaction probability of a CSP. In the simulation MCSs determine the distance of free propagation between each interaction and are essential for performing interactions (section 5.4).

The total MCS is obtained by summation over the MCSs $\Sigma_i(E)$ of all possible interaction channels (ICs) connected to the CSP:

$$\Sigma_{\text{tot}}(E) = \sum_i \Sigma_i(E). \quad (5.10)$$

The MCS of one specific IC is defined as product of the corresponding microscopic TCS σ_i and density of interaction partner n_i for this IC:

$$\Sigma_i(E) = \sigma_i(E_{\text{lab}}) \cdot n_i(\vec{x}), \quad (5.11)$$

where E_{lab} is the energy in the laboratory frame and \vec{x} the position of the CSP. The density of interaction partners $n_i(\vec{x})$ are obtained from the RDF and the TCS $\sigma_i(E_{\text{lab}})$ from the implemented theory. Generally TCSs are described in the laboratory system, where a kinetic bombarding particle with energy E_{lab} approaches a fixed target particle. In the MCS calculation it must be differentiated whether the CSP is bombarding or target particle in the TCS definition.

The actual models implemented for specific TCSs are presented in chapter 6. In the following methods for calculating the TCS for different matches of CSPs and RDFs with consideration of the laboratory frame definition are discussed. This calculation of the TCS is nontrivial, as the RDFs do not exactly specify a direction of motion and thus integration must be performed.

The drift speed of thermal RDFs has a well defined direction. This can be considered, by transformation to a frame, where the target RDF is at rest. This transformation is done prior the further calculations is therefore not explicitly stated in the following.

Then neither thermal nor kinetic RDFs specify the direction of their particles. Thus an isotropic distribution is assumed. For the calculation of the TCS the possible constellations between the velocity of a CSP $\vec{v}_1 = \hat{n}_1 \cdot v_1$ and the velocity \vec{v}_2 of a interaction partner from RDF must be considered. \vec{v}_2 can be parameterized using $\vartheta = [0, \pi[$ and $\varphi = [0, 2\pi[$ in respect to \hat{n}_1 (Figure 5.4), which results in

$$\vec{v}_2(\vartheta, \varphi) = v_2 \cdot \hat{n}_1 \cdot \begin{pmatrix} \sin(\vartheta) \cos(\varphi) \\ \sin(\vartheta) \sin(\varphi) \\ \cos(\vartheta) \end{pmatrix}. \quad (5.12)$$

Shifting to the laboratory frame, where the CSP is the bombarding particle yields

$$\vec{v}_{\text{lab}}(\vartheta, \varphi) = \vec{v}_1 - \vec{v}_2(\vartheta, \varphi), \quad (5.13)$$

$$E_{\text{lab}}(\vartheta) = \frac{m}{2} \cdot |\vec{v}_{\text{lab}}(\vartheta, \varphi)|^2 = \frac{m}{2} \cdot \left(v_1^2 + v_2^2 - 2v_1v_2 \cos(\vartheta) \right), \quad (5.14)$$

where m is the mass of the CSP. Since Equation 5.14 is independent of φ the TCS results in

$$\sigma(v_1, v_2) = \frac{1}{\pi} \int_0^\pi d\vartheta \sigma(E_{\text{lab}}(v_1, v_2, \vartheta)). \quad (5.15)$$

In the KARL code this one dimensional integral is solved numerically using Simpson's rule following [Pre+92].

The opposite laboratory frame definition, where the CSP is the target particle, can be easily adjusted by redefinition of m due to the symmetry of Equation 5.14. In that case m is the mass of a RDF particle.

For interactions of the CSP with a kinetic RDF, the absolute velocity v_2 is determined by the energy bin. Thus the MCS of a particular energy bin is obtained using Equation 5.15 and multiplying with the density of corresponding energy bins. The total MCS for that IC is obtained by summation over all energy bins.

For interactions with thermal density fields the underlying Maxwell Boltzmann distribution must be considered. Integration over the v_2 distribution must be performed and the TCS results in

$$\sigma(v_1) = \frac{1}{\pi} \int_0^\pi d\vartheta \int_0^\infty dv_2 f_{\text{MB}}(v_2) \cdot \sigma(E_{\text{lab}}(v_1, v_2, \vartheta)). \quad (5.16)$$

This two dimensional integration is solved using Simpson's rule on a rectangular grid following [Pre+92]. The infinite upper bound of the velocity integral is approximated using

$$v_{2,\text{up}} = 3 \cdot \sqrt{\frac{2k_{\text{B}}T}{m_t}}, \quad (5.17)$$

which represents 99.96 % of the integral.

For higher computational efficiency, integration is ignored, if either one of the velocities is much larger than the other. In that case Equation 5.14 can be replaced using the classical energy-velocity relationship. In the simulation this condition was formulated as

$$v_{\text{u}} > 2000 \cdot v_{\text{l}}, \quad (5.18)$$

where v_{u} is the velocity of the fast particle and v_{l} of the slow. The factor 2000 represents a ~1 % variation of the laboratory energy during ϑ integration in Equation 5.14. For comparison with thermal RDFs the velocity corresponding to $k_{\text{B}}T$ was used.

The integration precision can be increased by splitting the integration range into equal sized bins. The INT_N_INTPOINTS parameter specifies the number of bins. The integration is then performed in each bin and totaled up afterwards. This parameter also specifies the number of points in each direction of the rectangular grid used for the two dimensional integration.

Calculation of the MCS is among the most performed operations in the KARL code. Runtime calculation of integrals is very costly. Hence KARL provides the option to precompute the integrals. Since temperature of WGTS and properties of energy bins of kinetic RDFs are set prior to simulation the integral only depends on the energy of the CSP. Setting INT_PRE_START and INT_PRE_END parameter define the lower and upper end for the precomputed energy scale and the INT_PRE_N specifies the number of precomputed points. The precomputed energies are calculated on a logarithmic scale.

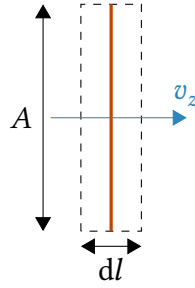


Figure 5.5.: Sketch of a particle with longitudinal speed v_z passing a Logging Barrier. The particle is displayed in blue. The Logging Barrier is displayed as thick red line. Dashed box with surface A and thickness dl represent volume the particle passes with constant speed v_z . Velocity components of the particle parallel to the Logging Barrier are not displayed in this sketch.

5.7. Logging Barrier Method

Using the Logging Barrier Method (LBM), particle densities and fluxes with high energy resolution are obtained at predefined z -positions in the WGTS. The positions are specified by the LOG_BARS parameter, which indicate the number of Logging Barriers. The barriers are evenly spaced in the WGTS including the minimum and maximum z -value. If LOG_BARS = 1 only particles reaching the minimum z -value (RW) are logged.

During each propagation step of a particle the simulation checks whether a Logging Barrier was passed and if a barrier was passed, the phase-space coordinates (\vec{x}, \vec{v}) of the particle are written to the output. From this data detailed particle densities and particle fluxes can be calculated in the post processing. This calculation will be shown in the following.

The contribution of a single particle to the total density n_i can be calculated from its longitudinal speed $v_{z,i}$. When treating a Logging Barrier as a three dimensional disk with thickness dl and surface A , the particle spends the time $dt_i = \frac{dl}{v_{z,i}}$ in the volume $dV = dl \cdot A$ (Figure 5.5). Thus the density in respect to the total simulation time T_{sim} of one particle results in

$$n_i = \frac{t_i}{V \cdot T_{\text{sim}}} = \frac{1}{A \cdot T_{\text{sim}} \cdot v_{z,i}} \quad (5.19)$$

The total density is obtained by summing over all density contributions. The differential spectrum in energy $\frac{dn}{dE}$ is obtained by grouping the data in energy bins prior summation and normalizing by the bin width. For better statistics logarithmic binning is recommended.

The longitudinal particle flux j_z is obtained by counting the number of particles passing the barrier with respect to the passing direction. The total flux results in

$$j_z = \frac{N_+ - N_-}{A \cdot t_{\text{sim}}}, \quad (5.20)$$

where N_+ is the number of particles with positive v_z and N_- with negative v_z . The differential particle flux $\frac{dj_z}{dE}$ is obtained analogous to the differential density $\frac{dn}{dE}$ calculation.

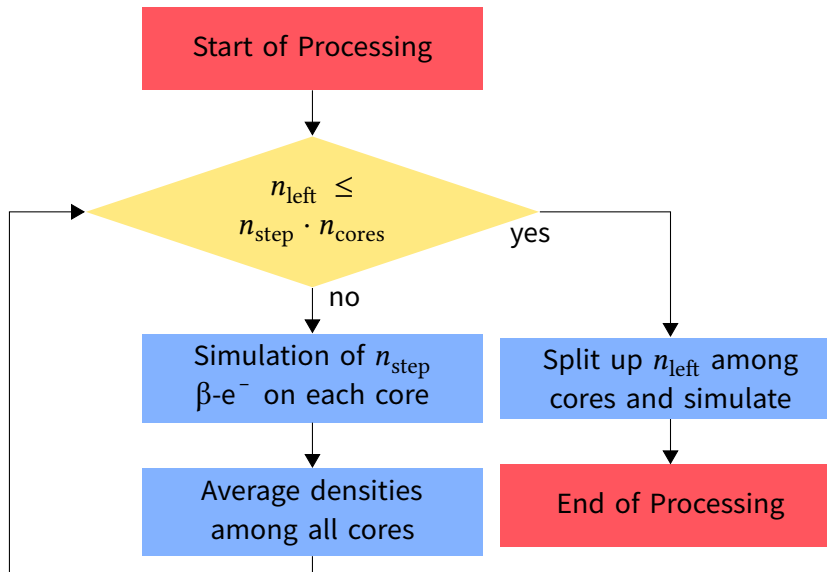


Figure 5.6.: Flowchart of the parallelization strategy of the KARL code. n_{left} is the number β -decays left until reaching the number of target decays. n_{step} is the number β -decays that are simulated on each core before synchronizing the RDF and n_{cores} is the number of cores used for the simulation.

5.8. Parallelization strategy

A high number of β -decays is needed to obtain statistically significant results. Therefore parallelization of the KARL code is inevitable.

Classical Monte Carlo parallelization strategy is not feasible for KARL, since the simulation of CSP depends on the RDF. Thus an adaption to the classical parallelization strategy is used for KARL. Here the RDFs are averaged over all cores after a fix number of β -decays on each core (Figure 5.6) before continuing the simulation. This stepping size before synchronizing is specified by the STEP parameter.

The actual communication in KARL is performed using MPI_ALLGATHER commands (section 4.7). For statistically uncorrelated results the RNGs of each core must be initialed with different seeds. Each core initializes its seed depending on the SEED parameter and its MPI rank. Thus same SEED parameters and same number of cores yields the same simulation results.

5.9. Simulation parameters

Setting simulation parameters allow for adjustment of the simulation. The function of each parameter is discussed in this and the subsequent chapter (chapter 5 and chapter 6) in the respective sections. An overview of all simulation parameters is displayed in Table 5.2.

Parameters are passed to the simulation using a parameter file. The location of the file is passed by setting the environment variables "parpath" and "parfile", where "parpath" is the path to the directory containing the file and "parfile" specifies the name of the file.

A parameter is set in the file by starting a row with the name of the parameter and specifying the parameter value with whitespace delimiter. Empty rows or rows starting with '#' are ignore. Also '=' and ';' are ignored. A sample parameter file using recommended parameters is displayed in Listing A.1.

Table 5.2.: Overview of simulation parameters with recommendation for KATRIN parameters in measurement mode.

Parameter	Rec.	Description
SEED		Seed of PRNG (section 4.1)
POP_DECAYS		Number of decays for initial population calculation
POP_STEP		Stepwidth for initial population calculation
DECAYS		Number of target β -decays
STEP	14	Stepwidth before synchronizing densities across cores
LOG_BARS		Number Logging Barriers
PROPAGATION	0	0 = Drift app. (section 4.6), 1 = Boris Push (section 4.5)
BORIS_T	10^{-9}	Step width for Boris Push in s
BFIELD	2.5	B in T in z
T2_MAXDENS	5×10^{21}	Peak density at $z = 5$
TEMP	30	Constant temperature of the WGTS
T2_VELO	-1	-1 = data from [Kuc+18], else const v in z in m s^{-1}
INJECTION	0	0 = β -decay, 1 = Delta, 2 = MB
INJ_E		Injection energy in eV
INJ_TI	1	ion generation by decay, 0= off, 1= on
TERM_E	10^{-7}	Energy threshold for terminating particles
TERM_DI_E	0	Energy threshold for electron termination at $z = 10$
TERM_MAX	10^6	Maximum number of interactions before termination
eT2_ELA	1	elastic scattering - 0: off, 1: on
INT_ELA_DIR	0	DCS model for ela. sca. - 0: from [SJP05], 1: 4π , 2: 0π
eT2_ION	1	ionization - 0: off, 1: model from [JRS03], 2: model from [KR94]
eT2_ROT	1	rot. exc. - 0: off, 1: unimplemented, 2: from [Yoo+08]
eT2_VIB	1	vib. exc. -0: off, 1: from [JRS03], 2: from [Yoo+08]
eT2_EL	1	T_2 el. exc. - 0: off, 1: from [JRS03], 2: from [Yoo+08]
eT2_REC	1	recombination - 0: off, 1: on
INT_N	100	Number of points for numeric integration
INT_PRE_START	10^{-7}	Start energy for precomputed TCS in eV
INT_PRE_END	1	End energy for precomputed TCS in eV
INT_PRE_N	5×10^3	Number of precomputed TCS values
POP_N_R	5	Number of r -bins for density fields
POP_N_PHI	1	Number of φ -bins for density fields
POP_N_Z	13	Number of z -bins for density fields
POP_N_E	50	Number of energy bins for density fields
POP_E_START	10^{-7}	Minimum energy for kinetic density fields
POP_E_END	2×10^4	Maximum energy for kinetic density fields

6. Modeling of the WGTS and of particle interactions

The replication of actual physical experiments by numerical simulations is always accompanied by deviations from the reality. Thus with every implemented model, divergences from the real setup are implemented. These arise from lack or bad quality of theory, misinterpretation of the experimental setup or from limits due to excessive computational effort. Nevertheless, simulations allow to gain a profound understanding of the real experiment. Therefore it is essential to be aware of the assumptions and approximations made during the implementation of the experimental setup and physics in the simulation. In this chapter models and assumptions made during the implementation of the WGTS and its physics into the KARL simulation are covered. In section 6.1 the model of the WGTS as implemented in KARL is presented.

For simulating the physics in the WGTS, particle interactions are of particular interest. The most common interactions are performed between electrons and tritium molecules. The therefore implemented interactions and connected models are presented in section 6.2.

Further interactions are performed between electron and tritium ions. Due to the low densities of both species, only significant interaction are considered. In this context these are electron-ion recombination, which are presented in section 6.3.

For the kinetic simulation of tritium ions interactions with molecular tritium are very important. These are covered in section 6.4.

Generally the implementation of tritium ions is extremely challenging and some assumptions had to be made. An overview and justification of these assumptions is presented in section 6.5.

Throughout this chapter the function of specific simulation parameters is discussed in the respective section. For general information on simulation parameters see section 5.9.

6.1. Implementation of the WGTS

Geometrically the WGTS is implemented as a 13 m long cylinder with 45 mm radius (Figure 6.1). The z -axis of the simulation's Cartesian coordinate system (section 5.2) is aligned along the length of the tube. One unit of Cartesian coordinates represent 1 m in the real experimental setup. The orientation of x and y axis are chosen arbitrarily since no radial effects are implemented in KARL.

Towards negative z -values the WGTS is terminated by the RW at $z = -3$. The tritium inlets are positioned at $z = 5$ and the Turbo Molecular Pumps (TMPs) are set to be at $z = 0$ and $z = 10$. The toroidal walls of the WGTS are defined at $r = 0.045$. At $z = 10$,

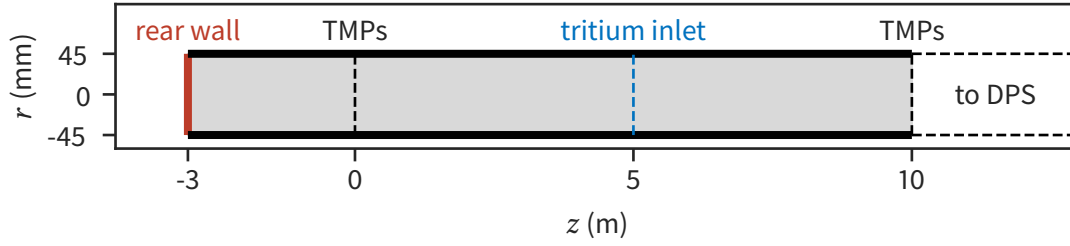


Figure 6.1.: Sketch of the geometrical implementation of the WGTS for the KARL simulation. The simulation area is marked in gray. The WGTS has a length of 13 m and a radius of 45 mm. The RW is positioned at $z = -3$, the Turbo Molecular Pumps (TMPs) are set at $z = 0$ and $z = 10$, the tritium inlet at $z = 5$. The scaling of z -axis and r -axis is chosen arbitrary here.

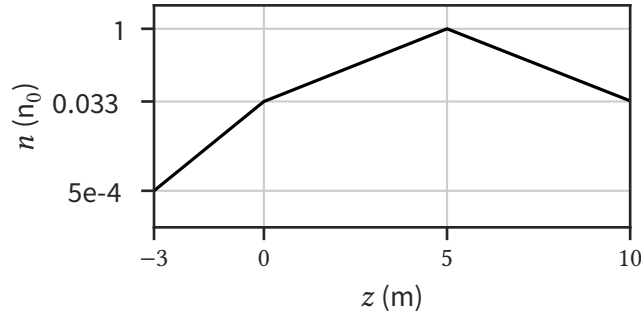


Figure 6.2.: Longitudinal course of the molecular tritium density profile over the length of the WGTS. The densities are calculated in respect to the maximum density n_0 at $z = 5$. The reduction factors are obtained from [Kuc+18].

the maximum z -value, electrons are reflected and ions removed from the simulation (section 5.4)

The T_2 distribution is not calculated during runtime but implemented as constant prior to simulation. The density profile was adapted from [Kuc+18]. For this the reduction factors in respect to the maximum density in the center of the WGTS were implemented and linearly interpolated (Figure 6.2). The reference reduction values were implemented at $z = -3, 0, 5, 10$. The peak density at $z = 5$ is specified by the `T2_MAXDENS` parameter in m^{-3} .

The T_2 velocity distribution is composed of a drift velocity and a thermal distribution. The thermal component is implemented as Maxwell Boltzmann distribution. The temperature of this Maxwell Boltzmann distribution is specified by the `TEMP` parameter. The drift component is specified by the `T2_VELO` parameter. For a value of `T2_VELO = -1` (sic!) the simulation results from [Kuc+18] are implemented between $0 \leq z \leq 10$ and a non moving distribution for $z < 0$. Setting other values for `T2_VELO` specify a constant drift speed in m s^{-1} throughout the WGTS in positive z -direction.

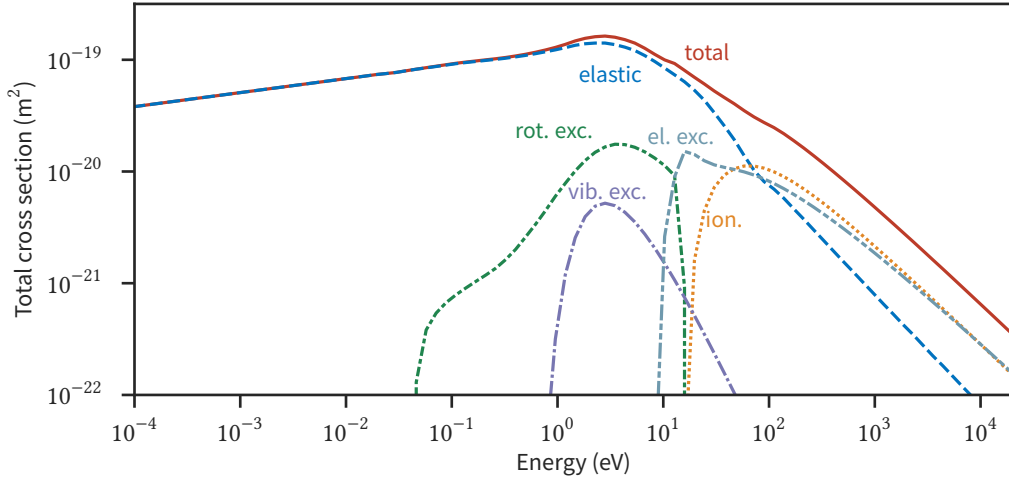


Figure 6.3.: Overview of implemented e^- - T_2 interactions. Displayed ionization and excitation TCS are summed over all sub channels. Energies defined in laboratory frame, where kinetic electrons interact with fixed tritium molecules.

Electric and magnetic fields of the WGTS are implemented prior to simulation. A constant magnetic fields in positive z -direction can be specified by the BFIELD parameter in T. The interface for the electric field integration is not fully specified as it depends on the PIC simulation's output format (section 5.3). In this version of the KARL code the electric potential can be read from a whitespace delimited csv-file, where the WGTS is binned into linear cylindrical bins.

General information on the WGTS can be found in section 3.2 and in [KK05; Ha17; Kuc16; Kuc+18].

6.2. Interactions of electrons with tritium molecules

The plasma of the WGTS arises from energetic β -electrons with energies of up to 18.6 keV. In contrast, the molecular tritium background has a temperature of 30 K, which corresponds to energies of 2.6 meV. Thus e^- - T_2 interactions need to satisfy on a large energy range. Density wise the WGTS is dominated by molecular tritium. Hence interactions with molecular tritium are very probable and all possible interactions need to be modeled precisely.

In the following subsections the implemented models for e^- - T_2 interactions are presented in detail. Since data and models for e^- - T_2 interactions are scarce, models for e^- - H_2 interactions are adopted. Throughout this section the laboratory energy E_{lab} definition implies a bombarding electron hitting a fixed tritium molecule (section 5.6). An overview for all implemented models is displayed in Figure 6.3.

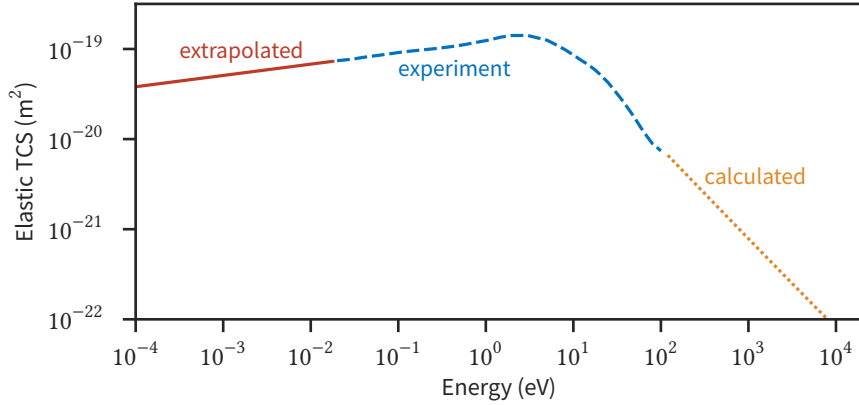


Figure 6.4.: Visualization of the composition of the TCS of e^- - T_2 elastic scattering. The TCS is composed of three models. The dotted, yellow line represents the TCS for energies $E > 100$ eV. These TCSs are calculated using ELSEPA [SJP05]. The dashed, blue line represents the TCS for energies 0.02 eV $< E < 100$ eV. These TCS are adapted from experimental data from [Yoo+08] was used. The solid, red line represents the TCS for energies $E < 0.02$ eV. These are obtained by interpolation of the experimental data.

e^- - T_2 elastic scattering

In the low energy regime elastic scattering of electrons with molecular tritium is the dominant interaction and causes electrons to enter thermal equilibrium. At higher energies other interactions are more effective in cooling the electrons, but elastic scattering is still persistent (Figure 6.3).

The implemented TCS is concatenated from three different sources (Figure 6.4). In the high energy regime $E_{\text{lab}} > 100$ eV the TCS was calculated using the ELSEPA simulation code [SJP05]. For energies of 0.02 eV $< E_{\text{lab}} < 100$ eV experimental data from [Yoo+08] was used. In the low energy regime $E_{\text{lab}} < 0.02$ eV the TCS is obtained from extrapolation of the data from [Yoo+08]. Interpolating the data for energies $E_{\text{lab}} < 1$ eV (Figure A.2) yields the analytic expression

$$\sigma(E) = 1.21 \times 10^{-19} \text{ m}^2 \cdot \left(\frac{E}{\text{eV}} \right)^{0.125}. \quad (6.1)$$

The kinematic of an elastic scattering is determined by the two scattering angles φ and θ . For elastic scattering the polar angle φ is uniformly spread on $[0, 2\pi[$ and the azimuth angle θ is sampled from the corresponding DCS $\frac{d\sigma}{d\theta}$. For energies $E \geq 10$ eV the DCS were calculated using ELSEPA [SJP05]. For energies of $E < 10$ eV isotropic scattering is assumed. This is in good agreement with the simulation results at $O(10$ eV).

Setting `eT2_ELA = 0` deactivates e^- - T_2 elastic scattering and setting `eT2_ELA = 1` activates it. For further studies the sublyng DCS model can be varied. For `INT_ELA_DIR = 0` the DCS calculated by ELSEPA [SJP05] are used. For `INT_ELA_DIR = 1` isotropic scattering is assumed and for `INT_ELA_DIR = 2` the motion of direction is not affected by elastic scattering.

Electron impact ionization of T₂

Electron impact ionization is the dominant process populating the WGTS with ions and electrons and is very effective in cooling high energetic electrons.

For the TCS good analytical models are obtained from [JRS03]. This source resolves three ionization channels (Figure A.3). The ionization is dominated by the non dissociative ionization process with threshold energy of 15.42 eV:



The other two ionization channels lead to dissociation of the tritium molecule and create a tritium atom and an ion. These ionization channels have higher threshold energies of 18.15 eV and 30.6 eV.

Another model for the ionization TCS was implemented from [KR94]. This model does not resolve the ionization channels individually.

The ionization model used in the simulation is specified by the eT2_ION parameter. For eT2_ION = 1 the model from [JRS03] is used and for eT2_ION = 2 the model from [KR94]. For eT2_ION = 0 ionization is disabled.

The energy of the secondary electrons is sampled in both cases from the DCS from [KR94]. The direction of motion of primary and secondary electrons are sampled analogous to [GW78].

Electronic excitation of T₂ by e⁻

Electrical excitation levels of T₂ (H₂) are of $O(10 \text{ eV})$. Thus electrical excitation is an important cooling mechanism for electrons with energies of $O(100 \text{ eV})$.

The state of the tritium molecules prior to excitation is assumed to be in ground state, since the WGTS is at 30 K. Analytical models for TCSs have been implemented from [JRS03]. The source specifies three main categories of electric excitation from groundstate:

- Excitation to dipole allowed singlet state (Figure A.4).
- Excitation to dipole forbidden singlet states (Figure A.5).
- Excitation to triplet states (Figure A.6).

A total of 15 excitation channels have been implemented from [JRS03]. Additionally experimental TCSs for electric excitation from [Yoo+08] have been implemented in KARL.

The models from [JRS03] can be specified by setting eT2_EL parameter = 1 and the models from [Yoo+08] by setting eT2_EL parameter = 2. Setting eT2_EL parameter = 0 mutes the electric excitation.

During electric excitation it is assumed that no further energy is transferred from the electron to the tritium molecule. Thus electric excitation is implemented as a reduction of electron energy that does not change the electron's motion of direction.

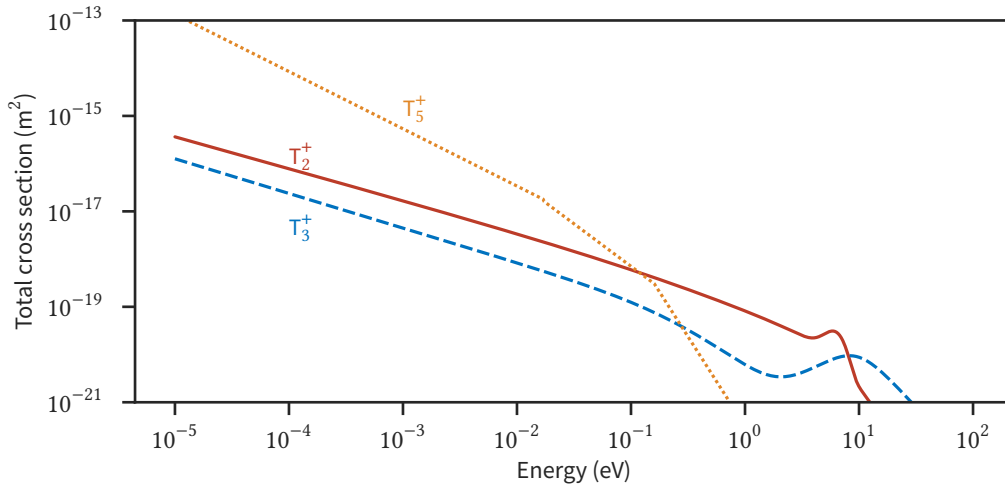


Figure 6.5.: TCSs for electron-ion recombination of different tritium ions. TCS for $e^- - T_2^+$ and $e^- - T_3^+$ recombination from [JRS03]. TCS for $e^- - T_5^+$ recombination from [Pet+15]. Energies defined in laboratory frame, where kinetic electrons interact with fixed T_2 molecules.

Rotational and vibrational excitation of T_2 by e^-

The adaption of H_2 data and models for rotational and vibrational excitation is rather ambitious due to different energies of rotation and vibration modes.

Nonetheless TCSs for rotational excitation from [Yoo+08] and vibrational TCSs from [Yoo+08] and [JRS03] are implemented in KARL. Analogous to electric excitation, rotational and vibrational excitation does not change the direction of the electron and solely reduces its energy.

Setting `eT2_ROT` parameter controls the rotational excitation. `eT2_ROT = 0` deactivates rotational excitation and for `eT2_ROT = 2` (sic!) the data from [Yoo+08] are used.

Vibrational excitation can be controlled by the `eT2_VIB` parameter. `eT2_VIB = 0` deactivates vibrational excitations. For `eT2_VIB = 1` model from [JRS03] is used. For `eT2_VIB = 2` the model from [Yoo+08].

6.3. Recombination of electrons with tritium ions

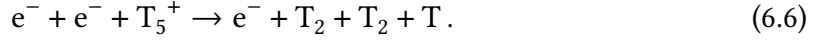
The density of tritium ions is by orders smaller than of molecular tritium. This leads to negligible number of interactions between electrons and ions. Only interactions that influence the simulation significantly are considered. Thus only recombination of electrons with ions are implemented as both species are removed from the simulation. Since both particles are removed only the TCS needs to be modeled.

Analogous to section 6.2, implemented models are adapted from H_2 and electrons are specified as bombarding particles in the laboratory frame definition.

Radiative recombination such as



is very unlikely ([BRM97]) and thus not implemented in the simulation. Also three-body recombination of T_2^+ , T_3^+ and T_5^+



is negligible. From [MS95] the rate coefficient for three body recombination at 30 K is approximates by

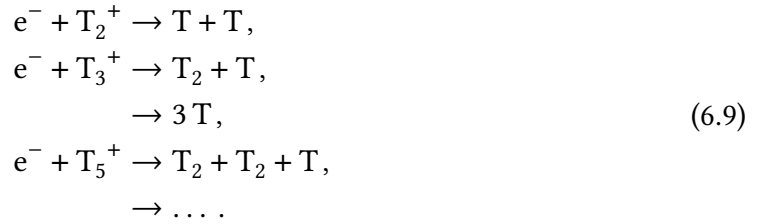
$$k_{3,\text{rec}} = 2 \times 10^{-45} \text{ m}^6 \text{ s}^{-1}. \quad (6.7)$$

Generously assuming (Figure 8.6) electron and ion densities of $n \approx 10^{15} \text{ m}^{-3}$ results in a MFP of

$$\lambda = \mathcal{O}(10^{10} \text{ m}). \quad (6.8)$$

Thus three-body recombination is negligible.

The dominant recombination channel in the WGTS is dissociative recombination of T_2^+ , T_3^+ and T_5^+ ions:



TCS for T_2^+ and T_3^+ are implemented using the analytic formulas from [JRS03] and TCS for T_5^+ recombination is implemented from [Pet+15]. An overview of the TCS is displayed in Figure 6.5. All TCSs raise towards small energies. Thus recombination becomes very dominant for slow electrons.

The recombination of electron with ions and vice versa can be controlled by the eT2_REC parameter. eT2_REC parameter = 0 deactivates the recombination and eT2_REC parameter = 1 activates it.

6.4. Interactions of tritium ions

The KARL simulation only simulates thermal ions and molecules (section 6.5). Thus only ion-molecule interactions that are relevant at 30 K are implemented. This will lead to large errors when higher temperatures are specified.

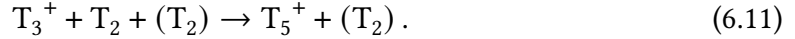
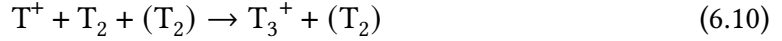
Elastic Scattering with T_2

Elastic scattering of tritium ions with T_2 is essential to keep thermal equilibrium. The TCS for T^+ , T_3^+ and T_5^+ are obtained from [TS00]. For T_5^+ - T_2 interactions the TCS of T_3^+ - T_2 was adapted. For T_2^+ the charge exchange TCS from [JRS03] was implemented. Since tritium ions and molecules are both implemented thermally (section 6.5), isotropic scattering was assumed for all ion-molecule elastic scattering processes.

Ion cluster formation

At low energies tritium ions can form larger ion clusters in combination with T_2 . In the simulation all ion clusters larger than T_5^+ are represented by T_5^+ (section 6.5). Thus only the formation up to T_5^+ must be implemented.

For T^+ and T_3^+ cluster formation is either radiative under radiation of a photon or in a ternary process in presence of a second tritium molecule possible:



Reaction rates for these processes are obtained from [Pla+12] and [GKP90]. For radiative cluster formation of T_5^+ a formation rate of $5 \times 10^{-23} \text{ m}^6 \text{ s}^{-1}$ was specified as in [GKP90]. The corresponding TCS are calculated from these reaction rates according to section 4.3.

For T_2^+ the process



was implemented from [JRS03].

Due to lack of models, the clusters are initialized with the velocities of the kinetic ion. This is sufficient as the thermal equilibrium with T_2 is reached quickly after formation.

6.5. Modeling of tritium ions

In the KARL code all tritium ions are assumed to be thermal. This assumption is made during the kinetic simulation and during interacting with tritium ions. For the implementation of energetic ions many further interaction processes need to be implemented and the current implemented models need to be modified. The implementation of models on larger energy range can be very challenging and adaption from hydrogen models rather ambitious.

The assumption of thermal ions is in first order fair, since in comparison to electrons, ions can only gain very little energy and are expected to cool down quickly. Further the impact of ions on the electron spectrum comes mainly from recombination processes, which is only possible at thermal energies.

Further the KARL code assumes that ion clusters larger than T_5^+ can be represented by T_5^+ . This assumption is in first order fair, since observations from [MG88; SJ97] show, that the recombination TCS for larger ion clusters barely differ for T_5^+ and larger clusters.

7. Analytical tests of the simulation

Quantitative experimental validation of the KARL code is only possible in the interplay with the PIC code (section 5.1). Since the PIC code is currently¹ still in development, no experimental tests can be performed. Yet the KARL code can be tested analytically. Therefore test cases with a analytical calculable outcome are designed. These tests have been performed for the most important processes that are implemented in KARL.

In section 7.1 the three implemented injection methods are tested. Elastic scattering is tested in section 7.2, ionization in section 7.3 and excitation in section 7.4.

The test of further processes is analytically hardly feasible, but a qualitative analysis is presented in chapter 8.

7.1. Test of the injection methods

The KARL code features three different injection methods. Depending on the INJECTION-parameter the initial electron energy is sampled from different distributions (section 5.4). The injection methods are tested by disabling all interactions. Thus it is expected, that immediately after creation the electrons propagate to the RW, where they can be observed unaltered. Hence successful injection tests do not only validate the sampling of the specified energy distributions, but also propagation in absence of interactions.

A corresponding test was performed for delta injection (INJECTION = 1) with energies of 1 meV, 1 eV and 1 keV. Delta injection initializes all electrons with exactly the specified energy. For each energy 10^4 injections have been performed. In all three test cases exactly 10^4 electrons with the specified energy² have been observed at the RW. Thus delta injection is properly implemented in the KARL code.

Analogously Maxwell Boltzmann injection (INJECTION = 2) was test at 1 meV, 1 eV, 1 keV with 10^5 injections each. In this context temperatures are specified by the energy-temperature relation $E = k_B T$. The observed and expected spectrum at the RW are displayed in Figure 7.1. All three tests show good results. Both the form and the normalization of the spectrum is in very good agreement with the expectation. Thus sampling Maxwell Boltzmann distributions is successfully validated.

The most important injection method for KARL is the β -injection (INJECTION = 0). Therefore a test with 10^5 injections was performed. The results are displayed in Figure 7.2. The expected and observed spectrum are in very good agreement. Thus the implemented β -spectrum (Equation 2.19) is validated.

¹as of December 2019

²Minor divergences can arise from the floating point of data types in C++

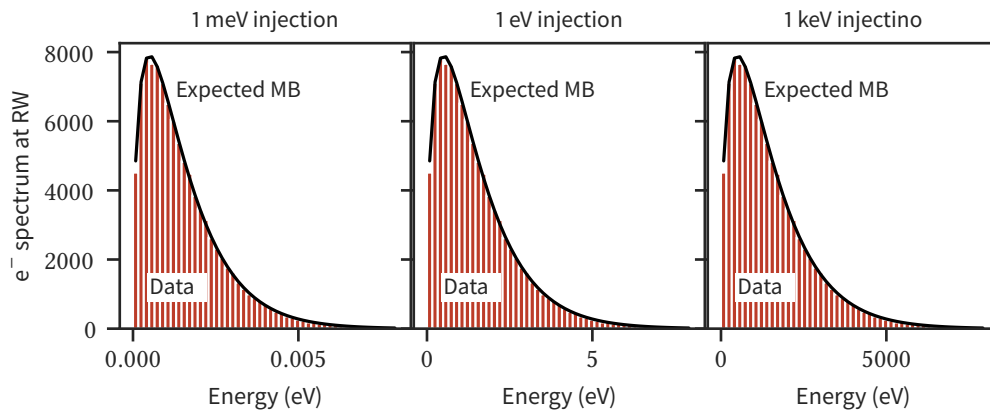


Figure 7.1.: Test of Maxwell Boltzmann Injection (INJECTION = 2) at three different energies: 1 meV (left), 1 eV (center), 1 keV (right), which are related to the temperature of the Maxwell Boltzmann distribution by $E = k_B T$. The red histograms show the observed electron energy spectrum at the RW. The solid, black lines shows the expected spectra.

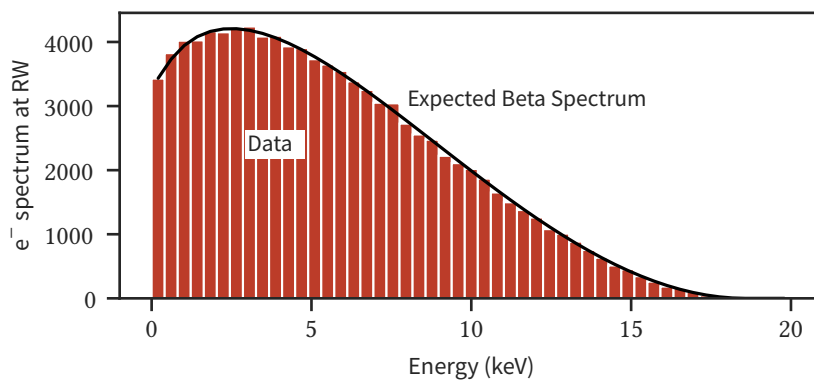


Figure 7.2.: Test of β -injection. The red histogram shows the observed energy spectrum at the RW. The solid, black line shows the expected β -spectrum (Equation 2.19).

7.2. Test of elastic scattering

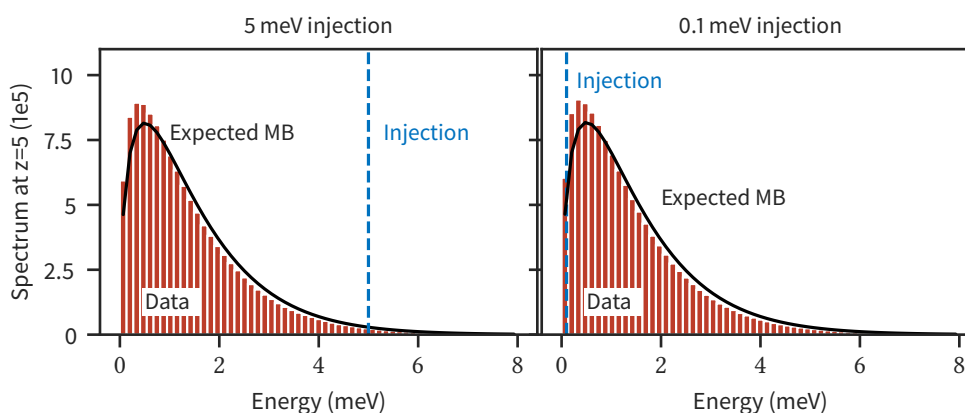


Figure 7.3.: Test of elastic scattering. Electrons are injected with constant energy of 5 meV (left) and 0.1 meV (right). The blue, dashed line represents the injection energy. After sufficient number of elastic scattering the electrons are expected to enter the 1 meV ($\cong 11.6$ K) Maxwell Boltzmann distribution of the underlying molecular tritium distribution. This expected spectrum is represented by the black, solid lines. These are normalized to the number of observed electrons. The red histograms represent the observed electron spectrum in the center of the WGTS.

In thermal region of energies $E = k_B \cdot 30 \text{ K} = 2.5 \text{ meV}$ elastic scattering is the dominant interaction. In this region elastic scattering is responsible for electrons to enter thermal equilibrium with the tritium molecules. For testing elastic scattering two tests have been performed.

In both test cases the sub lying molecular tritium distribution was initialized with a non-moving 1 meV ($\cong 11.6$ K) Maxwell Boltzmann distribution. It is expected that the electrons reach thermal equilibrium after a sufficient large number of interactions. To observe this effect electrons are initialized with constant energies (INJECTION = 1) of 5 meV and 0.1 meV.

Since electrons need a large number of interactions to reach thermal equilibrium a trade off between computation effort and statistics has to be made. To overcome this problem, the test case is designed to terminate the electrons after a fixed number of interactions. For better statistics the spectrum of electrons is observed in the center of the WGTS at $z = 5$.

The resulting spectra are displayed in Figure 7.3. The expected Maxwell Boltzmann distribution are normalized to the number of electrons observed. In first order observation and expectation are in good agreement. Minor divergences have been observed, indicating lower electron temperatures compared to the temperature of the molecular tritium. Since this effect arises in both tests, where the electrons have been initialization below and above the typical molecular tritium energy, it can not be caused by electrons that have not entered thermal equilibrium. The divergences arise from a known problem in the

integration over all possible momentum vector constellations of both interaction partners during MCS calculation. The problem also arises in the implementation of recombination and is discussed in detail in chapter 8 and chapter 9.

7.3. Test of ionization

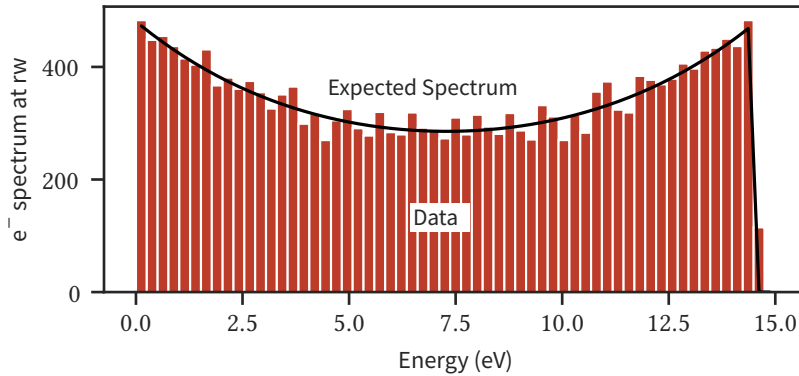


Figure 7.4.: Test of ionization. Electrons have been injected with constant energy of 30 eV. The expected energy spectrum is a superposition of secondary electron spectrum and altered primary spectrum. This expected spectrum is represented by the black, solid lines. The observed electron spectrum at the RW is displayed by the histograms in red.

Ionization processes between electrons and tritium molecules create the majority of charged particles in the WGTS. For testing the ionization all other interactions have been deactivated and the electrons are initialized with a constant energy. The energy was set to 30 eV, so that electrons can only perform one ionization process and hence the expected spectrum is easily analytically calculable. If all electrons perform an ionization the expected electron spectrum at the RW is a superposition of secondary electron spectrum and altered primary electron spectrum. The expected altered primary electron spectrum is derived from the expected secondary electron spectrum. This is unambiguous since the energy of primary electron after ionization calculates from energy of secondary electron and the binding energy.

In Figure 7.4 the results with 10^4 initialized electrons are displayed. The observed and expected spectrum are in good agreement in both shape and normalization. Thus ionization was successfully implemented in the KARL code.

7.4. Test of excitation

Excitation processes are very important for cooling electrons efficiently. In the KARL code excitation are implemented as constant energy loss. The energy corresponds exactly to the energy of the excited excitation level.

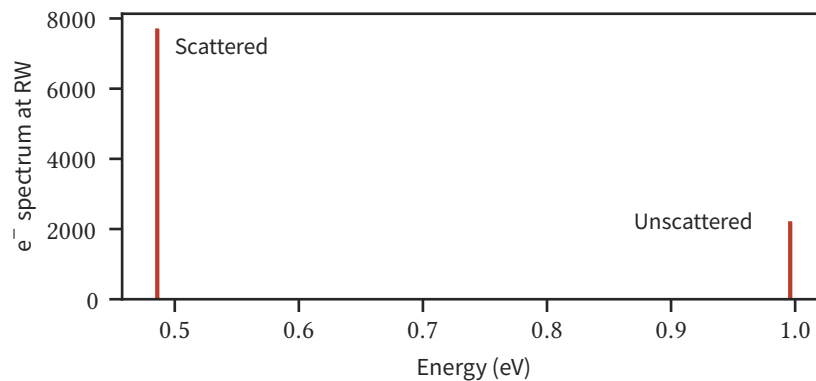


Figure 7.5.: Test of excitation. Electrons have been injected with constant energy of 1 eV. The expected energy spectrum consist of scattered electrons with energies of 0.484 eV and unscattered electron at 1 eV. The observed electron spectrum at the RW is displayed by the red histograms.

For testing excitation only the vibrational excitation of tritium³ from its ground state $\nu = 0$ to the first vibrational excitation level $\nu' = 1$ with an energy of 0.516 eV has been activated. All further interaction channels have been deactivated. In the test the electrons are injected with a constant energy of 1 eV. Thus an electron can perform exactly one excitation process. The results are displayed in Figure 7.5. The observed energy of scattered electrons is exactly at the expected position of 0.484 eV. Thus excitation processes are implemented successfully in KARL.

³adapted from H₂

8. Simulations with KARL

First simulations from the KARL code will be presented in this chapter. Since the PIC code (section 5.1) is still¹ under development, these first simulations are performed with the electric field set to zero. Thus these first results need to be treated with caution, as electric fields arising from charged particles are clearly a key component in the modeling of plasmas.

The final envisioned implementation of electron-ion recombination currently raises problems. Therefore the first simulation is performed without implementing recombination. Its results can be interpreted as conservative estimator, since additional recombinations decrease the particle densities. This first simulation without recombination is presented and analyzed in section 8.1.

In this first version of KARL, two preliminary implementations for recombination are featured. These show good results and will be presented in section 8.2.

Earlier works from [Nas+05] have also simulated the particle distribution in the WGTS of the KATRIN experiment. Although the previous work does not feature spatial resolution, the resulting electron spectrum can be compared to averaged results from KARL.

In addition, the influence of electric fields arising from the particle distributions is examined. Therefore the longitudinal electron flux from a previous plasma simulation from [Kuc16] is compared with the results from KARL. Both comparison are featured in section 8.3

The final plasma simulations at KATRIN can be validated using voltage-dependent RW currents generated by KARL. These currents are also experimentally measured and thus comparable with the simulation results. This validation method is introduced in section 8.4

8.1. First results using KARL

First results from the KARL code are obtained without electron-ion recombination. The lack of recombination lead to increased particle densities and thus increased plasma effects.

Accordingly a simulation was performed with 10^4 β -decays. For the proper initialization of the RDFs 5×10^3 additional β -decays were performed prior taking statistics (section 5.5). The corresponding parameter file is attached in Listing A.2. For better comprehensibility in the further context this simulation will be referenced as SIM1.

The simulation was performed on 200 cores and took ~ 2.2 h, equaling a wall time of $\sim 4.45 \times 10^2$ h. Hence the average simulation time for one β -decay and its subsequent reactions took ~ 100 s.

¹as of December 2019

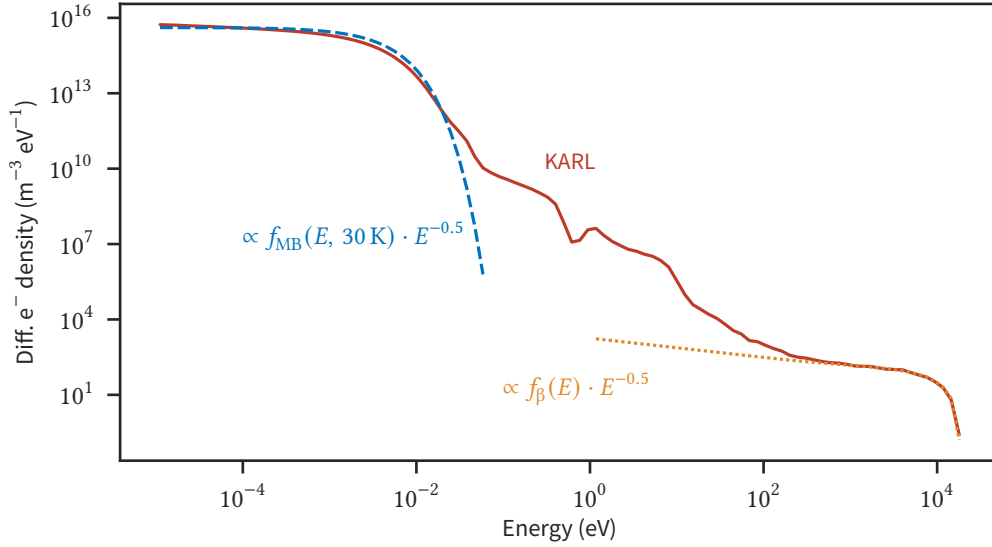


Figure 8.1.: Differential electron density spectrum averaged over the length of the WGTS. The solid, red line represent the results from SIM1. The dotted, yellow line follows Equation 8.1 and was fitted to the results from SIM1. The dashed, blue line follows Equation 8.2 and was also fitted to the results from SIM1.

Throughout the simulation a total of 2.1×10^5 secondary and higher order electrons were created. This equals ~ 14 secondary particles per initial β -electron. Thus the majority of electrons and ions are created by ionization.

Energy spectrum analysis A detailed analysis of the energy dependence of the electron spectrum from SIM 1 was performed by averaging over the length of the WGTS. The resulting differential electron density $\frac{dn}{dE}$ is displayed in Figure 8.1. The individual spectra at different longitudinal positions z are in first order identical in shape and only differ in the scale (Figure A.7). Thus this averaged spectrum act as substitute spectrum for the analysis.

The electron spectrum can be classified in three main regions. At high energies $E > 10^2$ eV the electron spectrum is expected to scale as

$$f_h(E) \propto f_\beta(E) \cdot E^{-0.5}, \quad (8.1)$$

where $f_\beta(E)$ is the β -spectrum (Equation 2.19). The high energetic electrons consists mainly of β -electrons, that approximately propagate unobstructed. Thus the non-directional flux scales with the β -spectrum. The additional factor $E^{-0.5}$ arises from the connection between non-directional particle flux and density. As shown in section 5.7 the density of a passing particle scales with the inverse of its longitudinal speed $\frac{1}{v_z}$ and thus with $E^{-0.5}$. This expected shape of the differential electron density for energies $E > 10^2$ eV is clearly reflected in the observed spectrum of SIM1.

At low energies $E < 10^{-2}$ eV the electrons are expected to enter thermal equilibrium with the molecular tritium. Hence the non-directional particle flux is expected to follow

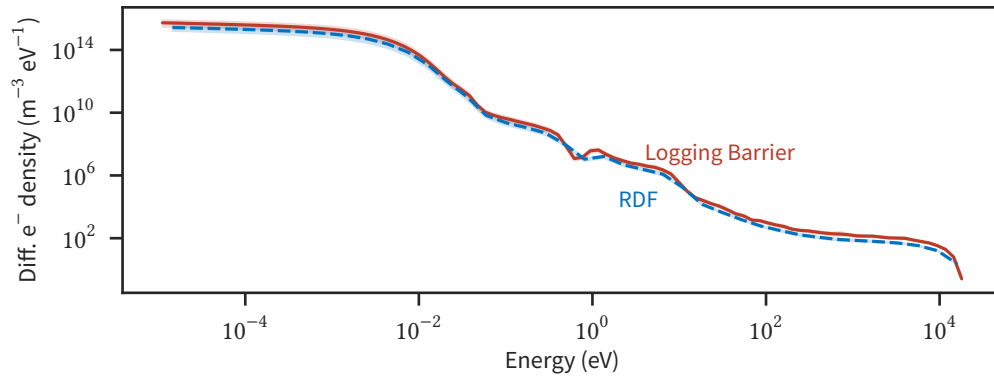


Figure 8.2.: Comparison of the differential electron density spectrum obtained from LBM with the spectrum of RDF at the end of the simulation. The solid, red line represents the results from the LBM. The dashed, blue line represents the final states of the RDF at the end of the simulation. Both spectra are average over the length of the WGTS. The corresponding standard deviation is indicated by the shaded area.

the 30 K Maxwell Boltzmann distribution $f_{\text{MB}}(E, 30 \text{ K})$ of the molecular tritium. Thus the differential electron density of low energies is expected to scale with

$$f_1 \propto f_{\text{MB}}(E, 30 \text{ K}) \cdot E^{-0.5}. \quad (8.2)$$

The observed spectrum fulfills the expectation well.

The intermediate energy regime consists of non-thermal secondary electrons, created by ionization processes. Subsequently these electrons have one or two orders of magnitude smaller MFP than β -electrons (Figure 6.3). Thus they can not propagate unobstructed through the WGTS, but cool down to thermal energies via numerous interactions.

Comparison of LBM and RDF Besides the standard LBM (section 5.7) for output, also the RDF (section 5.5) at the end of the simulation can be used to obtain differential electron distributions. Comparison of both spectra is a good validation of the results. Both spectra are displayed in Figure 8.2. As one can see both methods are in good agreement. This shows the consistency of both methods and is a good indicator for the quality of the algorithm. Minor divergences arise from the difference in calculation method. The RDFs focus on high spatial resolution, whereas the LBM on high energy resolution.

Longitudinal analysis of e^- -spectrum In addition to energy resolved spectra, the KARL code also yields spatially resolved spectra. An overview of the differential electron density spectrum $\frac{dn}{dE}$ with energetic and spatial resolution is displayed in Figure 8.3. It is visible that all secondary electrons show a strong longitudinal dependency, whereas at high energies $E > 10^2 \text{ eV}$ no longitudinal dependency is observable. In this context secondary electrons, refers to all non β -electrons.

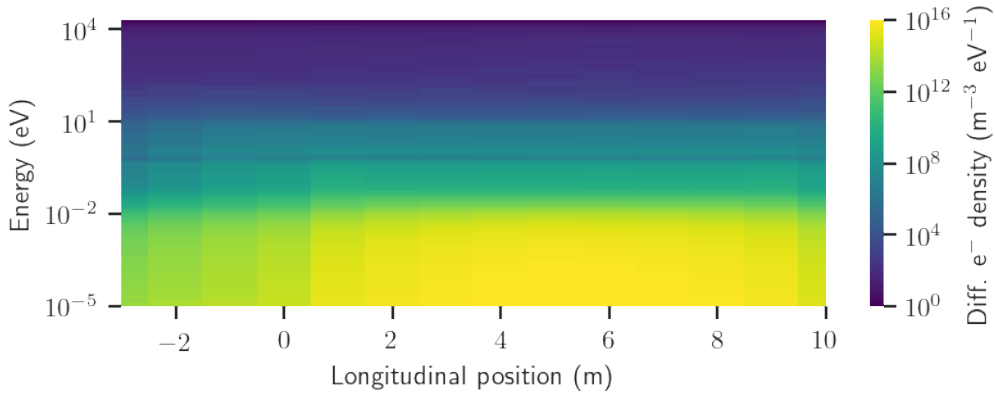


Figure 8.3.: Differential electron densities from SIM1. The differential density is indicated by the color. Small densities are indicated by blue coloring. Towards higher densities the hue shifts to yellow. The x -axis represent longitudinal position in the WGTS. y -axis represents the electron energy on a logarithmic scale.

On the assumption that the high energetic electrons are dominated by β -electrons and that these β -electrons pass the WGTS unobstructed, the non-directional β -electrons flux at a given longitudinal position z_{ref} is composed of three factors:

1. N_1 β -electrons emerging from $z < z_{\text{ref}}$ with $v_z > 0$, before reflection at the spectrometers.
2. N_2 β -electrons emerging from $z > z_{\text{ref}}$ with $v_z < 0$.
3. N_3 β -electrons after reflection at the spectrometers with $v_z < 0$.

z and v_z are the longitudinal position and velocity of the electrons in the respective categories. In the KARL code the β -electrons are injected isotropic. Thus half the β -electrons emerge with negative v_z and the other half with positive v_z . For N_β β -decays this yields to $N_1 + N_2 = \frac{N_\beta}{2}$ and $N_3 = \frac{N_\beta}{2}$. Hence the non directional flux $N_1 + N_2 + N_3$ is expected to equal N_β .

A more precise analysis shows a small longitudinal dependency of high energetic electrons in the order of $\mathcal{O}(0.1 \cdot N_\beta)$ (Figure 8.4). This small longitudinal dependency is in good agreement with the previous approximation and in first order no longitudinal dependency is observable at high energies.

At lower energies $E < 10^2$ eV the spectrum is made up of secondary electrons created by ionization. These subsequently cool down quickly to thermal energies. The probability for ionization scales with the T_2 -density. Thus the low energy electron spectrum is expected to scale with the T_2 -density. This dependency is clearly observable for the secondary electron spectrum. A more precise visualization of this dependency is displayed in Figure 8.5.

Further one can see that the electron densities are quantitatively dominated by thermal electrons. Non-thermal secondary electrons are also persistent, but the density is by orders of magnitude smaller.

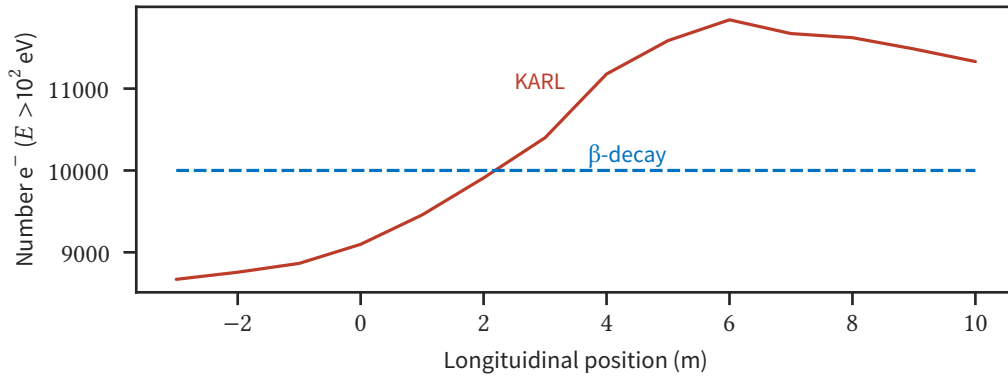


Figure 8.4.: Analysis of the high energetic β -electrons from SIM1. The solid, red line shows the number of e^- with energies $E > 10^2$ eV observed in the simulation. The dashed, blue line shows the expectation for unobstructed β -electrons of $N_\beta = 10^4$. Cutting the β -spectrum at 10^2 eV equals 99.1 % of the β -spectrum. The divergence of the simulation data to the expectation for unobstructed β -electrons is $O(1000) \hat{=} O(0.1)$.

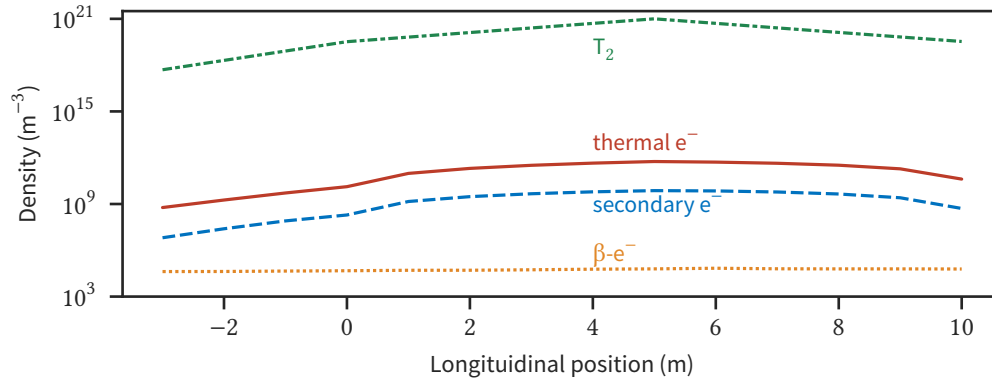


Figure 8.5.: Comparison of densities of electron from different energy regimes from SIM1. The solid, red line represents the thermal electrons with energies $E < 10^{-2}$ eV. The dashed, blue line represents the non-thermal secondary electrons with energies 10^{-2} eV $< E < 10^2$ eV. The dotted, yellow line represents the β -electrons with energies $E > 10^2$ eV. The dash-dotted, green line represents the density of molecular tritium.

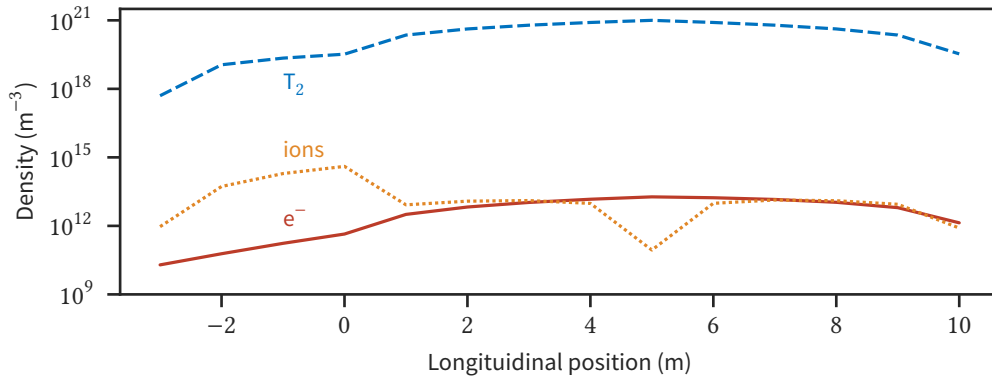


Figure 8.6.: Particle densities from SIM1. The solid, red line represents the electron density. The dashed, blue line represents the density of molecular tritium. The dotted, yellow line represents the density of tritium ions.

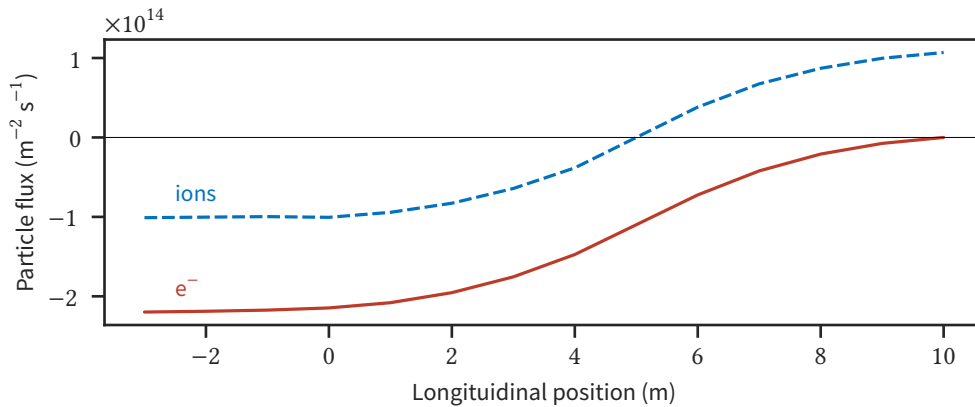


Figure 8.7.: Particle fluxes from SIM1. The solid, red line represents the particle flux of electrons. The dashed, blue line represents the ion flux. Positive fluxes indicates particles moving towards the spectrometers.

ions Another important output of the KARL code are ion distributions and fluxes. An overview of electron, ion and T_2 densities over the length of the WGTS is displayed in Figure 8.7. One can clearly see, that the ions do not follow the molecular tritium distribution. The ions show a clear minimum in the center of the WGTS and a maximum in the regime $-3 < z < 0$. In contrast to the electrons, the tritium ions follow the molecular tritium velocity profile, which shows an outward movement from the center at $z = 5$ towards the TMPs at $z = 0$ and $z = 10$. At $-3 < z < 0$ a non-moving molecular tritium background was implemented, which leads to high ion density in this area. This implementation is based on lack of data and is clearly in need of improvement.

The particle fluxes from SIM1 are displayed in Figure 8.7. The ion flux clearly reflects the T_2 velocity profile (section 6.1). Electrons can only leave the WGTS at the RW. Hence the electron-flux is expected to be monotonic rising and negative at all points. This expectation is clearly visible in the results. A brief quantitative analysis of the particle fluxes shows

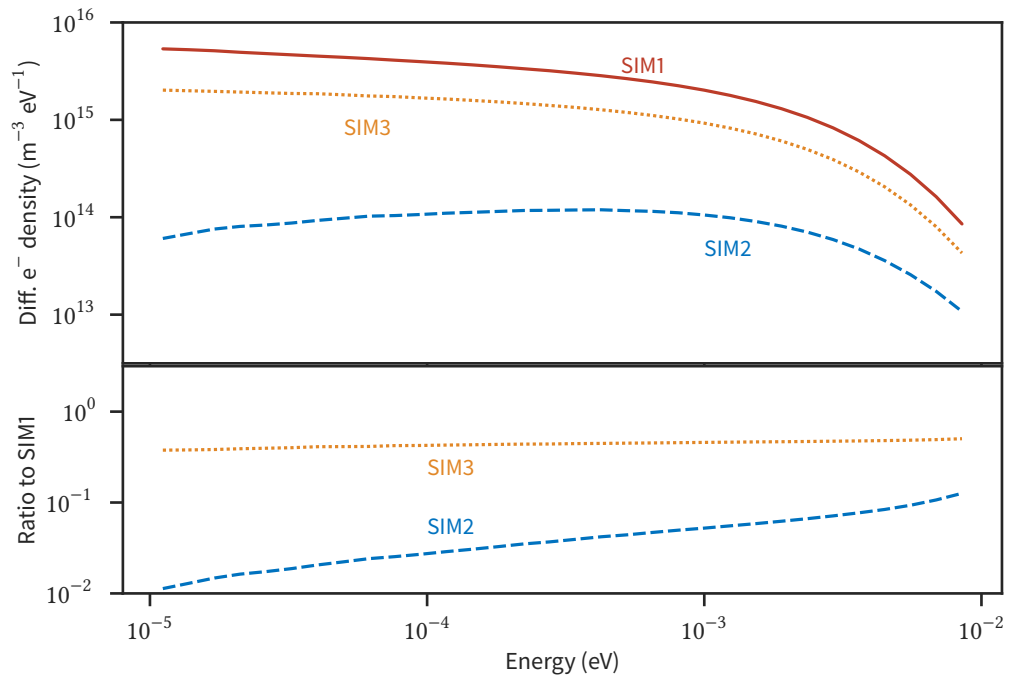


Figure 8.8.: Comparison of SIM1, SIM2 and SIM3 from KARL in the thermal region. The upper half of the plot shows the differential densities. The displayed densities are averaged over the whole length of the WGTS. The bottom half of the plot shows the ratio of the densities from SIM2 and SIM3 in respect to SIM1. SIM1: Conservative estimator without recombination, displayed as solid, red line. SIM2: Implementation of asymmetric recombination, displayed as dashed, blue line. SIM3: Implementation of recombination by solely accounting electron energy in the MCS calculation, displayed as dotted, yellow line.

that the number of electrons leaving the WGTS equals the number of ions. Thus no charge up of the WGTS was observed.

8.2. Simulations with recombination

Recombination has been implemented as described in chapter 5. First examinations show asymmetric recombination rates for electrons and tritium ions. Thus indicating nonphysical behavior. This problem arises at low energies during the MCS calculation. During this calculation an integration over all possible momentum constellations between initial particle and interaction partner, which is indicated by the RDF, is performed. As in this version all RDFs are implemented isotropic, which leads to absurdly large MCS for tritium ions and thus removing all tritium ions from the simulation. Envisioned fixes for this problem have been identified and will be discussed in chapter 9.

At this moment two implementation of recombination exist in the KARL code. Accordingly the two simulation SIM2 and SIM3 with 10^4 β -decays each have been performed.

In SIM2 the recombination was implemented asymmetrically. Only for the physical simulation of electrons, recombination has been implemented. To properly account for the recombination on ion side, the densities of the ion RDFs are accordingly reduced. During simulation of ions no recombination effects are followed and thus the results for ions are faulty. The corrected ion densities are only reflected by the ion RDFs.

In SIM3 the recombination was implemented symmetrically, but the integration over possible constellation of momentum vectors during the MCS calculation was completely neglected. The laboratory frame energy in the MCS calculation was calculated solely from the electron energy, thus completely ignoring ion energy. This assumption was implemented symmetrically during kinetic simulation of electrons and ions.

Comparing SIM1 with SIM2 and SIM3 shows, that for energies $E > 10^{-2}$ eV all three simulations yield identical results (Figure A.8). Thus only at low energies $E < 10^{-2}$ eV recombination is significant. A comparison in this energy regime is displayed in Figure 8.8.

The comparison shows that recombination reduces the electron densities. Compared to SIM1, the electron densities in SIM2 are reduced by a factor of $\mathcal{O}(10^{-2})$ and in SIM3 by a factor of ~ 0.4 . The stronger reduction of SIM2 compared to SIM3 indicates a strong influence of proper integration in the MCS calculation. Further SIM2 shows a slope in the reduction towards smaller energies, whereas the ratio between SIM3 and SIM1 is in first order a constant. From the TCS for electron-ion recombination (Figure 6.5) a higher recombination rate towards smaller energies is expected, thus favoring SIM2.

8.3. Comparing KARL with previous simulations

Comparison of differential electron spectrum The electron spectrum in the WGTS has also been simulated in a previous work from [Nas+05]. This work will be referenced as COMP1 in the further context. In comparison to KARL the previous work does not resolve the particle densities spatially and does not cover ions kinetically. Thus comparison with COMP1 was performed by averaging the results from KARL over the whole length of the WGTS.

A comparison of the differential electron density spectrum from SIM1 and COMP1 is displayed in Figure 8.9. The spectrum from SIM1 acts substitutional for SIM2 and SIM3 at energies $E > 10^{-2}$ eV, since all three spectra are identical in this energy regime (Figure A.8). At lower energies a more precise comparison will be featured in the further discussion.

For the comparison between SIM1 and COMP1, the spectrum from COMP1 was normalized to the spectrum from SIM1 using the β -spectrum at high energies of $E > 10^3$ keV. At energies from $\mathcal{O}(10$ keV) down to $\mathcal{O}(1$ eV) both simulation are in good agreement. Noticeably is the peak in the spectrum of COMP1 at $\sim 10^1$ eV, which is not present in KARL. However in both simulations a kink in the spectrum is visible at this point and the slopes from both simulations are in good agreement. The kink can be related to a corresponding kink in the TCS of electron T_2 interactions (Figure 6.3). At an energy of $E \approx 1$ eV the result from KARL show a local minimum. This minimum is not reflected in the results from COMP1. Further down to energies of $E \approx 10^{-2}$ eV both spectra show minor divergences but are in first order in good agreement.

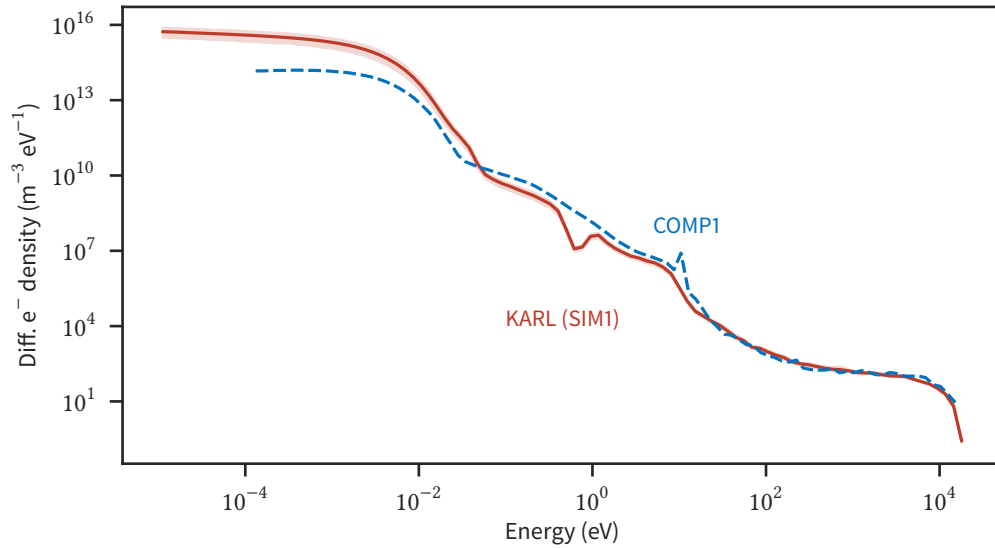


Figure 8.9.: Comparison of differential electron densities from SIM1 with results of COMP1 [Nas+05]. The results from KARL are averaged over the WGTS and displayed as solid, red line. The shaded area represents standard deviation of the longitudinal averaging. The dashed blue line shows results from COMP1. The spectrum of COMP1 was normalized using the β -spectrum at energies $E > 10^2$ eV.

Towards lower energies the spectra differ and recombination effects become dominant. A precise comparison of COMP1 with SIM2 and SIM3 at energies $E < 10^{-2}$ eV is displayed in Figure 8.10. One can see, that COMP1 and SIM2 are in very good agreement. The results from COMP1 are within one standard deviation of SIM2. The displayed standard deviation arises from averaging the spectra over the length of the WGTS. SIM3 shows larger divergence to COMP1, both in scale and shape. This indicates, that recombination was implemented better in SIM2 than in SIM3 and that proper integration is essential for MCS calculation.

Comparison of longitudinal electron density Electric fields arising from the particle distributions have not been implemented in the simulations with KARL so far. To estimate the errors arising from missing electric fields, a comparison with previous plasma simulations (section 3.4) from [Kuc16] will be featured. This simulation will be refereed as COMP2 in the further context. In Figure 8.11 the longitudinal electron density distributions from SIM2 and COMP2 are displayed. SIM2 was chosen among the three simulation from KARL, since its electron distribution properly reflects recombination effects.

The comparison shows that the shape of both simulations drastically differ. The results from KARL show a clear maximum in the center of the WGTS, whereas the results from COMP2 show a local minimum. This minimum was also observed in the ion distributions from simulations with KARL (Figure 8.6). Hence the electrons from COMP2 are likely attracted by the ions and therefor adapt their distribution. This effect can not be resolved by the KARL simulation alone, but only in interplay with the PIC simulation. This dras-

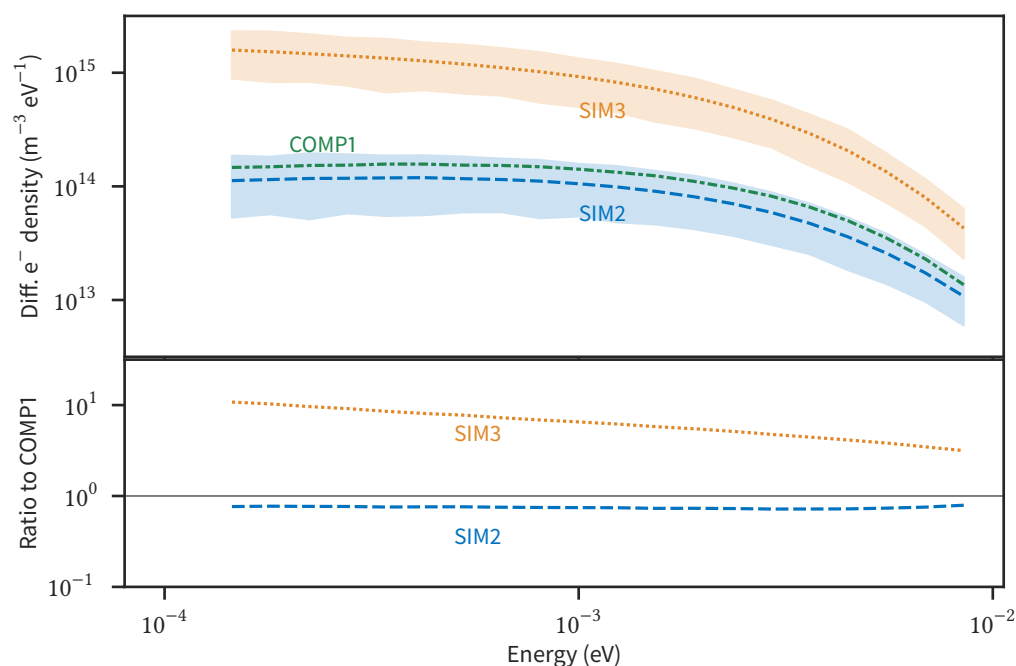


Figure 8.10.: Comparison of SIM2 and SIM3 with results from COMP1 [Nas+05] in the thermal region. The upper half of the plot shows the differential densities. The displayed densities from SIM2 and SIM3 are averaged over the whole length of the WGTS. The shaded area represent the stand deviation from this averaging. The bottom half of the plot shows the ratio of the densities from SIM2 and SIM3 in respect to COMP1. SIM2: Implementation of asymmetric recombination, displayed as dashed, blue line. SIM3: Implementation of recombination by solely accounting electron energy in the MCS calculation, displayed as dotted, yellow line. COMP1: Results from [Nas+05], displayed as dash-dotted, green line.

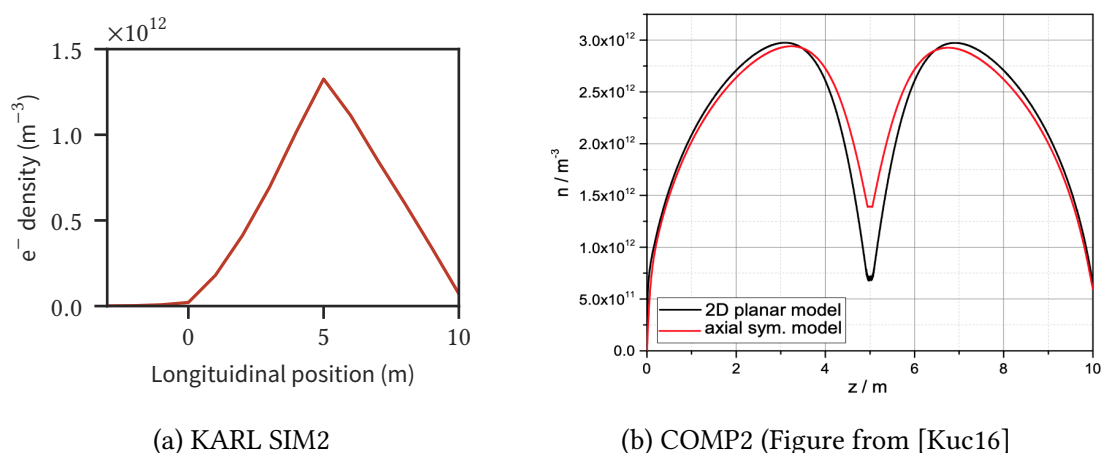


Figure 8.11.: Comparison of the longitudinal electron density distribution from, (a) SIM2: results from KARL, (b) COMP2: results from the plasma simulation of [Kuc16].

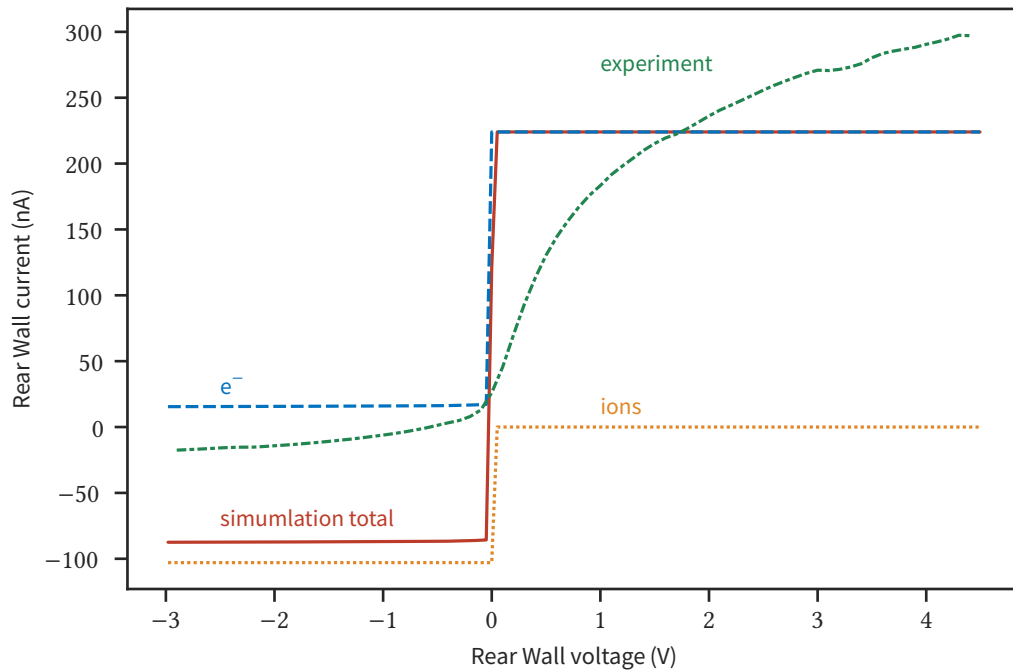


Figure 8.12.: Comparison of simulated voltage-dependent Rear Wall currents with experimental observations. The solid, red line represents the total Rear Wall current from simulation. The total consists of electron contribution (represented by dashed, blue line) and ion contribution (represented by dotted, yellow line). The observed currents from the experiment are represented by the dash-dotted green line. The measurement was made before KNM2 on the 20.09.2019 with a column density of 84 % at a temperature of 30 K.

tic divergence shows the need of proper implementation of electric fields in the KARL simulation.

Further a quantitative analysis of the densities show, that the electron densities in the center of the WGTS are both $\sim 1.25 \text{ m}^{-3}$. Since this is a maximum for SIM2 and a local minimum for COMP2, the total densities over the whole WGTS significantly differ. COMP2 shows much larger densities than SIM2. This can not be justified by missing electric fields, but is caused by either missing decay or creation channels.

All in all the comparison shows drastic divergences between SIM2 and COMP2 and reflects the need of implementing electric fields in the KARL simulation. A more precise comparison will be possible, once the development of the entire plasma simulation with KARL and the PIC simulation is completed.

8.4. Validation via voltage-dependent Rear Wall currents

Within the KATRIN experiment voltage-dependent RW current measurements have been performed. Therefore the RW voltage is swept from -3 V to 4 V and vice versa, while measuring the electric current at the RW.

In first order the RW voltage can be considered as electrostatic filter. Hence at negative voltages all positive ions and electrons with sufficient energy reach the RW. In the negative limit the entire current consists of ions and in the positive limit of electrons. Thus the experimental observation yields important quantitative information on the particle fluxes.

Further this electrostatic filtering can be simulated by the KARL code by analyzing the LBM at the RW. In the post processing all particles surpassing the retarding voltage can be accumulated and calculated to an electric current. By sweeping through different retarding voltages analogous voltage-dependent RW currents are obtained.

In Figure 8.12 results from SIM1 and experimental observations² are displayed. This comparison is more of demonstrative nature and quantitative analysis should only be performed under caution since several important factors have not been considered in this simulation.

One can clearly see that the experimental RW currents are larger in both limits and have a broader shape. Generally broader shapes indicate higher temperatures, since the particles have larger energies and thus can reach the RW at higher retarding voltages. This shows that the observed RW currents can not be formed solely by the 30 K Maxwell Boltzmann distributions from the simulation but further mechanisms need to be implemented. For this simulation this divergence is acceptable, since neither electric fields arising from particles, nor the interaction of the RW voltage with the particles in the KARL simulation are considered in this simulation. Proper modeling will only be possible by interplay of the KARL simulation and the PIC simulation. For the final validation multiple simulations have to be performed at different RW voltages using both simulations.

Further the higher experimental RW current in the positive limit raises questions. SIM1 is performed without recombination and the column density in the simulation is higher than in the experimental setting. Both factors favor higher simulational currents, but the opposite is observed. This indicates missing mechanism in the simulation. GEANT4 [Ago+03] simulations from [För17] have shown non negligible reflection coefficient for high energetic electrons at the RW. The average propagation length of an unreflected β -electron equals the length of the WGTS. Thus a reflected β -electron additionally propagates twice the average length. A reflection coefficient of 50 % already doubles the β -electron flux and therefore the ionization probability and hence the RW currents in the positive limit.

This shows how powerful the experimental validations via voltage-dependent RW currents are, since already at this point without proper modeling of physics, essential implementations for the KARL code have been identified. And once the entire plasma simulation is completed, the voltage-dependent RW currents allow for experimentally validation of the plasma simulations.

²The measurement was made before KNM2 on the 20.09.2019 with a column density of 84 % at a temperature of 30 K

9. Summary and outlook

The KATRIN experiment aims on measuring the mass of the electron neutrino with a unprecedented sensitivity of 0.2 eV. To limit the systematic uncertainty caused by plasma effects in the WGTS of the KATRIN experiment, a twofold plasma simulations strategy was designed. One constituent of this simulation strategy is the KARL code. The KARL code was developed within in this master thesis and simulates the electron and ion distribution in the WGTS within a constant electric field configuration.

The KARL code uses a semi classical Monte Carlo approach to iteratively simulate particles kinetically in the WGTS. Starting point of the kinetic simulation are β -decays creating energetic β -electrons. During the simulation of these β -electrons new particles arise from processes such as ionization. All arising particles are appended to a particle queue and simulated consecutively using the same algorithm. Hence particles arising from secondary and higher order particles are consistently included in the simulation. Particle species included in the current version of KARL are electrons and the tritium ions T^+ , T_2^+ , T_3^+ , T_5^+ . Further species can be easily added in future versions.

The kinetic simulation is performed using an alternating algorithm, where particles are propagated by one mean free path and afterwards perform an interaction. Therefore self consistent Runtime Density Fields (RDFs) have been implemented to properly calculate the interaction probabilities between two particles, that are both simulated within KARL. For the output the Logging Barrier Method (LBM) has been developed.

The focus of the KARL simulation is on particle interactions. Thus proper modeling of interactions is essential.. Therefore the most recent models for all relevant interaction have been implemented. These are e^- - T_2 elastic scattering, e^- impact ionization of T_2 , e^- impact excitation of rotational, vibrational and electrical modes of T_2 , e^- -ion recombination, ion- T_2 elastic scattering and ion- T_2 cluster formation.

In the scope of this thesis the KARL code has been successfully developed. It is implemented in C++, shows good performance and is highly parallelized. The KARL code shows very good results in first analytic test cases and a comparison with previous results from [Nas+05] are in great agreement. Further the KARL code can simulate voltage-dependent RW currents, that allow for experimental validation of the entire plasma simulation. An experimental validation has not yet been performed and will only be possible once the entire plasma simulation has been completed.

Minor problems have been observed in the ion-electron recombination. These arise from the implementation of the RDFs. Currently the ion RDFs are assumed to be thermal and isotropic. The electron RDFs feature energy resolution, but are also assumed to be isotropic. During the calculation of the MCS the integration over possible momentum constellations of initial particle and RDF yields too large results. This is caused by the current implementation of the RDFs. For fixing this problem, the RDFs need to be implemented with energetic and directional resolution.

Nonetheless the current results are in very good agreement with the previous results and only minor variations from the current results are expected. The current version of KARL covers all important effects. Further possible implementations have been identified, but are not expected to have a dominant influence on the simulation. A list of noteworthy envisioned implementations for future versions of KARL will be presented in the following:

- Simulation from [För17] have shown a non negligible reflection coefficient for electrons hitting the RW. More precise simulations or experimental observations should be performed and accordingly implemented into KARL.
- Currently in the region between RW $z = -3$ and the first pump ports: $z = 0$, the velocity profile for molecular tritium is expected to be at rest. In first order this assumption is fair, but a more precise simulation of the setting in the region should be performed and implemented to KARL.
- The current version of KARL only covers thermal ions. Adaption of the models towards higher energies and implementation of non thermal ions is recommended for future version of KARL.
- The majority of theoretical and experimental models for particle interaction have been adapted from models for hydrogen. If available in the future models for tritium should be preferred.

In summary, the KARL code was successfully developed and shows good efficiency. Possible updates have been identified and summarized. First analytic test cases have been successful and first results are in very good agreement with previous simulations from [Nas+05]. In addition to the previous simulation, the KARL code provides spatial resolution, covers ions kinetically and allows for easy adaptations in the further development. This spatial resolution also allows for experimental validation of the entire plasma simulation at KATRIN via voltage-dependent RW current measurements.

Bibliography

- [Abg+14] N. Abgrall et al. “The Majorana Demonstrator Neutrinoless Double-Beta Decay Experiment”. In: *Adv. High Energy Phys.* 2014 (2014), p. 365432.
- [Ago+03] S. Agostinelli et al. “Geant4—a simulation toolkit”. In: *Nuclear Instruments and Methods in Physics Research Section A: Accelerators, Spectrometers, Detectors and Associated Equipment* 506.3 (2003), pp. 250–303.
- [Ahm+01] Q. R. Ahmad et al. “Measurement of the Rate of $\nu_e + d \rightarrow p + p + e^-$ Interactions Produced by ^8B Solar Neutrinos at the Sudbury Neutrino Observatory”. In: *Phys. Rev. Lett.* 87 (7 July 2001), p. 071301.
- [Ake+19] M. Aker et al. “Improved Upper Limit on the Neutrino Mass from a Direct Kinematic Method by KATRIN”. In: *Phys. Rev. Lett.* 123 (22 Nov. 2019), p. 221802.
- [Ams+15] J. F. Amsbaugh et al. “Focal-plane detector system for the KATRIN experiment”. In: *Nucl. Instrum. Meth.* A778 (2015), pp. 40–60.
- [Ase+11] V. N. Aseev et al. “An upper limit on electron antineutrino mass from Troitsk experiment”. In: *Phys. Rev.* D84 (2011), p. 112003.
- [Aug+12] M. Auger et al. “Search for Neutrinoless Double-Beta Decay in ^{136}Xe with EXO-200”. In: *Phys. Rev. Lett.* 109 (3 July 2012), p. 032505.
- [Bec+14] M. Beck et al. “An angular-selective electron source for the KATRIN experiment”. In: *JINST* 9.11 (2014), P11020.
- [Bla15] H. J. de Blank. “Guding center motion”. In: vol. 298. *Schriften des Forschungszentrums Jülich Reihe Energie & Umwelt / Energy & Environment*. 12th Carolus Magnus Summer School on Plasma and Fusion Energy Physics, Leuven (Belgium), 24 Aug 2015 - 4 Sep 2015. Jülich: Forschungszentrum Jülich GmbH Zentralbibliothek, Verlag, Aug. 24, 2015, pp. 60–65.
- [BMH11] O. v. Baeyer, L. Meitner, and O. Hahn. “Magnetische Spektren der Beta-Strahlen des Radiums”. In: *Physikalische Zeitschrift* 12 (1911), pp. 1099–1103.
- [Bor70] J. P. Boris. “Relativistic plasma simulation-optimization of a hybrid code”. In: *Proceeding of Fourth Conference on Numerical Simulations of Plasmas* (Nov. 1970).
- [BRM97] Sujata Bhattacharyya, A. Roy, and Siddhartha Mitra. “Radiative recombination of cold electron with proton and deuteron”. In: *Fizika A* (Jan. 1997).
- [Cha14] Chadwick. “Intensitätsverteilung im magnetischen Spektrum der Betastrahlen von Radium B+C”. In: *Verhandlungen der Deutschen Physikalischen Gesellschaft* 16 (1914), pp. 383–391.

- [Coc16] F. Coccetti. “The Fermiac or Fermi’s Trolley”. In: *Nuovo Cimento C Geophysics Space Physics C* 39.2, 296 (Mar. 2016), p. 296.
- [Com17] Wikimedia Commons. *File:Fermiac.jpg — Wikimedia Commons, the free media repository*. [Online; accessed 29-November-2019]. 2017. URL: <https://commons.wikimedia.org/w/index.php?title=File:Fermiac.jpg&oldid=228537769>.
- [Cow+56] C. L. Cowan et al. “Detection of the Free Neutrino: a Confirmation”. In: *Science* 124.3212 (1956), pp. 103–104.
- [Dan+62] G. Danby et al. “Observation of High-Energy Neutrino Reactions and the Existence of Two Kinds of Neutrinos”. In: *Phys. Rev. Lett.* 9 (1 July 1962), pp. 36–44.
- [Fer34] E. Fermi. “Versuch einer Theorie der beta-Strahlen. I”. In: *Zeitschrift für Physik* 88.3-4 (Mar. 1934), pp. 161–177.
- [För17] Ellen Förstner. *Optimization of the KATRIN rear wall for a keV-scale sterile neutrino search*. BA thesis. 2017.
- [Frä10] Florian M. Fränkle. “Background Investigations of the KATRIN Pre-Spectrometer”. PhD thesis. 2010.
- [Fri+19] F. Friedel et al. “Time-dependent simulation of the flow reduction of D₂ and T₂ in the KATRIN experiment”. In: *Vacuum* 159 (2019), pp. 161–172.
- [Fuk+98] Y. Fukuda et al. “Evidence for Oscillation of Atmospheric Neutrinos”. In: *Physical Review Letters* 81.8 (Aug. 1998), pp. 1562–1567.
- [Gab+04] Edgar Gabriel et al. “Open MPI: Goals, Concept, and Design of a Next Generation MPI Implementation”. In: *Proceedings, 11th European PVM/MPI Users’ Group Meeting*. Budapest, Hungary, Sept. 2004, pp. 97–104.
- [GER+18] GERDA Collaboration et al. “Upgrade for Phase II of the Gerda experiment”. In: *The European Physical Journal C* 78.5 (May 2018), p. 388.
- [GGS99] Mary K. Gaillard, Paul D. Grannis, and Frank J. Sciulli. “The standard model of particle physics”. In: *Reviews of Modern Physics* 71.2 (Mar. 1999), S96–S111.
- [Gil+10] W. Gil et al. “The Cryogenic Pumping Section of the KATRIN Experiment”. In: *IEEE Transactions on Applied Superconductivity* 20.3 (June 2010), pp. 316–319.
- [GKP90] D. Gerlich, G. Kaefer, and W. Paul. “Ion trap studies of ternary and radiative ass. processes.” In: *Symposium on Atomic and Surface Physics*. T.D. Märk and F.Howorka, 1990.
- [Glü+13] Ferenc Glück et al. “Electromagnetic design of the large-volume air coil system of the KATRIN experiment”. In: *New Journal of Physics* 15.8 (Aug. 2013), p. 083025.
- [GP12] Andrea Giuliani and Alfredo Poves. “Neutrinoless Double-Beta Decay”. In: *Advances in High Energy Physics* 2012 (2012), p. 38.
- [GW78] B. Grosswendt and E. Waibel. “Transport of low energy electrons in nitrogen and air”. In: *Nuclear Instruments and Methods* 155.1 (1978), pp. 145–156.

-
- [Ha17] Florian Heizmann and Hendrik Seitz-Moskaliuk and. “The Windowless Gaseous Tritium Source (WGTS) of the KATRIN experiment”. In: *Journal of Physics: Conference Series* 888 (Sept. 2017), p. 012071.
- [Hac15] M. Hackenjos. “Die differentielle Pumpstrecke des KATRIN-Experiments - Inbetriebnahme und Charakterisierung des supraleitenden Magnetsystems”. MA thesis. Fakultät für Physik des Karlsruher Instituts für Technologie, 2015.
- [Hag15] Alireza Haghghat. *Monte Carlo methods for particle transport*. CRC Press Taylor & Francis Group, 2015. ISBN: 9781466592537.
- [Hig64] Peter W. Higgs. “Broken Symmetries and the Masses of Gauge Bosons”. In: *Phys. Rev. Lett.* 13 (16 Oct. 1964), pp. 508–509.
- [JRS03] R.K. Janev, D. Reiter, and U. Samm. *Collision processes in low-temperature hydrogen plasmas*. Tech. rep. Forschungszentrum Juelich GmbH (Germany). Inst. fuer Plasmaphysik, EURATOM Association, Trilateral Euregio Cluster, Dec. 2003.
- [KBS12] Patrick Kilian, Thomas Burkart, and Felix Spanier. “The Influence of the Mass Ratio on Particle Acceleration by the Filamentation Instability”. In: *High Performance Computing in Science and Engineering '11*. Ed. by Wolfgang E. Nagel, Dietmar B. Kröner, and Michael M. Resch. Berlin Heidelberg: Springer, 2012, pp. 5–13.
- [KK05] KATRIN Collaboration and KATRIN Collaboration. *KATRIN design report 2004*. Tech. rep. 51.54.01; LK 01. Forschungszentrum, Karlsruhe, 2005. 245 pp.
- [Kod+01] K. Kodama et al. “Observation of tau neutrino interactions”. In: *Physics Letters B* 504.3 (2001), pp. 218–224.
- [Kol08] Michael Kolonko. *Stochastische Simulation : Grundlagen, Algorithmen und Anwendungen*. SpringerLink. Wiesbaden: Vieweg+Teubner, 2008.
- [KR94] Yong-Ki Kim and M. E. Rudd. “Binary-encounter-dipole model for electron-impact ionization”. In: *Physical Review A* 50.5 (1994), pp. 3954–3967.
- [Kra+05] Ch. Kraus et al. “Final results from phase II of the Mainz neutrino mass search in tritium beta decay”. In: *Eur. Phys. J. C* 40 (2005), pp. 447–468.
- [Kuc+18] Laura Kuckert et al. “Modelling of gas dynamical properties of the Katrin tritium source and implications for the neutrino mass measurement”. In: *Vacuum* 158 (2018), pp. 195–205.
- [Kuc16] L. Kuckert. “The windowless gaseous tritium source of the KATRIN experiment - Characterisation of gas dynamical and plasma properties”. PhD thesis. Fakultät für Physik des Karlsruher Instituts für Technologie, Oct. 2016.
- [Lan12] Sebastian Lange. “Turbulenz und Teilchentransport in der Heliosphäre - Simulationen von inkompressiblen MHD-Plasmen und Testteilchen -”. doctoral thesis. Universität Würzburg, 2012.

- [Leh51] Derrick H. Lehmer. “Mathematical Methods in Large-scale Computing Units”. In: *Proceedings of the Second Symposium on Large Scale Digital Computing Machinery*. Cambridge, United Kingdom: Harvard University Press, 1951, pp. 141–146.
- [LL11] Lev Davidovič Landau and Evgenij M. Lifšic. *Lehrbuch der theoretischen Physik*. Unveränd. Nachdr. der 14., korr. Aufl. 1997. Vol. 1: Mechanik. Frankfurt am Main: Deutsch, 2011. ISBN: 9783817113262.
- [MG88] C. A. Miderski and Gregory I. Gellene. “Experimental evidence for the formation of $H < H^* H + 5/e^-$ dissociative recombination”. In: *The Journal of Chemical Physics* 88.9 (May 1988), pp. 5331–5337.
- [MNS62] Ziro Maki, Masami Nakagawa, and Shoichi Sakata. “Remarks on the Unified Model of Elementary Particles”. In: *Progress of Theoretical Physics* 28.5 (Nov. 1962), pp. 870–880.
- [MS95] A A Matveyev and V P Silakov. “Kinetic processes in a highly-ionized non-equilibrium hydrogen plasma”. In: *Plasma Sources Science and Technology* 4.4 (Nov. 1995), pp. 606–617.
- [Nas+05] Anatoly F. Nastoyashchii et al. “Effects of Plasma Phenomena on Neutrino Mass Measurements Process Using a Gaseous Tritium β -Source”. In: *Fusion Science and Technology* 48.1 (2005), pp. 743–746.
- [Nie16] Frank Nielsen. *Introduction to HPC with MPI for Data Science*. Cham, 2016.
- [Nor61] Theodore G Northrop. “The guiding center approximation to charged particle motion”. In: *Annals of Physics* 15.1 (1961), pp. 79–101.
- [Pau30] Wolfgang Pauli. *Offener Brief an die Gruppe der Radioaktiven der Gauvereins-Tagung zu Tübingen*. 1930.
- [Pet+15] J.B.C. Pettersson et al. “Dissociative recombination and excitation of $D5+$ by collisions with low-energy electrons”. In: *Molecular Physics* 113.15-16 (2015), pp. 2099–2104.
- [Pla+12] Radek Plasil et al. “Stabilization of $H^+ - H_2$ collision complexes between 11 and 28K”. In: *Philosophical transactions. Series A, Mathematical, physical, and engineering sciences* 370 (Nov. 2012), pp. 5066–73.
- [Pon58] B. Pontecorvo. “Inverse beta processes and nonconservation of lepton charge”. In: *Sov. Phys. JETP* 7 (1958). [*Zh. Eksp. Teor. Fiz.*34,247(1957)], pp. 172–173.
- [Pre+92] William H. Press et al. *Numerical Recipes in C (2Nd Ed.): The Art of Scientific Computing*. New York, NY, USA: Cambridge University Press, 1992. ISBN: 0-521-43108-5.
- [Qin+13] Hong Qin et al. “Why is Boris algorithm so good?” In: *Physics of Plasmas* 20.8 (2013), p. 084503.
- [Rei+60] F. Reines et al. “Detection of the Free Antineutrino”. In: *Phys. Rev.* 117 (1 Jan. 1960), pp. 159–173.

-
- [Röl15] Marco Röllig. “Tritium analytics by beta induced X-ray spectrometry”. 51.03.01; LK 01. PhD thesis. 2015. 202 pp.
- [Sch16] Kerstin Schönung. “Development of a Rear Wall for the KATRIN Rear Section and investigation of tritium compatibility of Rear Section components”. PhD thesis. Karlsruher Institut für Technologie (KIT), 2016. 336 pp.
- [Sei19] Hendrik Seitz-Moskaliuk. “Characterisation of the KATRIN tritium source and evaluation of systematic effects”. 51.03.01; LK 01. PhD thesis. Karlsruher Institut für Technologie (KIT), 2019. 204 pp.
- [SJ97] M.P. Skrzypkowski and R. Johnsen. “Electron-temperature dependence of the recombination of $\text{NH}_4^+(\text{NH}_3)_n$ ions with electrons”. In: *Chemical Physics Letters* 274.5 (1997), pp. 473–477.
- [SJP05] Francesc Salvat, Aleksander Jablonski, and Cedric J. Powell. “elsepa—Dirac partial-wave calculation of elastic scattering of electrons and positrons by atoms, positive ions and molecules”. In: *Computer Physics Communications* 165.2 (2005), pp. 157–190.
- [Tan+18] M. Tanabashi et al. “Review of Particle Physics”. In: *Phys. Rev. D* 98 (3 Aug. 2018), p. 030001.
- [The19] The HDF Group. *Hierarchical Data Format, version 5*. 1997-2019. URL: <http://www.hdfgroup.org>.
- [TS00] Tatsuo Tabata and Toshizo Shirai. “Analytic cross sections for collisions of H^+ , H_2^+ , H_3^+ , H , H_2 , and H^- with hydrogen molecules”. In: *Atomic Data and Nuclear Data Tables* 76 (Sept. 2000), pp. 1–25.
- [Val07] Kathrin Valerius. *Systematics and background suppression in the KATRIN experiment*. 2007.
- [Val10] K. Valerius. “The wire electrode system for the KATRIN main spectrometer”. In: *Progress in Particle and Nuclear Physics* 64.2 (2010). Neutrinos in Cosmology, in Astro, Particle and Nuclear Physics, pp. 291–293.
- [Vel00] Todd L. Veldhuizen. “Blitz++: The Library that Thinks it is a Compiler”. In: *Advances in Software Tools for Scientific Computing*. Ed. by Hans Petter Langtangen, Are Magnus Bruaset, and Ewald Quak. Berlin, Heidelberg: Springer Berlin Heidelberg, 2000, pp. 57–87. ISBN: 978-3-642-57172-5.
- [Win11] A. Windberger. “Berechnungen und Simulationen zum Verhalten von Ionen in der differentiellen Pumpstrecke des KATRIN-Experiments”. MA thesis. Fakultät für Physik des Karlsruher Instituts für Technologie, 2011.
- [Yoo+08] Jung-Sik Yoon et al. “Cross Sections for Electron Collisions with Hydrogen Molecules”. In: *Journal of Physical and Chemical Reference Data* 37.2 (June 2008), pp. 913–931.
- [ZU18] Seiji Zenitani and Takayuki Umeda. “On the Boris solver in particle-in-cell simulation”. In: *Physics of Plasmas* 25.11 (2018), p. 112110.

A. Appendix



Figure A.1.: The FERMIAC, invented by E. Fermi. The FERMIAC is an analog computer using Monte Carlo method to study slow neutrino transport. It is one of the first applications of Monte Carlo methods for modern physics. (Picture from [Com17])

```
1 # Parameter template for mcelectro
2 # Christian Reiling Version 18.11.19
3 #
4 # File ignores Lines starting with '#' or empty
5 # '=' ';' ',' and whitespaces are delimiters
6 # First value is Parameter Name
7 # Second value is Parameter Value
8 # Further Symbols are ignored
9
10
11 ### Simulation Parameters
12 SEED =          2342395328  Seed for PRNG
13 POP_DECAYS =   1e4          Number of decays for initial density calculation
14 POP_STEP =     2            Step width for initial density calculation
15 DECAYS =       1e5          Target number of beta decays
16 STEP =         200          Step width of beta decays before density synchronisation
17 LOG_BARS =     14           Number of logging barriers for Logging
18 PROPAGATION =  0            0 = Drift approximation, 1 = Boris Push
19 BORIS_T =      1e-10        Resolution for BorisPush
20 E_FIELD =      1            0 = off, 1 = load data
21
22 ### Katrin
23 # Properties
24 BFIELD =        2.5          B_z in T
25 T2_MAXDENS =    1e21         Peak Density at z=5m in m^-3
26 TEMP =          30           Temperatur of WGTS in K
```

A. Appendix

```
27 T2_VELO =      -1          -1 = data from Kuckert, else = v_z in m/s speed
28
29 ### Injection
30 INJECTION =     0          0 = Fermi, 1 = Delta, 2 = MB
31 INJ_E =        0          Injection energy in eV. Ignored for Fermi, for MB using E=kb*T
32 INJ_TI =       1          0 = No Ion, 1 = thermal Ion Injection
33
34 ### Termination
35 TERM_E =       1e-7       Threshold energy for termination
36 TERM_DI_E =   1e-4       Threshold energy for termination of electrons at z = 10
37 TERM_MAX =    1e4        Maximum Inteaction before termination
38
39 ### Interactions: 0 = Omitted, >1 = Activated
40 eT2_ELA =      1
41 INT_ELA_DIR =  0          0 = elastic data, 1=4pi, 2=0pi
42
43 eT2_ION =      1          1 = Janev (3channels), 2 = BED-Theory
44 eT2_ROT =      2          0 = off, 1 = not implemented, 2 = Y00N
45 eT2_VIB =      1          0 = off, 1 = Janev, 2 = Y00N
46 eT2_EL =       1          0 = off, 1 = Janev, 2 = Y00N
47 e_REC =        1
48
49 INT_N =        100       Number of points for theta integration
50 INT_PRE_START = 1e-7     Start energy for precomputed cross sections
51 INT_PRE_END =  1e0      End energy for precomputed cross sections
52 INT_PRE_N =    1e3      Number of points for precomputed cross sections
53
54 ### Properties of runtime density containers
55 POP_N_R =      5          Number of bins in r
56 POP_N_PHI =    1          Number of bins in phi
57 POP_N_Z =     13          Number of bins in z
58 POP_N_E =     50          Number of bins in E for kinetic bins
59 POP_E_START =  1e-7      Minimum energy bin for kinetic bins
60 POP_E_END =    2e4       Maximum energy bin for kinetic bins
```

Listing A.1: Sample parameter file for the KARL code. Parameters are set using recommended values. For details see section 5.9.

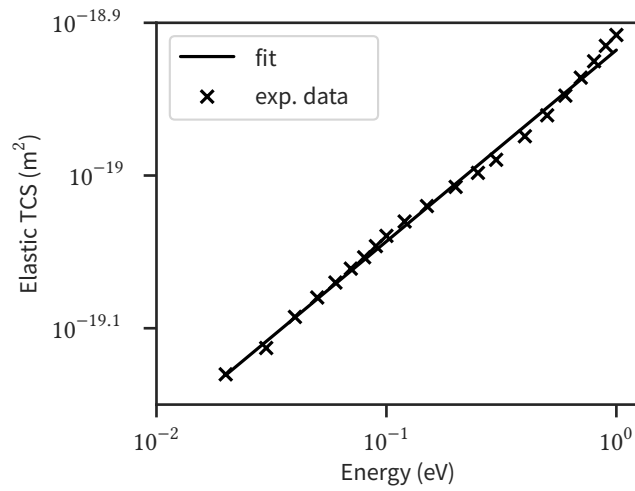


Figure A.2.: Linear fit of e^- - T_2 elastic scattering TCS data below 1 eV from [Yoo+08] . Resulting fit is used for sub 0.02 eV regime. Energies in laboratory frame, where of kinetic electrons interact with fixed T_2 molecules.

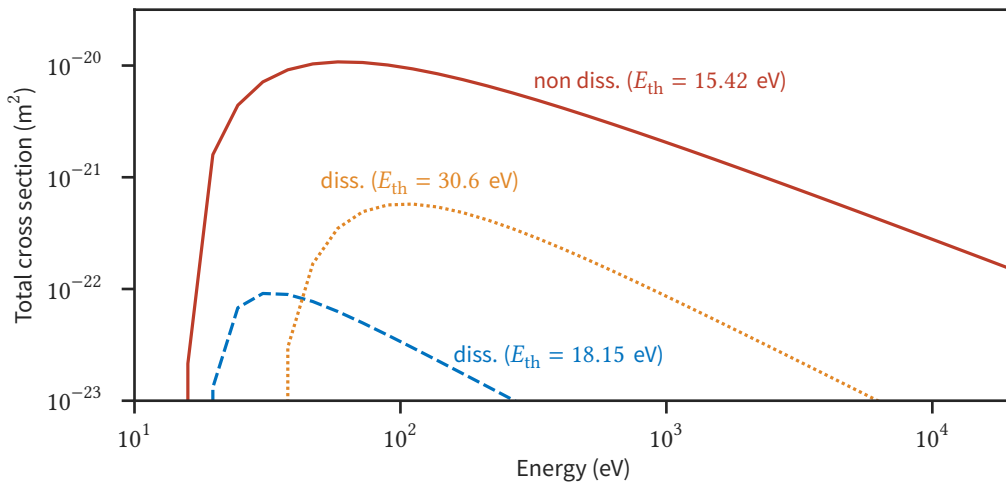


Figure A.3.: TCS for electron impact ionization of T_2 . Cross sections from [JRS03]. Non-dissociative ionization channel with threshold energy of 15.42 eV displayed as solid red line. Dissociative ionization channel with threshold energy of 18.15 eV displayed as dashed blue line. Dissociative ionization channel with threshold energy of 30.6 eV displayed as dotted yellow line. Energies in laboratory frame, where of kinetic electrons interact with fixed T_2 molecules.

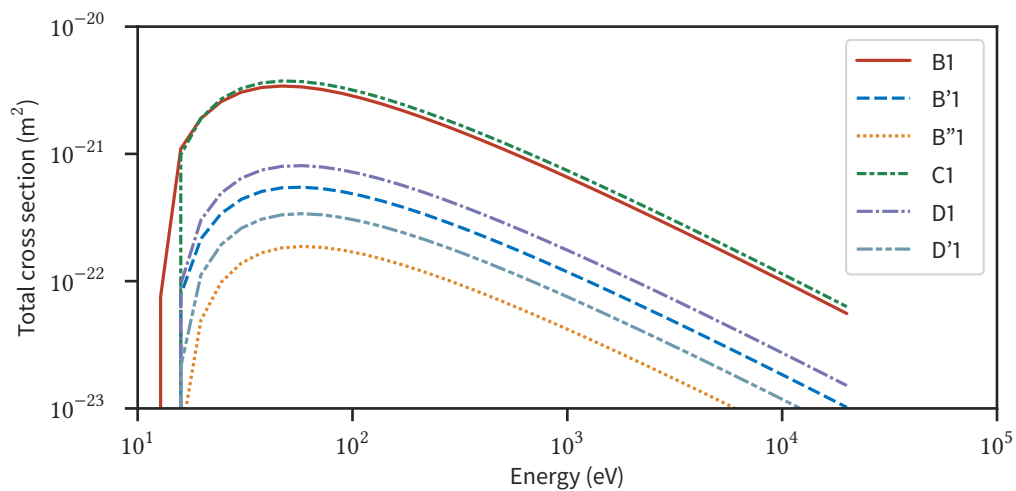


Figure A.4.: TCSs of e^- electronic excitations of T_2 to dipole allowed singlet states. Models from [JRS03]. Energies in laboratory frame, where of kinetic electrons interact with fixed T_2 molecules.

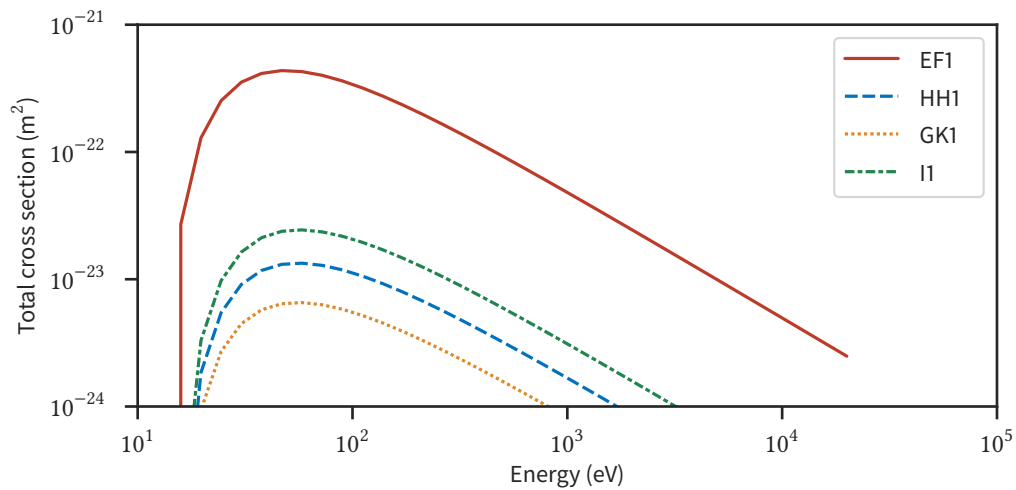


Figure A.5.: TCSs of e^- electronic excitations of T_2 to symmetry forbidden singlet states. Models from [JRS03]. Energies in laboratory frame, where of kinetic electrons interact with fixed T_2 molecules.

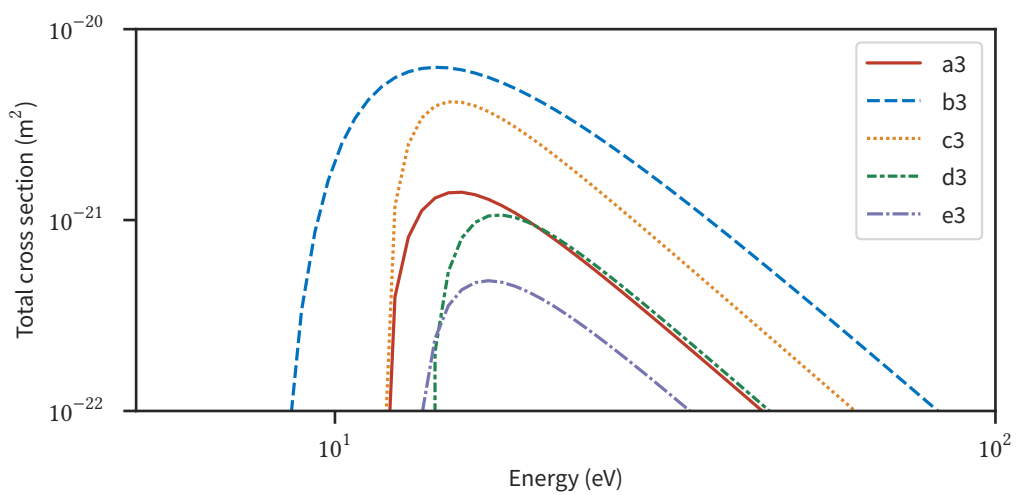


Figure A.6.: TCSs of e^- electronic excitations of T_2 to tripled states. Models from [JRS03]. Energies in laboratory frame, where of kinetic electrons interact with fixed T_2 molecules.

A. Appendix

```
1 # Parameter file for SIM1
2 ### Simulation Parameters
3 SEED =          2342395328  Seed for PRNG
4 POP_DECAYS =    5e3          Number of decays for initial density calculation
5 POP_STEP =      2           Step width for initial density calculation
6 DECAYS =        1e4         Target number of beta decays
7 STEP =          10          Step width of beta decays before density synchronisation
8 LOG_BARS =      14          Number of logging barriers for Logging
9 PROPAGATION =   0           0 = Drift approximation, 1 = Boris Push
10 BORIS_T =       1e-10       Resolution for BorisPush
11 E_FIELD =       0           0 = off, 1 = load data
12
13 ### Katrin
14 # Properties
15 BFIELD =        2.5          B_z in T
16 T2_MAXDENS =    1e21         Peak Density at z=5m in m^-3
17 TEMP =          30           Temperatur of WGTS in K
18 T2_VELO =       -1          -1 = data from Kuckert, else = v_z in m/s speed
19
20 # Injection
21 INJECTION =     0           0 = Fermi, 1 = Delta, 2 = MB
22 INJ_E =         0           Injection energy in eV. Ignored for Fermi, for MB using E=kb*T
23 INJ_TI =        1           0 = No Ion, 1 = thermal Ion Injection
24
25 # Termination
26 TERM_E =        1e-7         Threshold energy for termination
27 TERM_DI_E =     0           Threshold energy for termination of electrons at z = 10
28 TERM_MAX =      1e8          Maximum Inteaction before termination
29
30 # Interactions
31 eT2_ELA =       1           0 = Omitted, >1 = Activated
32 INT_ELA_DIR =   0           0 = elastic data, 1=4pi, 2=0pi
33
34 eT2_ION =        1           1 = Janev (3channels), 2 = BED-Theory
35 eT2_ROT =        2           0 = off, 1 = not implemented, 2 = Y00N
36 eT2_VIB =        1           0 = off, 1 = Janev, 2 = Y00N
37 eT2_EL =         1           0 = off, 1 = Janev, 2 = Y00N
38 e_REC =         0
39
40 INT_N =          100         Number of points for theta integration
41 INT_PRE_START = 1e-7         Start energy for precomputed cross sections
42 INT_PRE_END =   1e-0         End energy for precomputed cross sections
43 INT_PRE_N =      9e3         Number of points for precomputed cross sections
44
45 # Properties of runtime density containers
46 POP_N_R =        5           Number of bins in r
47 POP_N_PHI =      1           Number of bins in phi
48 POP_N_Z =        13          Number of bins in z
49 POP_N_E =        50          Number of bins in E for kinetic bins
50 POP_E_START =    1e-7         Minimum energy bin for kinetic bins
51 POP_E_END =      2e4         Maximum energy bin for kinetic bins
```

Listing A.2: Simulation parameter file for SIM1.

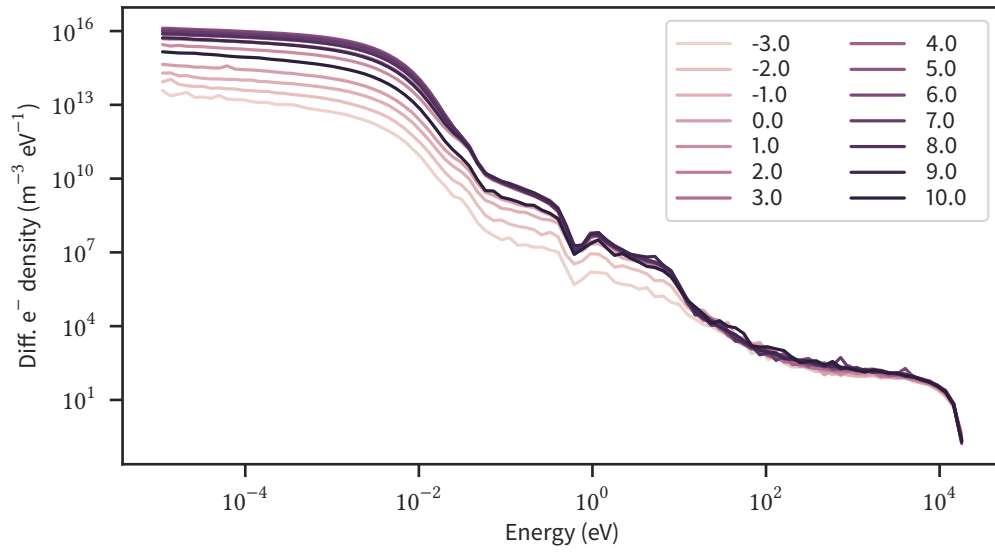


Figure A.7.: Differential electron densities from SIM1 at different longitudinal positions z throughout the WGTS. Each line represents a different z position.

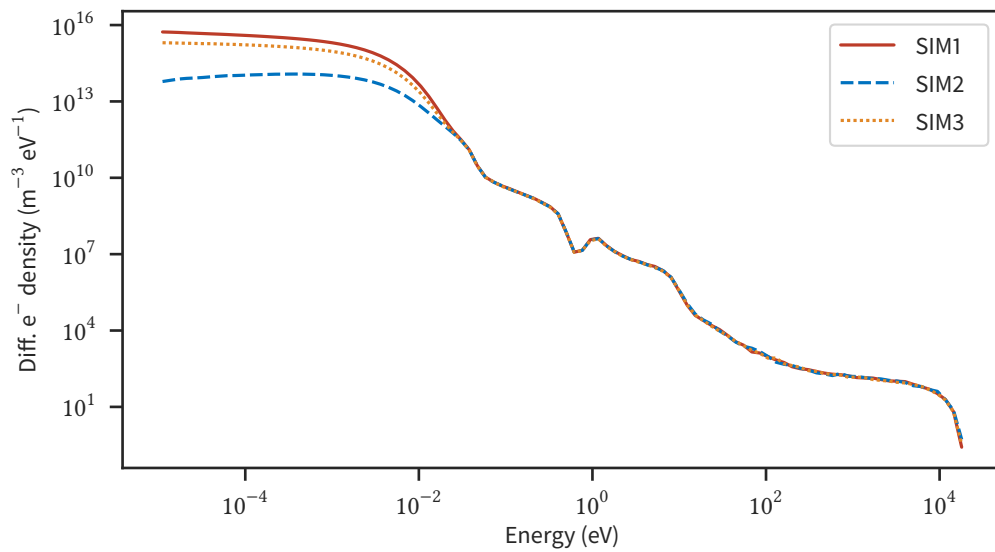


Figure A.8.: Comparison of differential electron densities of SIM1, SIM2, SIM3. Results averaged over the length of the WGTS. The shaded area represent the standard deviation. SIM1: Conservative estimator without recombination, displayed as solid, red line. SIM2: Implementation of asymmetric recombination, displayed as dashed, blue line. SIM3: Implementation of recombination by solely accounting electron energy in the MCS calculation, displayed as dotted, yellow line.

Danksagung

Zum Abschluss dieser Arbeit möchte ich mich herzlich bei allen Unterstützern auf meinem Weg hierher bedanken. Mein besonderer Dank gilt

- Prof. Dr. Guido Drexlin, für die Möglichkeit meine Masterarbeit im Umfeld von KATRIN schreiben zu dürfen, für die Einführung in die Astroteilchenphysik, sowie für jeglicher Unterstützung auf dem Weg hierher.
- Prof. Dr. Günter Quast, für die Unterstützung als Korreferent dieser Arbeit.
- Dr. Felix Spanier, für die ausgeprägt fachliche Betreuung, der thematische Einführung in die Welt der numerischen Simulationen und der Plasmaphysik, als auch für die Korrektur meiner Arbeit.
- Jonas Kellerer, als Betreuer vor Ort, für jegliche Unterstützung und spannenden Diskussionen, sowie für die aufmerksame Korrektur meiner Arbeit.
- Der gesamten KATRIN Kollaboration, für das Zusammenarbeit am KATRIN Experiment und der damit eingehenden Möglichkeit an solch einem spannenden Projekt zu arbeiten.
- Der Karlsruher KATRIN Arbeitsgruppe, für die tolle Arbeitsatmosphäre, die das vergangene Jahr auf fachlicher und persönlicher Ebene sehr bereichert hat und stets für Freude gesorgt hat.
- Meiner Familie, Kerstin und meinen Freunden, für die Unterstützung.